

Carbon-Supported Silver Catalysts for Electrocatalytic Reduction of CO₂ to CO

Koolstof-gedragen zilver katalysatoren voor elektrokatalytische reductie van CO₂ tot
CO
(met een samenvatting in het Nederlands)

Proefschrift

ter verkrijging van de graad van doctor aan de
Universiteit Utrecht
op gezag van de
rector magnificus, prof. dr. H.R.B.M. Kummeling,
ingevolge het besluit van het college voor promoties
in het openbaar te verdedigen op

woensdag 31 januari 2024 des ochtends te 10.15 uur

door

Francesco Mattarozzi

geboren op 7 september 1994
te Como, Italië

Promotor:

Prof. dr. P.E. de Jong

Copromotor:

Dr. P. Ngene

Beoordelingscommissie:

Prof. dr. F.M.F de Groot

Prof. dr. W.K. Kegel

Prof. dr. G. Mul

Dr. W. van der Stam

Prof. dr. D.A.M Vanmaekelbergh

Dit proefschrift, in samenwerking Shell Global Solutions International B.V., maakt deel uit van het Advanced Research Center Chemical Building Blocks Consortium (ARC-CBBC), mede-opgericht en medegefinancierd door het NWO en het ministerie van Economische Zaken en Klimaat.

Contents

<u>CHAPTER 1</u>	Introduction.....	1
	1.1 CO ₂ emissions	2
	1.2 Electrochemistry and electrolyzers	4
	1.3 Heterogeneous electrocatalysis	7
	1.4 CO ₂ electrocatalytic reduction	10
	1.5 CO ₂ reduction to CO on silver and carbon	14
	1.6 Scope of this thesis	17
 <u>CHAPTER 2</u>	 Surface-modified carbon materials.....	 24
	Abstract.....	25
	2.1 Introduction.....	26
	2.2 Experimental section	28
	2.2.1 Modification of carbon materials	28
	2.2.2 Working electrode preparation	28
	2.2.3 Carbon characterization	29
	2.2.4 Electrochemical measurements	30
	2.3 Results and discussion	33
	2.3.1 Tuning the surface properties of graphitic carbon.....	33
	2.3.2 Electrocatalytic reduction of CO ₂	39
	2.3.3 Effect of the surface functional groups on the CO selectivity	42
	2.4 Conclusions.....	44
 <u>CHAPTER 3</u>	 Ligand-free silver nanoparticles.....	 49
	Abstract.....	50
	3.1 Introduction.....	51
	3.2 Experimental section	52
	3.2.1 Modification of the carbon materials.....	52

3.2.2	Synthesis of supported silver nanoparticles.....	52
3.2.3	Working electrode preparation	53
3.2.4	Characterization.....	53
3.2.5	Electrochemical measurements	56
3.3	Results and discussion	60
3.3.1	Control over the particle size.....	60
3.3.2	Electrocatalytic activity.....	64
3.3.3	Effect of the silver coverage on the CO Faradaic efficiency	66
3.3.4	Effect of the particle size on the CO partial current density	67
3.3.5	H ₂ to CO ratio	70
3.4	Conclusions.....	71

CHAPTER 4

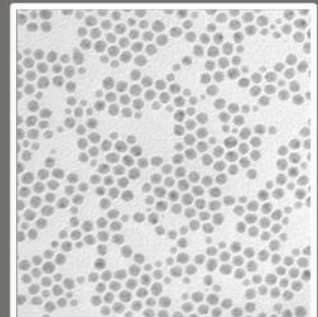
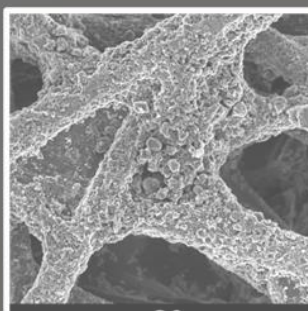
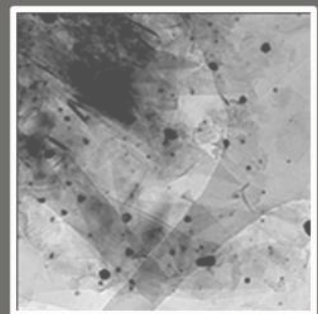
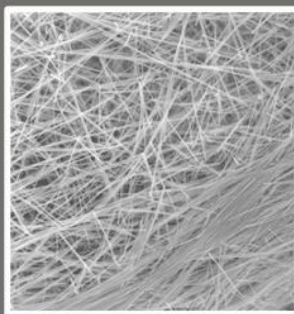
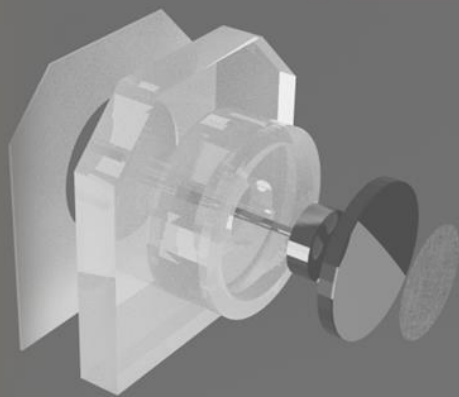
	Alkylamine-functionalized carbon supports for silver nanoparticles	75
	Abstract.....	76
4.1	Introduction.....	77
4.2	Experimental section	79
4.2.1	Synthesis of silver nanoparticles	79
4.2.2	Synthesis of functionalized carbon powders.....	79
4.2.3	Synthesis of functionalized carbon electrodes.....	80
4.2.4	Characterization.....	80
4.2.5	Electrocatalytic measurements	81
4.3	Results and discussion	83
4.3.1	Synthesis of silver nanoparticles	83
4.3.2	Carbon functionalization	84
4.3.3	Carbon supported silver nanoparticles (electrodes).	89
4.3.4	Electrocatalytic performance: influence of hydrophobic functionalization on the catalysts' selectivity.....	91
4.4	Conclusions.....	96

<u>CHAPTER 5</u>	Oxide-derived silver nanowires	100
	Abstract.....	101
	5.1 Introduction.....	102
	5.2 Experimental section	104
	5.2.1 Synthesis of pristine silver nanowires	104
	5.2.2 Synthesis of fresh AgCl.....	104
	5.2.3 Synthesis of oxide-derived silver nanowires	105
	5.2.4 Characterization.....	106
	5.2.5 Electrochemical measurements	107
	5.3 Results and Discussion.....	109
	5.3.1 Synthesis and characterization of oxide-derived silver nanowires	109
	5.3.2 Electrocatalytic activity and selectivity	114
	5.3.3 Understanding the selectivity of oxide-derived silver nanowires	117
	5.3.4 Electrocatalytic stability.....	121
	5.4 Conclusions.....	124
<u>CHAPTER 6</u>	Summary	130
	Outlook	133
	Samenvatting	135
	List of publications	139
	About the author.....	143
	Acknowledgements.....	145



CHAPTER 1

Introduction



1.1 CO₂ emissions

Ever since the industrial revolution, fossil fuels have been the primary energy source, producing several benefits for human society. Nevertheless, their combustion has led to an unprecedented rise in greenhouse gasses emissions, greatly exceeding the amount that the ecosystem can absorb and dramatically affecting the climate^[1]. The CO₂ gas atmospheric concentration grew from 280 ppm in the early 1800s to 420 ppm in 2023. In the latest Intergovernmental Panel on Climate Change report, it was estimated that the greenhouse gas emissions have already caused a global warming of approximately 1.0 °C above the pre-industrial levels (1850-1900)^[2].

Several international attempts to mitigate the climate problem, caused by CO₂ emissions, were made in the past years, starting from the Kyoto protocol in 1997^[3] until the Paris agreement in 2015^[4]. As we entered the 'decade of actions (2020-2030)'^{[5][6]}, we must commit to a sustainable energy transition, encouraging the idea of reducing consumption, supporting the principle of circularity, and changing our primary energy sources. The use of renewable resources is key to accomplishing this energy transition, but their intermittent nature remains a challenge^{[7][8][9]}. Large scale devices to store renewable electricity are needed to overcome this problem. However, the scarcity of raw materials to produce large scale technologies, the lack of cost-effective recycling processes and infrastructures, delayed this process.

The implementation of carbon capture and utilization technologies aims to achieve a zero net emission society, by removing CO₂ from the atmosphere and converting it into valuable chemicals. This would enable the use of CO₂ as carbon feedstock^{[10][11][12]}. The first challenge is to selectively capture CO₂. Both direct air capture and point source capture are interesting strategies to tackle the problem. While the former enables the capture of diluted CO₂ (420 ppm) from the atmosphere, effectively lowering the atmospheric concentration of the greenhouse gas, the latter allows to capture of highly concentrated CO₂ from exhaust gasses in power plants or refineries before it is released in the atmosphere, decreasing CO₂ emissions^{[13][14][15]}.

Electrochemistry is an exciting strategy to utilize CO₂. Specifically, the electrocatalytic conversion of CO₂ might offer a solution to both the renewable energy storage problem and

CO₂ utilization, by storing renewable electricity in chemical bonds, and thereby creating a human-driven CO₂ cycle (figure 1.1)^{[16][17]}. Research and development of efficient electrocatalyst materials, combined with a fundamental understanding of the electrochemical reactions, are pivotal aspects of this revolution, as well as key motivations behind this thesis.

In the next sections, we present a general overview of the principles of electrochemistry and electrocatalysis, which provides the basis for a detailed discussion on the electrocatalytic conversion of CO₂.

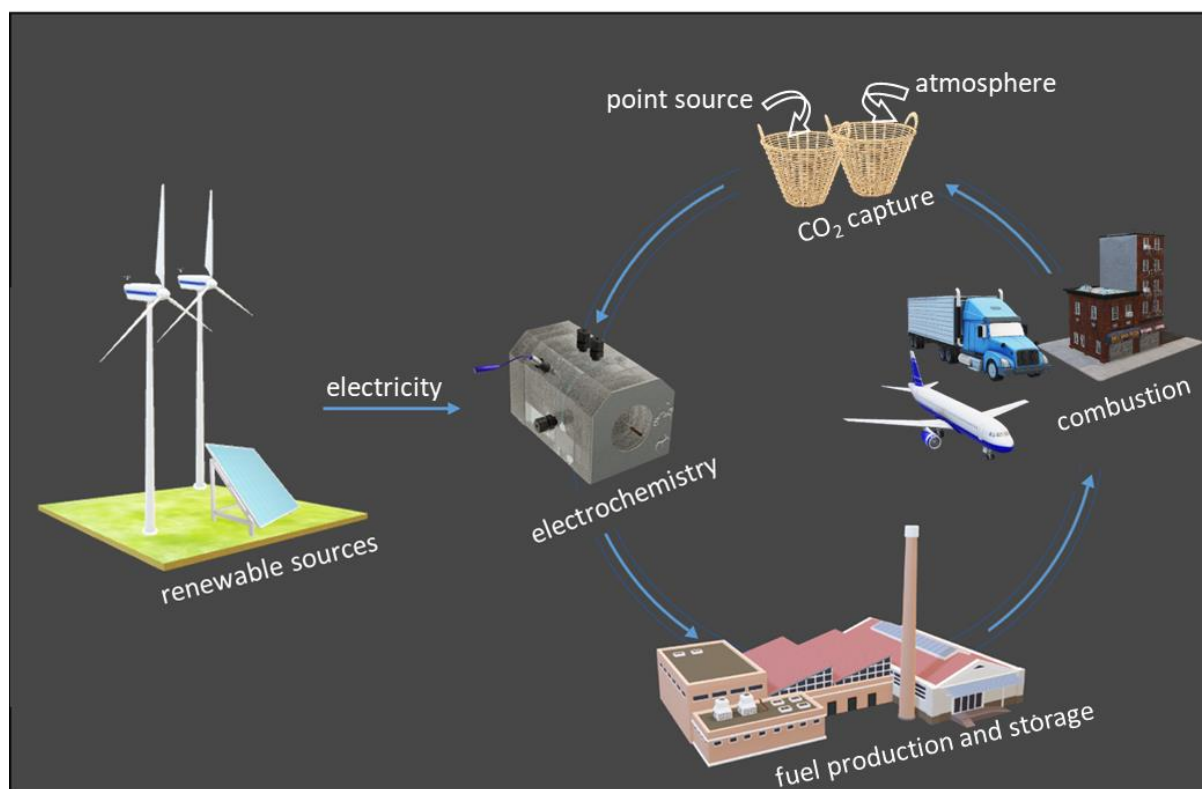


Figure 1.1 – CO₂ reduction driven by renewable electricity, aiming to convert greenhouse to chemicals and fuels.

1.2 Electrochemistry and electrolyzers

Electrochemistry is defined as the branch of physical chemistry which studies chemical reactions involving the transfer of one or multiple electrons, driven by a difference in electrical potential^[18]. Electrochemistry is at the basis of life, as it controls many biochemical processes in humans. For instance, the continuous exchange of electrons between the redox cofactors NAD⁺ and NADH play a key role in glucose metabolism^[19]. In the late 18th century, Alessandro Volta discovered that electrical current could be generated by simply stacking discs of zinc and copper separated by a cloth soaked in brine (NaCl aqueous solution) and connecting the top and bottom discs with a metallic wire^[20]. This was the first example of galvanic cell (battery), where electricity was produced by the spontaneous oxidation of zinc ($\text{Zn} \rightarrow \text{Zn}^{2+} + 2\text{e}^-$) and the reduction of protons ($2\text{H}^+ + 2\text{e}^- \rightarrow \text{H}_2$). The importance of electrochemistry in the contemporary society was demonstrated by the 2019 Nobel Prize in chemistry, awarded to J. B. Goodenough, M. S. Whittingham, and A. Yoshino for their work on development of lithium-ion batteries in the 70s^[21].

An electrolyzer uses electrical energy to power non-spontaneous chemical reactions, for instance converting molecules, such as H₂O, into energy carriers, such as H₂. At the cathode, a reduction reaction takes place, involving an electroactive species accepting electrons, while at the anode oxidation reaction occurs, with a species losing electrons^[22]. The net result of the reaction is a change in the oxidation state of the reactants. The electrons are transported from anode to cathode *via* an external circuit, normally a wire connecting the two electrodes. Between the two electrodes, an electrolyte ensures the movement of ions, governed by migration. Positively charged ions are transported towards the negatively charged cathode, while the negatively charged ions migrate towards the anode. The two half reactions are separated by an ion-selective membrane or a salt bridge, which allows only the flow of specific ions, keeping physically separated the electroactive species. This prevents spontaneous homogeneous redox (reduction-oxidation) reactions from taking place. A potentiostat provides the potential difference between the two electrodes, which is the driving force of the reaction^{[12][23][24]}.

At standard conditions (i.e. 298 K, 1 bar and 1 M concentration), the minimum energy input (E_{cell}^0) required to perform the electrochemical reaction is determined by the difference in standard reduction potential of the two half reactions (equation 1.1):

$$E_{cell}^0 = E_{cathode}^0 - E_{anode}^0 \quad \text{equation 1.1}$$

The E_{cell}^0 is related to the standard Gibbs free energy of the reaction (ΔG^0) by the equation 1.2:

$$\Delta G^0 = -n * F * E_{cell}^0 \quad \text{equation 1.2}$$

Where n is the number of electrons transferred during the electrochemical reaction and F is the Faraday constant, which defines the charge transferred per mole of electrons (96485 C mol^{e-}⁻¹). Therefore, a positive E_{cell}^0 and negative ΔG^0 characterize spontaneous reactions. Deviating from the standard conditions, the theoretical value of cell potential is given by the Nernst equation, linking the electrode potential with the bulk concentration of the reactants and products (equation 1.3):

$$E_{cell} = E_{cell}^0 - \frac{(R * T)}{n * F} * \ln Q \quad \text{equation 1.3}$$

Where R is the ideal gas constant (8.31 J K⁻¹ mol⁻¹), T is the temperature (K), n are the moles of electrons per mole of reactant (mol^{e-} mol⁻¹), F is the Faraday constant and Q is the reaction quotient, ratio between the activities of products and reactants, each raised to the power of the number of moles of the reactants or products^[25]. In addition to this minimum voltage requirement, an overpotential is necessary to run the electrochemical reactions to an appreciable rate. This is required to overcome both the high energy barriers of individual elemental steps of the electrochemical reaction (activation energy or overpotential) and the electrolyte resistance or other resistances in the system (ohmic resistance). This overpotential (η) is defined as the difference between the equilibrium cell potential, calculated using the Nernst equation, and the applied voltage (equation 1.4):

$$\eta = E_{applied} - E_{cell} \quad \text{equation 1.4}$$

The rate of the electrochemical process, which can be expressed as current density flowing through the electrode, depends on the driving force of the process, the applied potential. By increasing the cathodic potential bias, an increase in cathodic current is expected. The Butler-Volmer equation (equation 1.5)^{[26][27]}, describes the electrochemical kinetics of a reaction both in the oxidation and reduction direction at the electrode surface, as a function of the overpotential (η):

$$j = j_0 * \left\{ \exp\left[\frac{(1-\alpha) * n * F * \eta}{R * T}\right] - \exp\left[\frac{-\alpha * n * F * \eta}{R * T}\right] \right\} \quad \text{equation 1.5}$$

Where j is the electrode current density (A m^{-2}), j_0 is the exchange current density, a measure of the intrinsic rate of the reaction on a specific electrode material in the absence of overpotential (A m^{-2}), α is a dimensionless factor called charge transfer coefficient. This equation does not account for mass transport limitations, and hence is mostly valid at low current densities. When a large negative overpotentials is applied, the first exponential in the Butler-Volmer equation becomes negligible compared to the second. This leads to a simplified version of this equation (equation 1.6):

$$\log |j| = \log j_0 - \frac{\alpha * F}{2.3 R * T} * \eta \quad \text{equation 1.6}$$

This equation is called the Tafel equation^{[18][28][29]}, and its validity is limited to high overpotentials, and not-mass transport limited systems. In a plot $\log j$ vs η , the Tafel slope can reveal information about the rate determining step of the electrochemical reaction. This concept will be applied in chapter 5 to evaluate the rate determining step for CO_2 electroreduction on silver nanowire electrodes. Another parameter of interest in electrochemistry is the faradaic efficiency. The faradaic efficiency represents the reaction selectivity towards a specific product, which is evaluated as the ratio between the current used to generate the specific product and the total current flowing through the system.

In the next section, we will discuss in detail heterogeneous electrocatalysts, focusing on the electrolyte region close to the electrode surface, which has great influence on the selectivity of the chemical reaction.

1.3 Heterogeneous electrocatalysis

Electrocatalysis is a field of electrochemistry in which a catalyst promotes electrochemical reactions by lowering the activation energy of the reaction and, hence, increases the reaction rate. The catalyst facilitates electron transfer between electrode and reactive species without being consumed during the reaction. In heterogeneous electrocatalysis, the electrode surface is the catalyst or supports nanostructured catalysts. Therefore, the electrode surface is directly involved in the molecular rearrangement and reaction intermediates stabilization that facilitates the electron transfer across the solid-liquid interface^[30]. Most of the electrocatalyzed industrial electrochemical processes rely on heterogeneous catalysts, thanks to the high stability of the catalyst, easy separation of the products and the possibility to tune the process selectivity by selecting a combination of suitable electrode materials and applied voltage. The chlor-alkali process is an example of an industrial electrocatalytic process, which produces chlorine and concentrated sodium hydroxide on a large scale since the 19th century. A low-carbon steel cathode boosts the kinetics of H₂ evolution in alkaline media, while at the anode an Ir or Ru oxides electrode, doped with TiO₂ or SnO₂, favors the Cl₂ evolution over the O₂ evolution, thus changing the selectivity of the process^[31].

As the reactions occur at interface between the solid electrode and the liquid electrolyte, a model describing the structure and composition of the interface is necessary. The Gouy-Chapman-Stern theory (figure 1.2) describes the electrical double layer formed when a charged electrode is immersed in an electrolyte, including both specific and electrostatic interactions and the thermal motion of ions^{[27][28][18]}. This region is divided into three layers: the Inner Helmholtz Plane (IHP), the Outer Helmholtz Plane (OHP) and the diffused layer. The IHP is a 2-D rigid plane close to the electrode surface ($x \approx 0.1\text{-}0.4$ nm, depending on the ion radius), where only specific, charge independent chemical interactions between ions and the electrode surface occur. This strong interaction results in ions partially losing their solvation shell. After the IHP, fully solvated ions with opposite charge to the electrode gather at the OHP, due to electrostatic interactions with the electrode surface. At OHP ($x < 1$ nm, depending both on the ion radius and solvation shell thickness) the ions are solvated. The IHP and OHP together form the so-called Stern layer^[34]. The potential at the IHP

and OHP changes linearly with the distance from the electrode surface, as described by equation 1.7:

$$\varphi(x) = \frac{q_m}{\varepsilon * \varepsilon_0} * x \quad \text{equation 1.7}$$

Where φ (V) is the potential as a function of the distance (x ; m) from the electrode surface, q_m is the surface charge density at the plane (C m^{-2}), ε is the dielectric constant of the electrolyte solution (dimensionless) and ε_0 is the permittivity constant of vacuum (F m^{-1}). After the OHP, because of thermal motion, the ions distribute in a region where the potential slowly approaches the bulk value, forming a diffused layer, as a result of both the electrostatic interactions and the diffusive forces. The thickness of this layer greatly varies depending on several parameters, such as ionic strength of the electrolyte, surface charge density, electrolyte composition and temperature. In the diffused region, the potential decrease exponentially with the distance from the electrode surface, according to the Poisson-Boltzmann equation (equation 1.8):

$$\varphi(x) = \frac{q_m}{\varepsilon_0 * \varepsilon * k} e^{-(k * x)} \quad \text{equation 1.8}$$

Where k is the inverse of the Debye length (m^{-1}), which includes the temperature effect on the potential.

The structure of the double-layer strongly influences the kinetics of electrocatalyzed reactions, as suggested by Frumkin in the 1930s^{[35][18]}. He argued that the real potential which impacts the reaction kinetic is not the potential at the electrode surface, but the potential at the reaction plane (IHP or OHP). A similar conclusion was drawn for the concentration of electroactive species, which does not correspond to the bulk concentration, but the one at the plane of interest. These considerations are relevant when near surface environment effects are used to explain experimental observations^{[36][37]}.

In the following section, we will explain the theory behind the electrocatalytic reduction of CO_2 .

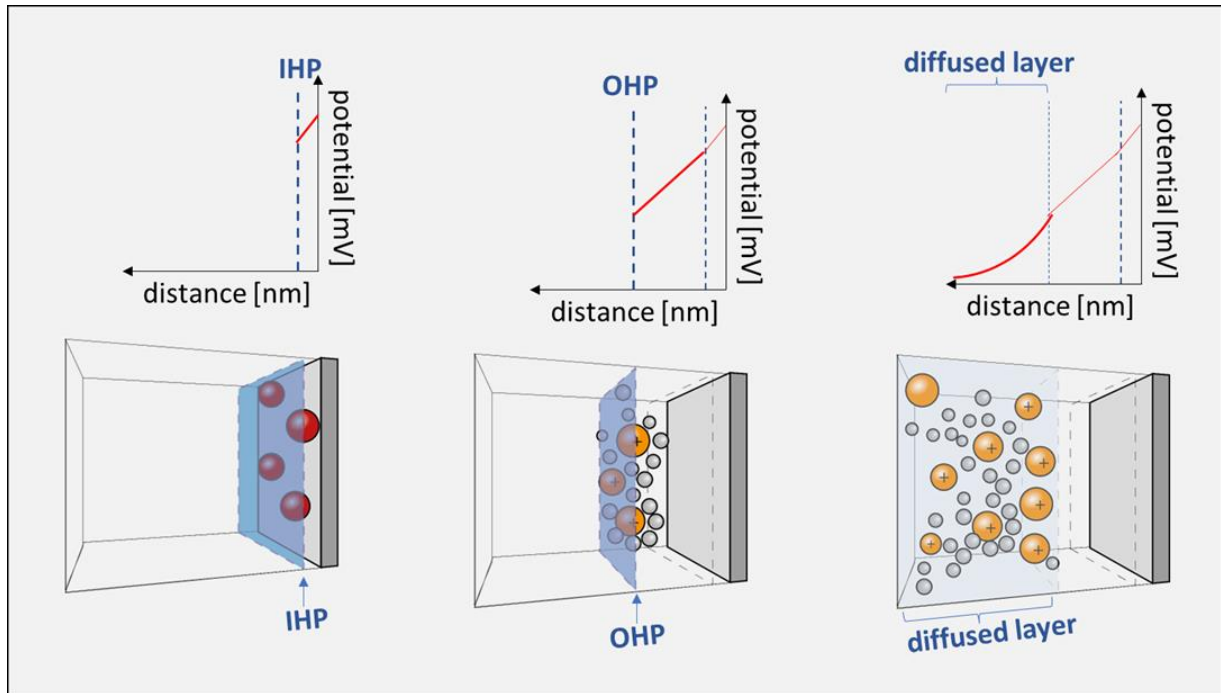


Figure 1.2 – Double layer composition and potential as a function of the distance from the electrode interface. Specifically, the inner Helmholtz plane (IHP), outer Helmholtz plane (OHP) and diffused layer are shown.

1.4 CO₂ electrocatalytic reduction

Pioneered by Hori in the 90s, the interest around the electrocatalytic reduction of CO₂ (CO₂RR – CO₂ reduction reaction) is nowadays revived, thanks to the decreasing cost of renewable electricity, and the urgent need to reduce CO₂ emissions^[17]. Although industrially this reaction is envisioned to be carried out in large gas diffusion electrode flow cells, three electrodes H-type cells are still widely used for fundamental research. The working principle of CO₂RR is simple and the different components of the H-type custom-built cell, used in chapter 2, 4 and 5, are shown in figure 1.3: CO₂ is fed in the cathodic compartment of the electrochemical cell where the cathode (catalyst and carbon paper working electrode) provides electrons and stabilizes the reaction intermediates. At the anode (platinum disc counter electrode), an oxidation reaction, commonly water oxidation to O₂ and protons, closes the circuit. An ion selective membrane (Nafion N117 proton selective membrane) ensures the migration and diffusion of protons inside the cell, avoiding homogenous reactions in the electrolyte solution and re-oxidation (or reduction) of the reaction products. The CO₂RR can generate a wide range of products, mainly from C₁ to C₂ molecules^{[38][39][40]} (figure 1.5), although small concentrations of C₆ products was recently reported by using nickel-oxygenate-derived electrocatalysts^[41]. Thermodynamically, the formation of hydrocarbons such as CH₄ and C₂H₄ is more favorable than CO formation, as they require a smaller potential bias. However, the activation energies of individual steps and the kinetics of multiple proton and electron transfers during the CO₂ reduction should also be considered. Since this reaction can produce a mixture of chemicals, selectivity remains a challenge, and energy intensive separation steps might be required to separate the products. The selectivity can be steered by the applied potential, the electrolyte solution composition and the electrocatalytic material.

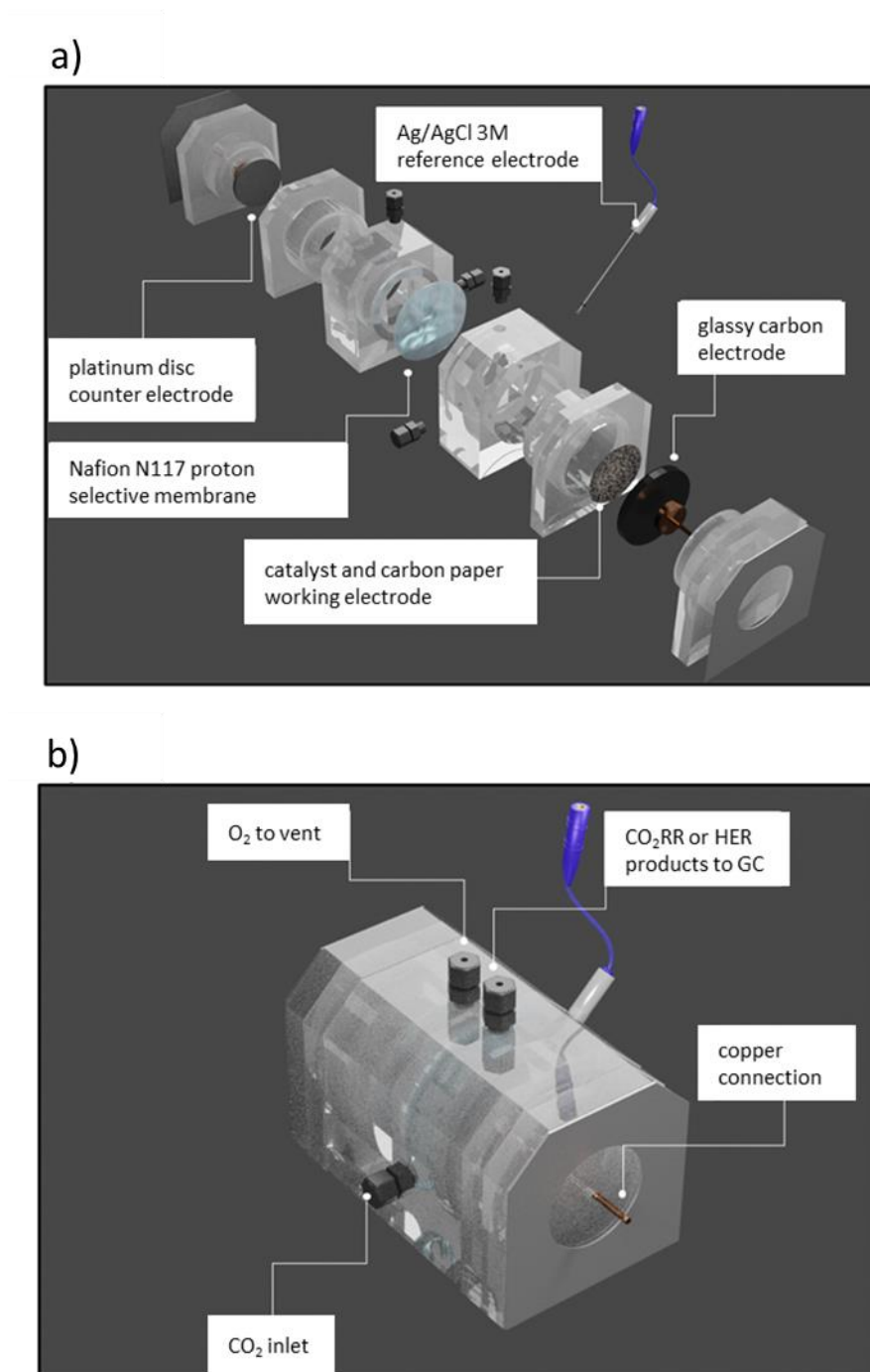
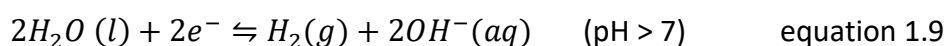


Figure 1.3 – Schematic representation of the custom-built electrochemical cell designed with the help of Sander Deelen. a) Open cell showing all individual components and b) closed cell emphasizing the external connections.

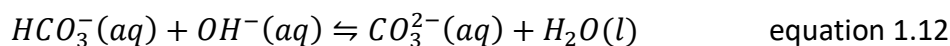
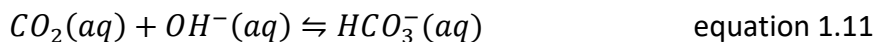
Hori and coworkers carefully classified the active electrocatalysts based on the reduction products generated (figure 1.4). Metals such as gold and silver, mostly produce

CO^[42], while tin is selective to formate^[43]. Nickel and platinum in their metallic state are great hydrogen formation catalysts^[44] and they show almost no activity towards CO₂RR. Copper enables further hydrogenation of CO and C-C coupling on its surface, hence generating both methane and C₂₊ products^[45]. Selectivity depends on the electronic properties of the metal catalysts which influence the binding strength and modes of the reactants, the intermediates and products on the metal surface. The correlation between activity towards specific products and binding energy is a volcano-shaped plot (the Sabatier principle). A too strong binding of reaction intermediates and/or products implies a high surface coverage and active sites poisoning. A too weak binding of intermediates and/or reactants leads to a low surface coverage, thus preventing their (further) reaction. Thus, an optimal catalyst shows a not-too-strong and not-too-weak bonding of key reaction intermediates^[46].

As mentioned previously, electrolyte plays a key role. Water is often used as solvent, as it provides H⁺ to react with CO₂, and it dissolves salts to increase the ionic conductivity. Nevertheless, water-based electrolytes have some drawbacks, such as the poor solubility of CO₂ in polar solvents (33 mM at 25 °C in water) and the low hydration strength of CO₂ in water. This can be mitigated by a high CO₂ pressure or by using gas diffusion electrodes to enable direct contact between gaseous CO₂ and the catalyst surface. Furthermore, water (equation 1.9) and proton reduction (equation 1.10) are competing with CO₂RR. Depending on the type of electrode, the H₂ evolution reaction (HER) can be kinetically favorable compared to CO₂RR, lowering the energy efficiency and selectivity of the process^{[39][40]}.



Near the electrode surface, the solution is affected by both the HER and CO₂RR, as either OH⁻ is formed, or protons are depleted during these reactions. The net effect is an increase in local pH compared to the bulk. This affects the kinetics of both the HER and CO₂RR, as many elemental steps involve H⁺ transfer. Another indirect effect of the increase in local pH is the change in local cation concentration^[49]. The local pH determines the maximum concentrations of dissolved CO₂, HCO₃⁻ and CO₃²⁻ as reflected in equations 1.11 and 1.12:



This limits the availability of CO_2 , which is the most reactive species, therefore decreases the CO_2RR partial current density. To cope with this, buffers, such as potassium bicarbonate, are often used in aqueous electrolytes, although they cannot fully stabilize the local pH. Many challenges still exist for the CO_2RR .

In the next section, we focus on how catalyst design can improve the activity and selectivity of the process, using silver and carbon as examples.

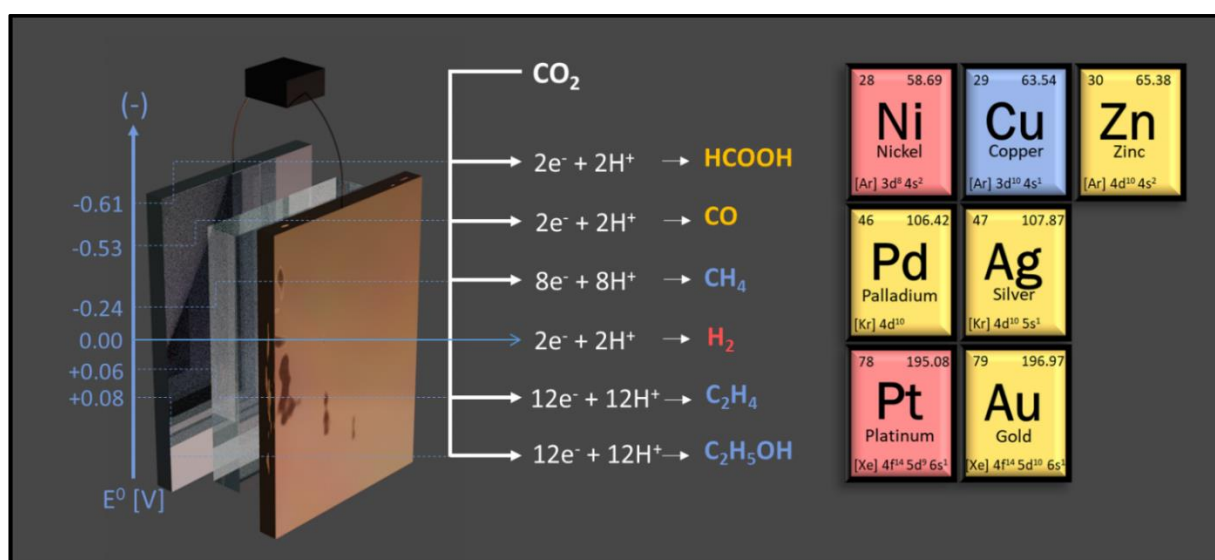


Figure 1.4 – CO_2RR products divided into four categories, according to the transition metals that generate the molecule.

1.5 CO₂ reduction to CO on silver and carbon

CO is a desirable product as it is used as building block for a wide range of chemicals, such as acetic acid^[50], phosgene^[51] and alcohols^[52]. In addition, long-chain hydrocarbons, methanol and fuels, can be synthesized from a mixture of CO and H₂ (syngas) over iron, cobalt, nickel or copper catalysts^[53]. Silver is a widely investigated electrocatalyst for the CO₂RR; its selectivity to CO is second only to gold^{[54][55][56]}. Besides CO, H₂ is produced, while only traces of formate have been detected^[57]. The reaction scheme for CO₂ reduction to CO is shown in figure 1.5a. Free energy calculations identify *COO⁻ as the key intermediate, formed *via* a single electron transfer between the metal surface and the electrophilic carbon in adsorbed CO₂^{[55][58]}. This activation step of CO₂, involves a structural rearrangement of the molecule, from linear to bent shape, and constitutes the rate determining step of the reaction. After a subsequent proton transfer, *CO is generated by the removal of a water molecule. The final step involves the desorption of *CO. This mechanism, until the formation of *CO, is at the basis of every C₁ and C₂ reduction product. The only exception is formate, which is generated *via* an oxygen-bidentate mechanism (figure 1.5b), and commonly is produced by p-block metals such as Sn or Pb. The well-known Volmer-Tafel-Heyrovsky mechanism for the HER (figure 1.5c) competes with the CO formation.

The high selectivity to CO is driven by the electronic surface properties of silver, which can absorb and reduce CO₂ to form the key intermediate *COO⁻. Electron density from the Ag d-band is back donated into the anti-bonding orbitals of adsorbed CO₂. Silver has an intermediate binding energy of this first reaction intermediate (*COO⁻), allowing further proton and electron transfer. The weak binding of *CO allows its rapid desorption.

Several researchers explored strategies to optimize silver-based electrodes^{[59][60]}. This involves geometric and electronic modification, such as the nano-crystallization of the metal, doping and surface modification^{[61][62][63]}. Moving from bulk to nanostructured electrodes gives a higher surface to volume ratio, but sometimes also a preference for CO₂RR over HER activity^[64]. This is attributed to an increase in crystal lattice strain and lower-coordinated surface atoms, such as edges^[65], being more active for the first electron transfer to CO₂^{[66][67][68]}. For instance, silver nanoparticles showed a size-dependent CO faradaic efficiencies, with an optimum found at 5 nm, corresponding to the highest edge to corner

ratio. Nevertheless, control over the silver nanoparticle size often requires the use of ligands, which in turn modifies the electronic structure of the particles^[69]. Surface modifications, such as sulfidation or oxidation-reduction of silver, allow to introduce defects and new active sites in the catalyst structure, changing the rate of the reaction^[70]. The silver morphology also affects catalyst selectivity, as different exposed crystal facets, with different electronic configurations and structural parameters, result in different activation barriers for the key reaction intermediates. Hence, preferential crystal growth, resulting in a large fraction of the 100 to 111 facets in nanowires or nanocubes, is another effective strategy to tune the CO production^[71]. The influence of different silver nanostructures will be discussed in chapter 3 and 5.

As nanostructures are thermodynamically unstable with respect to microcrystalline materials, a suitable support is needed. Carbon is an earth-abundant and low-cost material often used as a catalyst support. Its high surface area allows a fine dispersion of nanoparticles. The possibility to tune its surface properties also enables tuning of the properties of the supported metal nanoparticles^[72]. Traditionally used as capacitors and electrolyzers, the high conductivity of carbon boosted its application in electrocatalysis. The main drawback for carbon as an electrode material for CO₂ reduction is its tendency to form H₂ in aqueous solutions^[73]. Wu et al. reported that for pristine carbon nanotubes, H₂ dominated the products^[74]. This was attributed to the lack of active catalytic sites for CO₂RR. DFT calculations gave a large energy barrier (3.0 eV) to activate CO₂ on a defect-free graphite, considering the first electron transfer to adsorb CO₂ the rate determining step of the reaction^[72]. Heteroatoms and structural defects introduced into the graphitic carbon can act as active sites for CO₂RR, enhancing the CO and formate production^{[75][76][77]}. A detailed overview of the most important results achieved with modified-carbon-based electrodes is provided in chapter 2, which discusses the benefits of nitrogen-containing surface groups, and in chapter 4, in which the effects of enhancements of the carbon hydrophobicity (by alkylamine surface modification) on CO₂RR is described.

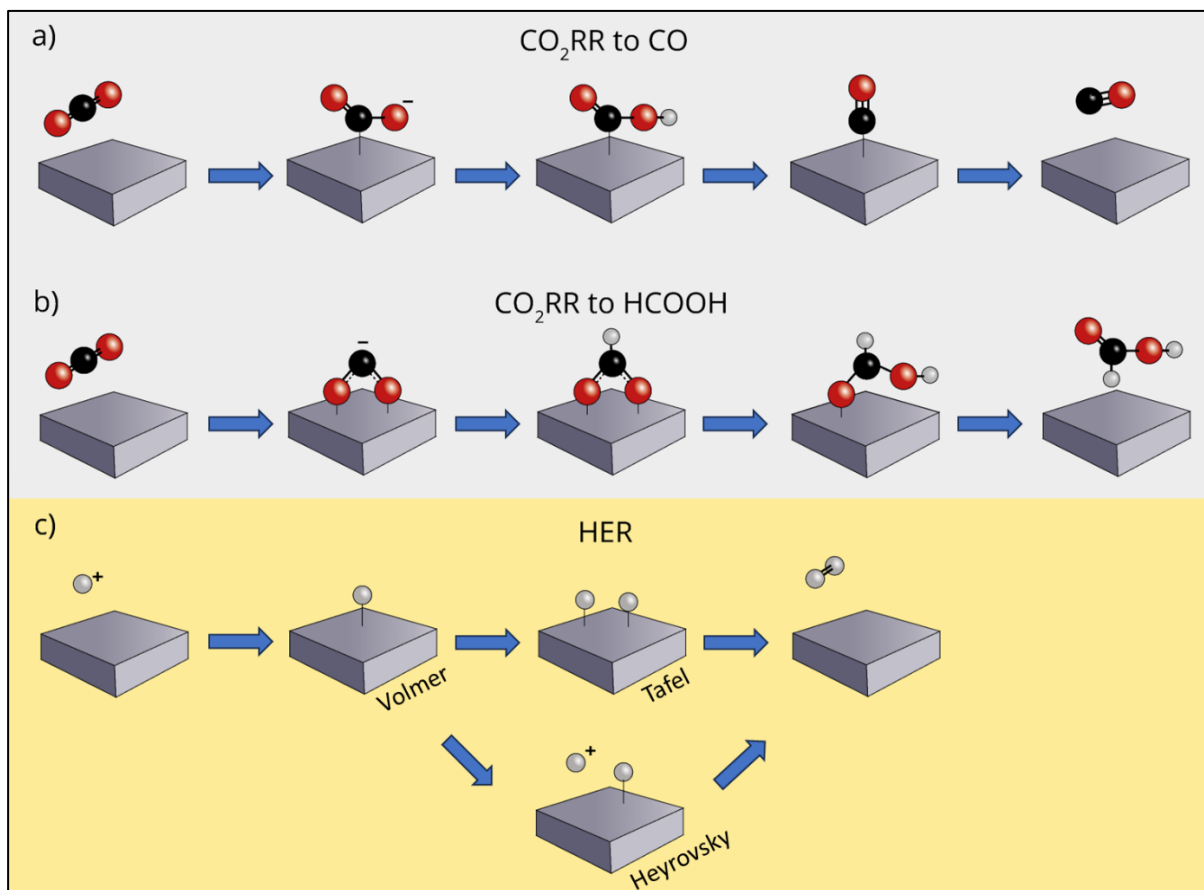


Figure 1.5 – a) CO₂RR to CO mechanism, b) mechanism underlying formate production and c) HER mechanism.

1.6 Scope of this thesis

The scope of this thesis is understanding the key parameters that influence the selectivity of carbon, and carbon supported silver catalysts during the CO₂RR to CO. This includes both the synthesis, characterization and testing of carbon and silver-based cathode materials. During the synthesis, we focused on the effects of the surface chemistry of carbon, and the morphology and size of silver nanocatalysts. Physical and chemical properties of the prepared materials were characterized by transmission electron microscopy, scanning electron microscopy, x-ray powder diffraction, x-ray photoelectron spectroscopy, acid-base titration, point of zero charge analysis and contact angle measurements. Finally, we correlated activity and selectivity descriptors, such as current density and faradaic efficiency, to the material surface properties.

In chapter 2, starting from previous knowledge on thermal catalysis and synthesis of stable materials for gas phase reactions, we began this project by investigating the effects of surface functionalization/modification on the CO₂RR to CO on high surface area carbon materials. To achieve this, we introduced acidic oxygen-containing groups and basic nitrogen-containing groups on the carbon to tune the electronic properties. We also removed all the surface group *via* an H₂ treatment to clearly study the effect of the acidic and basic surface groups. This work led to unraveling the selectivity of the different surface groups, demonstrating that the N- containing groups are more selective towards CO.

In chapter 3, we discuss silver particle size effect by synthesizing ligand-free silver nanoparticles supported on high surface area carbon materials. Building on the knowledge gained in chapter 2, we achieved control over the silver particle size by functionalizing the carbon substrate with acidic surface groups and exploiting electrostatic interactions between the silver precursor and the support. We compared the performance of three catalysts with different particle sizes in the 10-30 nm range. The selectivity was dominated by the HER, due to the high surface area carbon materials. The current density for CO formation, normalized by silver mass, is larger for smaller particles. No differences were found if the CO current was normalized per active surface area, showing that in this range the nanoparticle size does not significantly influence the type or the number of active sites per unit area.

In chapter 4, we elaborate on suppressing the H_2 formation over high surface area carbon by introducing alkylamine surface groups. This resulted in hydrophobic carbon electrodes with large contact angles and with electrostatic interactions with the alkylamines. With a low silver loading ($0.0016 \text{ mg}_{\text{Ag}} \text{ cm}^{-2}$), produced by colloidal synthesis, we explored the effect of different linear alkylamine chain lengths on the selectivity towards CO. Functionalization led to suppression of the HER, and boosted CO production, probably due to the hydrophobic groups shielding the carbon surface.

Chapter 5 is dedicated to silver nanowires, which present a high 100 to 111 facet ratio, reportedly favorable for the CO_2RR to CO. Starting from the CO selective catalysts (silver nanowire), we introduced surface defects (by controlled electrochemical oxidation) to investigate the effects on the selectivity. Interestingly, the CO selectivity increased further with increasing oxidation potential, indicating that either new active (defected) sites were formed, or the local environment positively affected the reaction selectivity.

Finally, in chapter 6, the overall summary of the thesis, both in English and in Dutch, and some perspective for the future research on CO_2RR to CO are presented.

In summary, with this work, we tried to correlate specific surface parameters to the electrocatalytic performance of silver and carbon-based electrodes, building understanding on how to steer the selectivity of the CO_2RR towards CO.

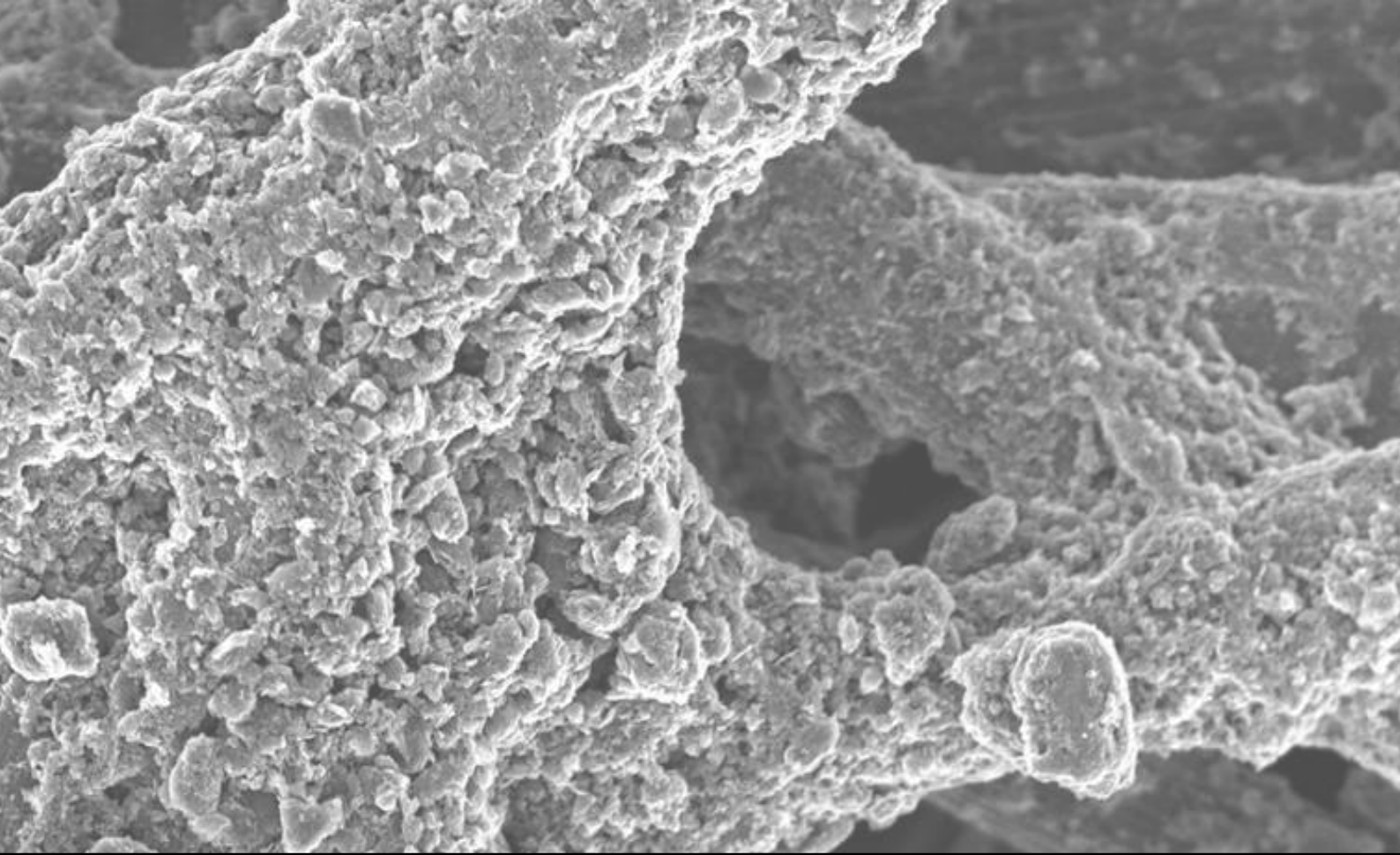
References

- [1] G. S. Malhi, M. Kaur, P. Kaushik, *Sustainability* **2021**, *13*, 1–21.
- [2] V. Masson-Delmotte, P. Zhai, H.-O. Pörtner, D. Roberts, J. Skea, P. R. Shukla, A. Pirani, W. Moufouma-Okia, C. Péan, R. Pidcock, S. Connors, J. B. R. Matthews, Y. Chen, X. Zhou, M. I. Gomis, E. Lonnoy, T. Maycock, and T. W. M. Tignor, **2019**.
- [3] C. Bohringer, *Oxford Review of Economic Policy* **2003**, *19*, 451–466.
- [4] A. Savaresi, *Journal of Energy & Natural Resources Law* **2015**, *34*, 16–26.
- [5] M. Biggeri, *J. Hum. Dev. Capab.* **2021**, *22*, 706–712.
- [6] R. Van Tulder, S. B. Rodrigues, H. Mirza, K. Sexsmith, *J. Int. Bus. Policy* **2021**, *4*, 1–21.
- [7] V. Kumaravel, J. Bartlett, S. C. Pillai, *ACS Energy Lett.* **2020**, 486–519.
- [8] R. J. Detz, B. van der Zwaan, *Energy Policy* **2019**, *133*, 110938.
- [9] J. C. Abanades, E. S. Rubin, M. Mazzotti, H. J. Herzog, *Energy Environ. Sci.* **2017**, *10*, 2491–2499.
- [10] H. Chen, T. N. Cong, W. Yang, C. Tan, Y. Li, Y. Ding, *Prog. Nat. Sci.* **2009**, *19*, 291–312.
- [11] T. Hatsukade, K. P. Kuhl, E. R. Cave, D. N. Abram, T. F. Jaramillo, *Phys. Chem. Chem. Phys.* **2014**, *16*, 13814–13819.
- [12] P. Atkins, J. de Paula, *Physical Chemistry*, W. H. Freeman, New York, **2006**.
- [13] M. Ozkan, S. P. Nayak, A. D. Ruiz, W. Jiang, *iScience* **2022**, *25*, 103990.
- [14] A. Badgett, A. Feise, A. Star, *iScience* **2022**, *25*, 104270.
- [15] N. McQueen, K. V. Gomes, C. McCormick, K. Blumanthal, M. Pisciotta, J. Wilcox, *Prog. Energy* **2021**, *3*, 1–22.
- [16] D. L. T. Nguyen, Y. Kim, Y. J. Hwang, D. H. Won, *Carbon Energy* **2020**, *2*, 72–98.
- [17] D. Bogdanov, M. Ram, A. Aghahosseini, A. Gulagi, A. S. Oyewo, M. Child, U. Caldera, K. Sadovskaia, J. Farfan, L. De Souza Noel Simas Barbosa, M. Fasihi, S. Khalili, T. Traber, C. Breyer, *Energy* **2021**, *227*, 120467.
- [18] A. J. Bard, L. R. Faulkner, *Electrochemical Methods*, John Wiley & Sons, **2001**.
- [19] W. Xiao, R. S. Wang, D. E. Handy, J. Loscalzo, *Antioxidants Redox Signal.* **2018**, *28*, 251–272.
- [20] G. Pancaldi, *Hist. Stud. Phys. Biol. Sci.* **1990**, *21*, 123–160.
- [21] J. L. Brédas, J. M. Buriak, F. Caruso, K. S. Choi, B. A. Korgel, M. R. Palacín, K. Persson,

- E. Reichmanis, F. Schüth, R. Seshadri, M. D. Ward, *Chem. Mater.* **2019**, *31*, 8577–8581.
- [22] K. Zhang, X. Liang, L. Wang, K. Sun, Y. Wang, Z. Xie, Q. Wu, X. Bai, M. S. Hamdy, H. Chen, X. Zou, *Nano Res. Energy* **2022**, *1*, e9120032.
- [23] C. M. A. Brett, A. M. O. Brett, *Electrochemistry*, Oxford Pree, **1994**.
- [24] A. J. Bard, L. R. Faulkner, *Electrochemical Methods*, John Wiley & Sons, **2001**.
- [25] B. N. Ciribelli, F. Colmati, E. C. de Souza, *Int. J. Innov. Educ. Res.* **2020**, *8*, 670–683.
- [26] J. V. A. Butler, *Trans. Faraday Soc.* **1924**, *19*, 729–733.
- [27] T. . Erdey-Grúz, M. Volmer, **1930**, 203–213.
- [28] J. Tafel, *Zeitschrift für Phys. Chemie* **1905**, 641–712.
- [29] P. Khadke, T. Tichter, T. Boettcher, F. Muench, W. Ensinger, C. Roth, *Sci. Rep.* **2021**, *11*, 8974.
- [30] G. Q. Lu, A. Wieckowski, *Curr. Opin. Colloid Interface Sci.* **2000**, *5*, 95–100.
- [31] J. Crook, A. Mousavi, *Environ. Forensics* **2016**, *17*, 211–217.
- [32] B. Timmer, M. Sluyters-Rehbach, J. H. Sluyters, *Surf. Sci.* **1969**, *18*, 44–61.
- [33] M. Breiter, M. Kleinerman, P. Delahay, *J. Am. Chem. Soc.* **1958**, *80*, 5111–5117.
- [34] G. C. Gschwend, H. H. Girault, *Chem. Sci.* **2020**, *11*, 10304–10312.
- [35] A. Frumkin, A. Gorodetskaja, *Zeitschrift für Phys. Chemie* **1928**, 451–472.
- [36] R. Parsons, in *J. Electroanal. Chem.*, **1969**, 35–43.
- [37] M. A. Habib, J. O. Bockris, in *Compr. Treatise Electrochem.*, Springer US, **1980**, 135–219.
- [38] Y. Hori, in *Mod. Asp. Electrochem.*, Springer New York, New York, NY, **2008**, 89–189.
- [39] Y. Hori, R. Takahashi, Y. Yoshinami, A. Murata, *J. Phys. Chem. B* **1997**, *101*, 7075–7081.
- [40] Y. Hori, S. Suzuki, *Bull. Chem. Soc. Jpn.* **1982**, *55*, 660–665.
- [41] Y. Zhou, A. J. Martín, F. Dattila, S. Xi, N. López, J. Pérez-Ramírez, B. S. Yeo, *Nat. Catal.* **2022**, *5*, 545–554.
- [42] Y. Hori, H. Wakabe, T. Tsukamoto, O. Koga, *Electrochim. Acta* **1994**, *39*, 1833–1839.
- [43] R. Daiyan, X. Lu, Y. H. Ng, R. Amal, *Catal. Sci. Technol.* **2017**, *7*, 2542–2550.
- [44] A. B. Laursen, A. S. Varela, F. Dionigi, H. Fanchiu, C. Miller, O. L. Trinhammer, J. Rossmeisl, S. Dahl, *J. Chem. Educ.* **2012**, *89*, 1595–1599.

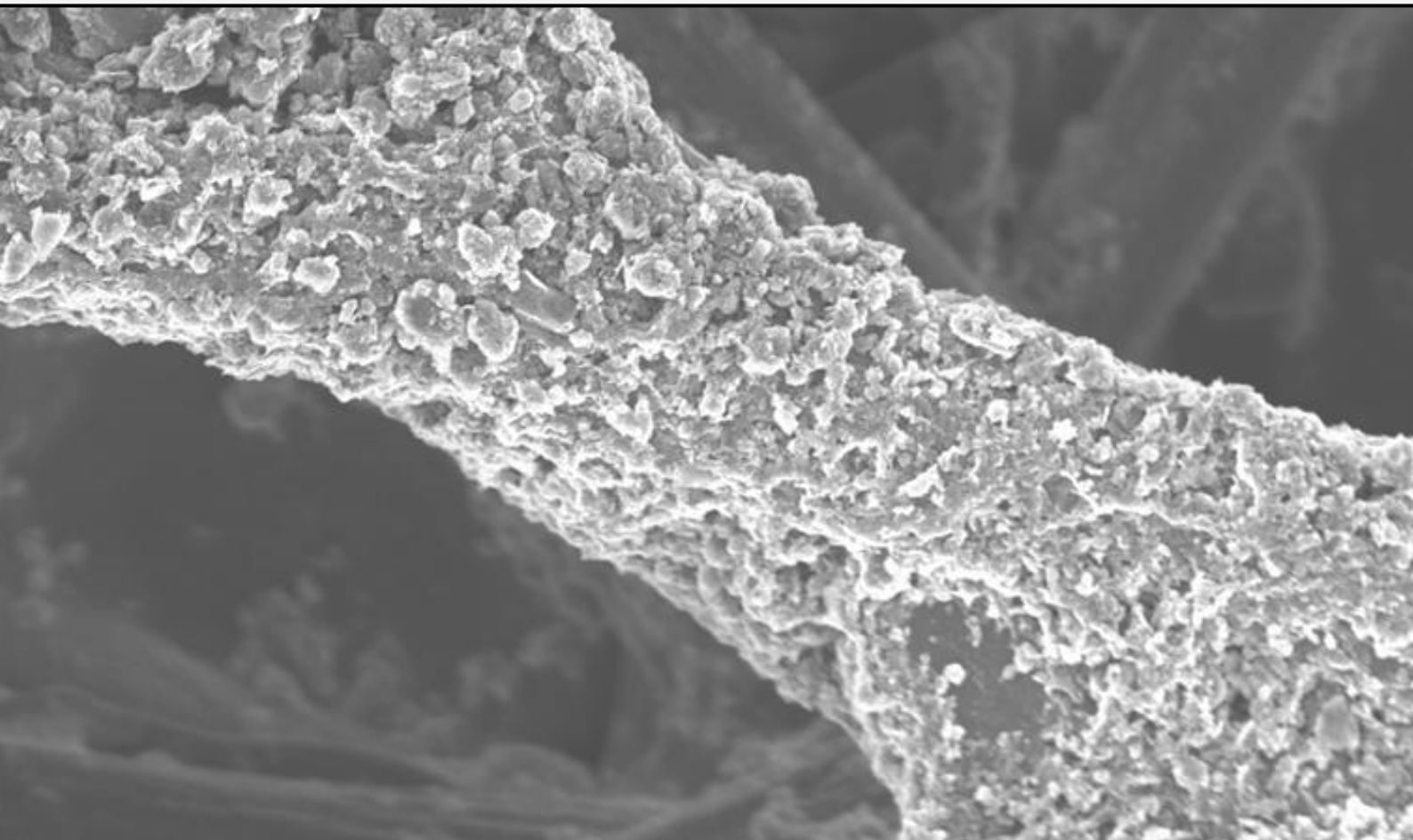
- [45] Y. Hori, I. Takahashi, O. Koga, N. Hoshi, *J. Mol. Catal. A Chem.* **2003**, *199*, 39–47.
- [46] H. Ooka, J. Huang, K. S. Exner, *Front. Energy Res.* **2021**, *9*, 1–20.
- [47] A. Goyal, G. Marcandalli, V. A. Mints, M. T. M. Koper, *J. Am. Chem. Soc.* **2020**, *142*, 4154–4161.
- [48] C. J. Bondue, M. Graf, A. Goyal, M. T. M. Koper, *J. Am. Chem. Soc.* **2021**, *143*, 279–285.
- [49] A. Goyal, M. T. M. Koper, *Angew. Chemie - Int. Ed.* **2021**, *60*, 13452–13462.
- [50] G. J. Sunley, D. J. Watson, *Catal. Today* **2000**, *58*, 293–307.
- [51] G. E. Rossi, J. M. Winfield, C. J. Mitchell, N. Meyer, D. H. Jones, R. H. Carr, D. Lennon, *Appl. Catal. A Gen.* **2020**, *602*, 2–9.
- [52] H. C. Woo, I. S. Nam, J. S. Lee, J. S. Chung, K. H. Lee, Y. G. Kim, *J. Catal.* **1992**, *138*, 525–535.
- [53] H. Schulz, *Appl. Catal. A Gen.* **1999**, *186*, 3–12.
- [54] N. J. Firet, T. Burdyny, N. T. Nesbitt, S. Chandrashekar, A. Longo, W. A. Smith, *Catal. Sci. Technol.* **2020**, *10*, 5870–5885.
- [55] J. T. Feaster, C. Shi, E. R. Cave, T. Hatsukade, D. N. Abram, K. P. Kuhl, C. Hahn, J. K. Nørskov, T. F. Jaramillo, *ACS Catal.* **2017**, *7*, 4822–4827.
- [56] M. Ma, B. J. Trzeźniewski, J. Xie, W. A. Smith, *Angew. Chemie - Int. Ed.* **2016**, *55*, 9748–9752.
- [57] Y. W. Choi, F. Scholten, I. Sinev, B. R. Cuenya, *J. Am. Chem. Soc.* **2019**, *141*, 5261–5266.
- [58] D. Sun, X. Xu, Y. Qin, S. P. Jiang, Z. Shao, *ChemSusChem* **2020**, *13*, 39–58.
- [59] Y. Wang, C. Niu, Y. Zhu, *Nanomaterials* **2019**, *9*, 173–183.
- [60] S. Li, X. Dong, W. Chen, Y. Song, G. Li, W. Wei, Y. Sun, *Catalysts* **2022**, *12*, 1–11.
- [61] X. Deng, D. Alfonso, T. D. Nguyen-Phan, D. R. Kauffman, *ACS Catal.* **2022**, *12*, 5921–5929.
- [62] T. T. H. Hoang, S. Verma, S. Ma, T. T. Fister, J. Timoshenko, A. I. Frenkel, P. J. A. Kenis, A. A. Gewirth, *J. Am. Chem. Soc.* **2018**, *140*, 5791–5797.
- [63] M. Abdinejad, E. Irtem, A. Farzi, M. Sassenburg, S. Subramanian, H. P. Iglesias Van Montfort, D. Ripepi, M. Li, J. Middelkoop, A. Seifitokaldani, T. Burdyny, *ACS Catal.* **2022**, *12*, 7862–7876.

- [64] J. Pérez-Ramírez, N. López, *Nat. Catal.* **2019**, *2*, 971–976.
- [65] N. Jeyachandran, W. Yuan, C. Giordano, *Molecules* **2023**, *28*, 3504–3526.
- [66] A. Loiudice, O. Segura Lecina, R. Buonsanti, *ACS Mater. Lett.* **2020**, *2*, 1182–1202.
- [67] S. E. Skrabalak, L. Au, X. Li, Y. Xia, *Nat. Protoc.* **2007**, *2*, 2182–2190.
- [68] A. Tao, P. Sinsermsuksakul, P. Yang, *Angew. Chemie - Int. Ed.* **2006**, *45*, 4597–4601.
- [69] C. Kim, H. S. Jeon, T. Eom, M. S. Jee, H. Kim, C. M. Friend, B. K. Min, Y. J. Hwang, *J. Am. Chem. Soc.* **2015**, *137*, 13844–13850.
- [70] L. Wei, H. Li, J. Chen, Z. Yuan, Q. Huang, X. Liao, G. Henkelman, Y. Chen, *ACS Catal.* **2020**, *10*, 1444–1453.
- [71] L. Zeng, J. Shi, H. Chen, C. Lin, *Energies* **2021**, *14*, 2840–2850.
- [72] G. L. Chai, Z. X. Guo, *Chem. Sci.* **2016**, *7*, 1268–1275.
- [73] Z. Sun, T. Ma, H. Tao, Q. Fan, B. Han, *Chem* **2017**, *3*, 560–587.
- [74] J. Wu, R. M. Yadav, M. Liu, P. P. Sharma, C. S. Tiwary, L. Ma, X. Zou, X. D. Zhou, B. I. Yakobson, J. Lou, P. M. Ajayan, *ACS Nano* **2015**, *9*, 5364–5371.
- [75] F. Pan, B. Li, W. Deng, Z. Du, Y. Gang, G. Wang, Y. Li, *Appl. Catal. B Environ.* **2019**, *252*, 240–249.
- [76] S. Liu, H. Yang, X. Huang, L. Liu, W. Cai, J. Gao, X. Li, T. Zhang, Y. Huang, B. Liu, *Adv. Funct. Mater.* **2018**, *28*, 1800499.
- [77] J. Yuan, W. Y. Zhi, L. Liu, M. P. Yang, H. Wang, J. X. Lu, *Electrochim. Acta* **2018**, *282*, 694–701.



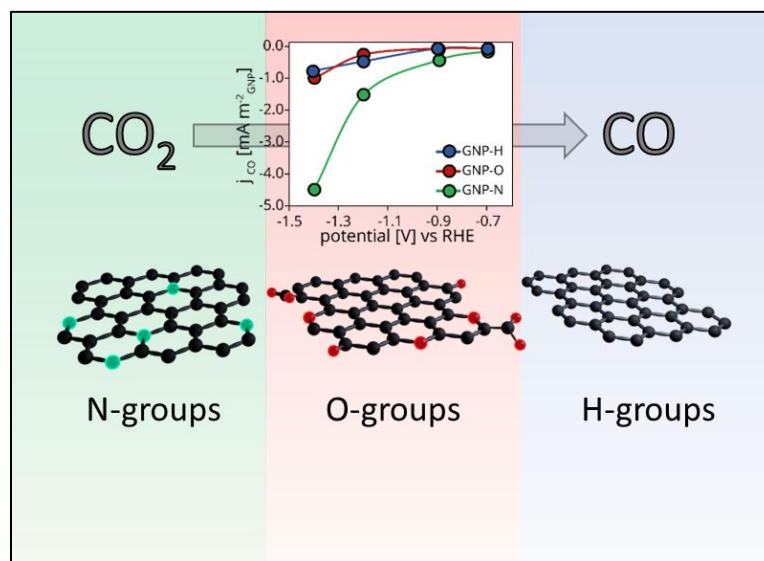
CHAPTER 2

Surface-modified carbon materials



Abstract

The electrochemical reduction of CO₂ to produce sustainable fuels and chemicals has attracted great attention in recent years. This chapter reports a strategy to modify the surface of commercially available carbon materials by adding oxygen and nitrogen surface groups without modifying its graphitic structure. Clear differences in CO₂RR activity, selectivity and the turnover frequency between the surface-modified carbons were observed, and these differences were ascribed to the nature of the surface groups chemistry and the point of zero charge (PZC). The results show that nitrogen-containing surface groups are highly selective towards the formation of CO from the electroreduction of CO₂ in comparison with the oxygen-containing surface groups, and the carbon without surface groups. This demonstrates that the selectivity of carbon for CO₂RR can be rationally tuned by simply altering the surface chemistry *via* surface functionalization.



This chapter is based on the following publication:

Francesco Mattarozzi, Marisol Tapia Rosales, Rim van de Poll, Emiel Hensen, Peter Ngene and Petra de Jongh, 'Surface-modified carbon materials for CO₂ electroreduction', *European Journal of Inorganic Chemistry*, **2023**, e202300152.

2.1 Introduction

Carbon-based materials gained much interest as electrocatalysts, due to their low cost and abundance, their high electrical conductivity, and the possibility to tune their textural properties and surface chemistry. The main drawback for carbon as an electrode material for electrochemical CO₂ reduction is its low selectivity towards CO₂ over H⁺ reduction, hence forming mostly hydrogen in aqueous solution. Its poor electrocatalytic performance relates to the inert surface of graphite, which makes it dependent on surface defects as active sites^[1]. Hence, heteroatoms and structural defects have been introduced in the graphitic carbon matrix to improve the catalytic performance^[2–8]. It was shown that by synthesizing carbon monolith with high nitrogen content (0.28 wt%), it was possible to increase the CO₂ adsorption of activated carbon 1.5-times (mmol CO₂ adsorbed per gram of material) at 25 °C and 1 bar^[9]. In electrocatalysis, different research groups reported that nitrogen-doped carbon materials enhanced selectivity towards the CO₂RR^{[10][11][12][13][14]}. This has been ascribed to the strong adsorption of the electrophilic CO₂ carbon atom on the electron-rich nitrogen atoms at the carbon electrode surface^[15]. This leads to a lower activation energy to generate the first reaction intermediate *COO[−] and hence a faster first electron transfer to CO₂, compared to pure graphitic carbons. Hence, high concentration of nitrogen atoms in the carbon structure or nitrogen-containing surface groups are favorable.

Two main strategies are commonly adopted for the synthesis of N-doped carbon electrocatalysts: top-down approaches (hydrothermal, mechanical exfoliation, plasma treatment and arc-discharge method) and bottom-up approaches (chemical vapor deposition, solvothermal method and free-radical polymerization)^{[16][17]}. The former generally use commercially available carbons as starting materials, while the latter use nitrogen rich organic compounds as precursors, which allow to tune the nitrogen content in the graphene layers^[17]. For instance, the synthesis of N-doped graphene quantum dots *via* a multi-step procedure, involving the oxidation of commercially available graphite powder, graphene oxide exfoliation and functionalization with dimethylformamide, represents an example of top-down approach^[16]. This carbon-based electrocatalyst possessed 6 at% N atoms and produced C₂ (31% FE) and C₂ oxygenated products (26% FE) at -0.75 V vs RHE. Alternatively, imidazole-type groups were introduced on the surface of oxidized graphitic carbon materials by exploiting the high reactivity of thionyl chloride to generate an acid chloride intermediate, achieving a 35%

selectivity towards ethanol at -1.0 mA cm^{-2} [18]. Other groups focused their attention on synthesis routes that allow good control over the catalyst morphology and nitrogen content. For instance, it has been shown that starting from different molar ratios of L-cysteine and melamine precursors, it is not only possible to control the total nitrogen content in the pyrolyzed carbon matrix in the range between 3.9 at% and 5.8 at%, but also to tune the pyridinic to pyrrolic groups ratio from 1.2 to 0.7. A good correlation between higher pyridine atomic percentage and CO productivity was found, as the CO partial current density linearly increase with the pyridinic nitrogen content^[19].

Besides nitrogen-modified carbon, some researchers have also looked at the effect of oxygen-containing functional groups on the CO₂RR. Typically, either an acidic treatment at high temperatures or oxygen plasma treatment are used to introduce oxygen-containing groups on the surface^{[3][20]}. Yang *et al.* recently showed a linear increase in the formate selectivity with increasing number of carboxylic groups, and proposed a synergistic effect between carboxylic groups and other oxygen-containing moieties (hydroxy, epoxide, and carbonyl) that steered the selectivity towards formate production (80% FE)^[20].

As previously investigated multi-step methods were laborious, in this chapter we discuss a simple and scalable procedure to modify the surface of commercially available carbon materials, to specifically probe the effects of the surface properties of carbon on the electrocatalytic activity and selectivity towards the CO₂RR. Oxygen-containing surface groups were introduced *via* a single-step liquid phase oxidation procedure. Nitrogen-containing groups were anchored on the carbon surface through gas-phase amination after the oxidation procedure, while carbon with negligible surface groups was obtained by removing surface groups through a gas-phase reduction in hydrogen. The careful characterization allowed us for the first time to quantify the intrinsic activity (turnover frequency) of specific CO₂RR active sites, proving the remarkable performance of pyridine-like surface groups for CO production.

2.2 Experimental section

2.2.1 Modification of carbon materials

The modification of the graphitic carbon was performed by three different treatments. Surface oxidized carbon was obtained by liquid-phase oxidation using concentrated nitric acid^[21]. Typically, 10 g of the as-received carbon (XGnP500, XG Science) material was suspended in 50 ml $\text{g}_{\text{carbon}}^{-1}$ HNO_3 (Sigma Aldrich, 65% wt/wt), inside a 1 L round bottom flask fitted with a reflux condenser. The suspension was heated to 80 °C, and kept at 80 °C for 120 min. Subsequently, the suspension was quenched by diluting it with deionized water. The solid carbon material sedimented on the bottom of the flask, and the supernatant was removed. The carbon material was washed rigorously with deionized water until the washing liquid reached a pH of around 7. Finally, the carbon powder was dried overnight at 120 °C. The surface-oxidized carbon is referred to as GNP-O. The final yield from the preparation of the GNP-O was 90%. This treatment was previously reported for the introduction of various oxygen-containing functional groups with a predominant surface coverage of carboxylic acid groups without having a significant change in the carbon crystal structure^{[22][23][24][25][26]}. The reduced carbon (GNP-H) was obtained by treating oxidized GNP (0.3 g) in a flow of 20% H_2 and 80% Ar at a rate of 400 mL min^{-1} at 400 °C for 12 h. The H_2 reduction treatment was meant to remove oxygen functional groups from the surface of the carbon (80% yield)^{[22][25]}. Amination treatment was performed with gaseous NH_3 at 600 °C at a flow rate of 0.25 L min^{-1} per 0.3 g of carbon. This incorporates nitrogen-containing functional groups at the carbon surface^{[25][27][28][29]} which in this work is referred to as GNP-N.

2.2.2 Working electrode preparation

The preparation of the working electrode was performed in three steps. First, a catalyst ink was prepared by mixing 11.8 mg modified carbon catalyst (sieve fraction < 75 μm), 1120 μL isopropanol (Sigma Aldrich, 99.5%), 4470 μL MQ water and 44.4 μL Nafion solution (Sigma Aldrich, 5.0% in a mixture of aliphatic alcohols and water). The ink was sonicated for 45 min in an ultrasonic bath to ensure a good dispersion of the catalyst powder in the Nafion containing solution. The resulting ink was sprayed onto a circular-shaped carbon paper

substrate (Toray, TGP-H-060) with a surface area of 4.9 cm² using an airbrush. Prior to the deposition of the catalyst, the carbon paper substrate was washed with ethanol under sonication for 30 minutes, and subsequently rinsed with milli-Q water. A catalyst loading of 0.2 mg cm⁻² was intended for all electrodes. The prepared electrodes were dried under vacuum overnight before each electrochemical testing.

2.2.3 Carbon characterization

To better understand the structure-selectivity relationship, we performed physical and chemical analyses on the modified carbon materials. The modified carbon catalysts were characterized using N₂-physisorption performed in a Micromeritics TriStar 3000 V6.08. Before the measurements, the carbon-based catalysts were dried at 170 °C under N₂-flow for 16 hours. The isotherms were measured at -196 °C using carbon black as a reference. The specific surface area was calculated using the multipoint Brunauer-Emmet-Teller (BET) method with p/p_0 between 0.05-0.25. The pore diameter was determined using the Barrett-Joyner-Halenda (BJH) method and the pore volume was determined as single point pore volume at $p/p_0=0.995$. Scanning Electron Microscopy (SEM) measurements of the surface-modified carbon on carbon paper were performed on the Phenom ProX from Thermo Fisher, operated at 10 kV. X-ray diffraction (XRD) measurements were done on a Bruker D2 Phaser, equipped with a Co K α X-ray source with a wavelength of 1.79026 Å. The point of zero charge of the carbon materials was measured by titration using a pH meter TitraLab. The amount of acidic and basic surface groups was determined in separate measurements. Typically, 25 mg of modified carbon was suspended in 65 mL of 0.1 M KCl solution. The suspension was degassed with N₂ for 5 minutes under vigorous stirring. The titrations were performed using solutions of either 0.01 M NaOH or 0.01 M HCl, in 0.1 M KCl electrolyte. The acidic and basic groups densities were calculated from the titration curve showing the change in pH as a function of the volume of titrant. The inflection points on the curves were identified using the second derivative of the fitted curves. The inflection point corresponds to the titrant volume necessary to titrate the surface groups of the carbon, therefore at the inflection point, the moles of titrant are equal to the moles of surface groups on the carbon surface. This method is extensively used to measure the amount of surface groups present on materials

surfaces^{[21][22][23][24][25]}. The XPS data were collected by using ThermoFischer Thermo Scientific K-Alpha X-ray Photoelectron Spectrometer System, with an Al source ($K\alpha$ monochromatic radiation 1486.6 eV). The deconvolution of the carbon, oxygen and nitrogen peaks was performed by using CasaXPS. These measurements enable a better understanding of the influence of these surface groups on the activity and selectivity of the carbon material in the CO₂ reduction reaction.

2.2.4 Electrochemical measurements

The electrochemical measurements were performed in a custom-built H-type electrochemical cell (figure 1.3) with cathode and anode compartments separated by a Nafion membrane (Ion Power, Nafion N117). 15 mL of 0.1 M KHCO₃ (Sigma Aldrich, >99.0%) electrolyte at pH 7.5 was used in each compartment. The anolyte was constantly purged with argon and the catholyte was purged with CO₂ at 20 ml min⁻¹. The electrochemical measurements were performed with an Autolab PGSTAT204 Potentiostat, using a Pt disk (Metrohm, 99.5%) as a counter electrode and a Ag/AgCl 3 M KCl reference electrode (Metrohm).

The modified-carbon catalysts deposited onto the carbon paper substrate were placed on a glassy carbon disk (HTW-Germany) with 3 cm diameter, which acted as an extra support for the carbon paper, and as the current collector. The glassy carbon and the carbon paper were held in place by O-shaped gaskets, leaving an electrode area of 3.8 cm² exposed to the electrolyte solution. The electrolyte was bubbled with CO₂ for 20 minutes before every electrocatalytic test, to achieve a homogeneous CO₂-saturation of the electrolyte, resulting in a pH of 6.8.

Chronoamperometry measurements for 45 minutes at different potentials were performed to determine the selectivity. The gaseous products were analyzed by an on-line gas chromatograph (Global Analysis Solutions Microcompact GC 4.0). The GC system was equipped with three channels. The first channel has an Rt-QBond (10 m*0.32 mm, Agilent) packed column and an FID detector for the detection of CH₄, C₂H₄ and C₂H₆, the second channel has a Molecular Sieve 5A (10 m* 0.53 mm, Restek) packed column that separates small gaseous molecules such as CO and CH₄. This channel has an FID detector with a methanizer to increase the detection sensitivity of CO. The third channel has a Carboxen 1010

(8m*0.32mm, Agilent) packed column which separates H₂ and CO₂ with a TCD detector. High purity nitrogen (N₂; 99.999%) was used as a carrier gas.

Liquid phase products were analyzed using a Varian HPLC equipped with a refractive index detector (RID) and a Bio-Rad Aminex HPX-87H column at 65 °C. 1 mM H₂SO₄ was used as the eluent with a flow rate of 0.55 mL min⁻¹. The retention time of formic acid was 15 minutes, and the total analysis time was 20 minutes.

The obtained potentials were converted to the reversible hydrogen electrode (RHE) potentials using equation 2.1:

$$E_{RHE} = E_{Ag/AgCl} + 0.209 + 0.059 pH \quad \text{equation 2.1}$$

The Faradaic efficiency for each modified carbon (FE) was calculated as shown in equation 2.2:

$$FE(\%) = \frac{n_x * F * [\text{moles of product } x]}{Q} * 100\% \quad \text{equation 2.2}$$

In which n_x is the number of electrons needed to produce x product from CO₂ molecules and F is the Faradaic constant.

For gaseous products ($x = \text{H}_2, \text{CO}, \text{and } \text{CH}_4$), the moles of the product were determined *via* equation 2.3:

$$\text{moles of product} = \frac{C_x * q * p}{R * T} \quad \text{equation 2.3}$$

in which C_x is the volumetric concentration of product x in ppm extracted from the GC calibration plot, q is the gas flow rate, p is the pressure, R is the ideal gas constant (8.314 m³ Pa K⁻¹ mol⁻¹), T is the temperature, n_x is the number of reduced electrons needed to produce x (product) from CO₂ molecules and F is the Faradaic constant (96485 s A mol⁻¹).

For liquid-phase products ($x = \text{formic acid}$), the moles of product formed were determined *via* equation 2.4:

$$\text{moles of product} = \frac{C_x * V_{\text{catholyte}}}{1000 * M_w} \quad \text{equation 2.4}$$

in which C_x is the volumetric concentration of product x in ppm extracted from the HPLC calibration curve, $V_{\text{catholyte}}$ is the volume of the catholyte (L) and M_w the molar weight of product x (g mol⁻¹).

The turnover frequency (TOF), which corresponds to the intrinsic selectivity of the surface groups to CO, was calculated per mol of surface groups, using equation 2.5:

$$TOF = \frac{j}{mol_{groups} * F * n} \quad \text{equation 2.5}$$

Where j is the partial current of each individual product (CO), The total moles of surface groups (mol_{groups}) was calculated by multiplying the surface area of the carbon (m^2) by the density of surface groups ($n^\circ m^{-2}$) based on the theoretical weight of the surface-modified carbon over the carbon paper, finally the result is divided by the Avogadro's number to obtain moles of surface groups (mol). F is the Faraday constant, and n is the number of electrons needed to produce the product of interest.

2.3 Results and discussion

2.3.1 Tuning the surface properties of graphitic carbon

We modified pristine commercial carbon graphene nanoplatelets (GNP-P) by three different methods. The carbon was first oxidized in concentrated nitric acid (GNP-O) and then converted into either nitrogen-modified carbon (GNP-N) *via* gas phase amination or H₂-reduced carbon (GNP-H). These treatments introduced different functional groups on the carbon surface which allowed to study the effect of these groups on the electrocatalytic performance. The physical properties of the surface-modified carbons are summarized in table 2.1.

Table 2.1 - Surface area and porosity of the modified carbons.

Sample	BET surface area [m ² g ⁻¹]	Total pore volume [mL g ⁻¹]
GNP-P	490	0.84
GNP-O	437	0.78
GNP-N	338	0.73
GNP-H	404	0.76

GNP-P carbon had a BET surface area of 490 m² g⁻¹, however, upon the oxidation a 10.8% surface area loss was observed. When the GNP-O was thermally reduced (GNP-H) or aminated (GNP-N) the surface area decreased further by 7.5% and 22.6%, respectively. The reduction of the surface area for GNP-O can be attributed to limited textural damage during the oxidative treatment ^{[21][26][30]}, while the high temperatures, used during the reduction and amination of the carbon surface (400 °C and 600 °C, respectively), caused a further reduction in surface area^[27]. During the catalytic tests, the current density results were normalized by carbon surface area, while all samples discussed had a similar pore volume were tested (GNP-O, GNP-N and GNP-H).

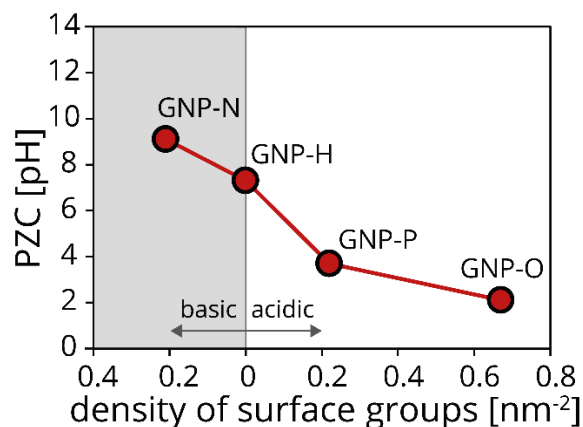


Figure 2.1 - Point of zero charge as a function of the density of surface groups of the GNP-P, GNP-O, GNP-N and GNP-H electrocatalysts.

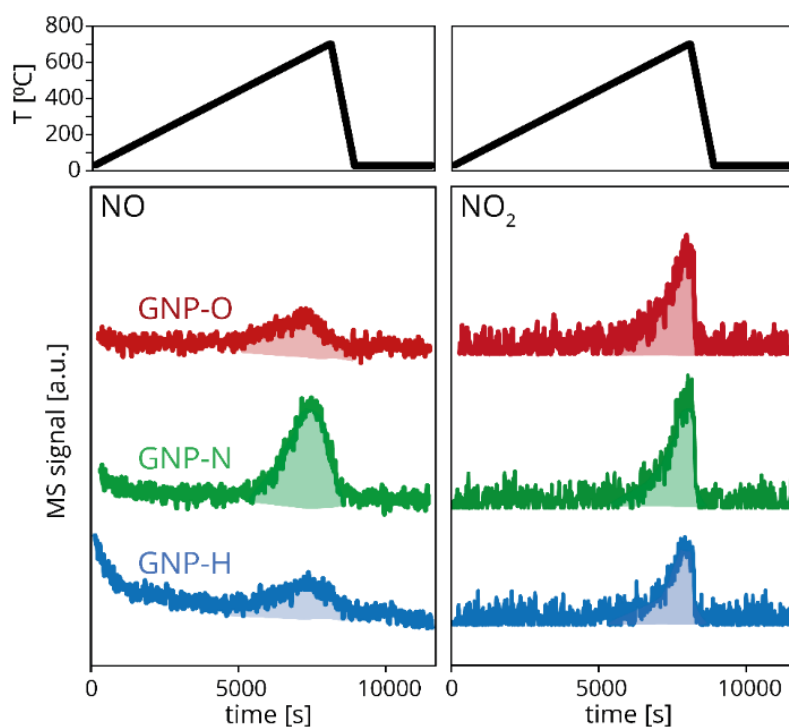


Figure 2.2 - NO (left) and NO₂ (right) MS signals as a function of the elapse time, for the three different surface modified catalysts, obtained during heat treatment in 20% O₂ in Ar using a heating ramp of 5 °C min⁻¹.

The PZC, obtained by acid-base titration, of the surface-modified carbons (figure 2.1) defines the average acid-base properties of the carbon surface and decreased in the following

order: GNP-N > GNP-H > GNP-P > GNP-O. The as-received graphitic carbon (GNP-P) was acidic with a PZC value of 3.7. The acidity of GNP-P originates from native oxygen-containing functional groups^{[22][24][26]}. The GNP-O was more acidic with a PZC value of 2.3 due to the strong acidic groups introduced by the HNO₃ treatment. The surface of GNP-H was neutral with a PZC value of 7.3, possibly due to the disappearance of the acidic groups when heated in a reducing atmosphere^{[25][31]}. The GNP-N was basic with a PZC value of 9.1, resulting from the introduction of basic groups upon amination treatment. The origin of the surface basicity of GNP-N is ascribed to the presence of N-containing groups, as when heated in O₂ atmosphere, nearly two times more NO/NO₂ was released than for GNP-H and GNP-O (figure 2.2)^{[27][32]}. These results show that the PZC of GNP-P surface can be tuned within a broad pH range from 2.3 to 9.1.

The change in PZC correlates with the increase of density of acid or base surface groups, as measured by potentiometric titration. Upon oxidation of the GNP-P, a 3-fold increase in the density of acidic groups was observed, from 0.20 nm⁻² for GNP-P to 0.67 nm⁻² for GNP-O (figure 2.1, x-axis), which explains the low PZC. The GNP-N catalyst had only 0.22 nm⁻² basic surface groups, possibly because of thermal decomposition of the O-containing groups under the harsh conditions (T = 600°C) of the ammonia treatment. GNP-H contained a negligible amount of acid-base surface groups, confirming their removal by the H₂-reduction treatment and therefore leading to a PZC close to 7^[25,26].

Table 2.2 - XPS survey derived atomic percentages of carbon, oxygen and nitrogen in pristine and surface modified carbons.

Sample	C [at%]	O [at%]	N [at%]
GNP-P	96.13	3.73	0.13
GNP-O	90.99	8.82	0.18
GNP-N	96.59	0.63	2.76
GNP-H	95.96	3.69	0.34

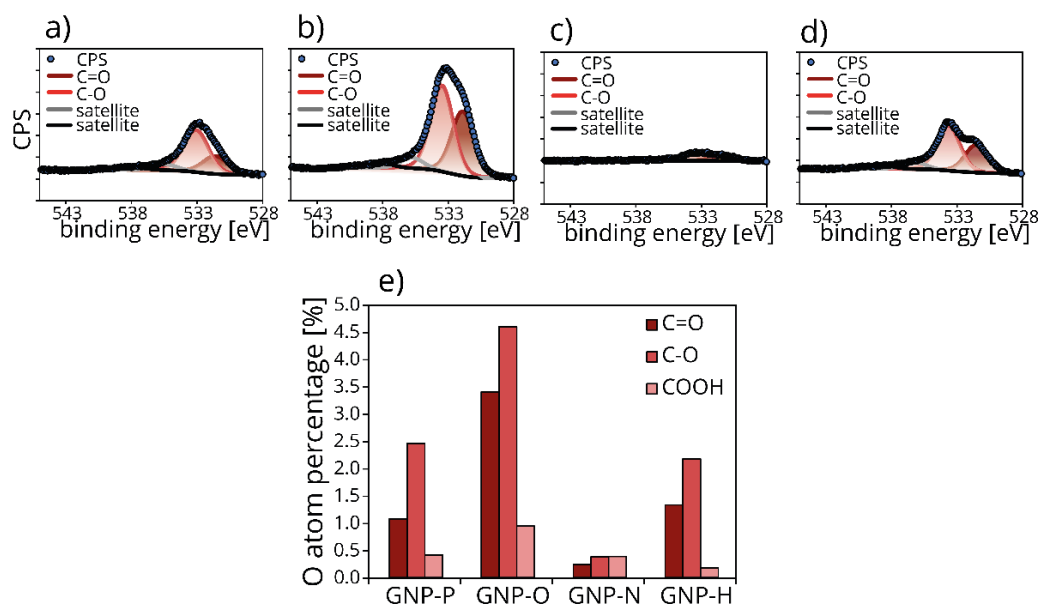


Figure 2.3 - O-containing surface group quantification (e) based on XPS O 1s peak analysis (a-d), where C=O and C-O at% is based on XPS O 1s peak analysis, while COOH at% is based on XPS C 1s peak analysis. a) GNP-P, b) GNP-O, c) GNP-N and d) GNP-H O 1s high resolution XPS spectra.

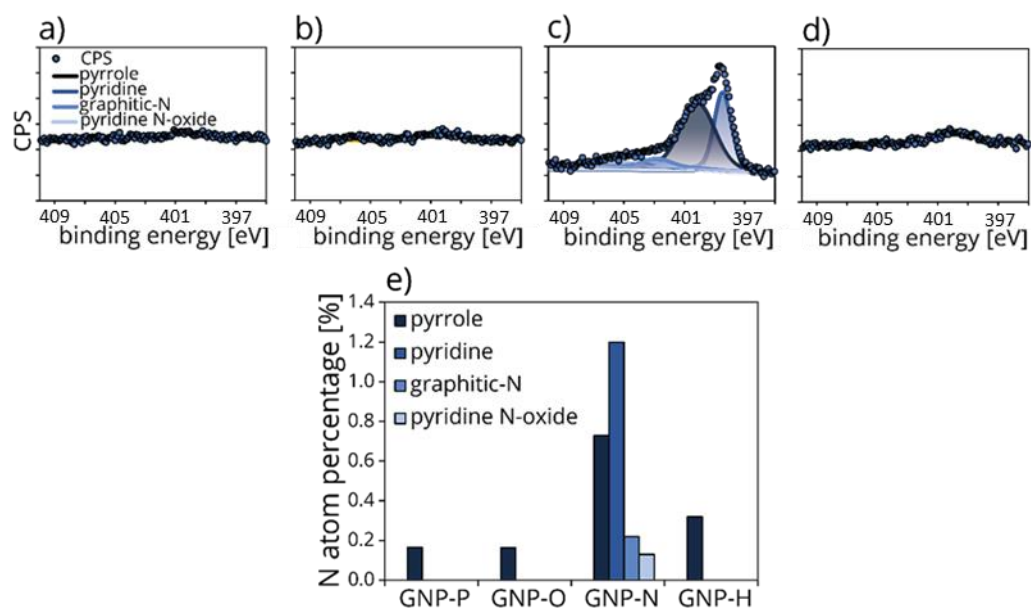


Figure 2.4 - N-containing surface group quantification (e) based on XPS N 1s peak analysis. a) GNP-P, b) GNP-O, c) GNP-N and d) GNP-H N 1s high resolution XPS spectra.

Figure 2.3 and figure 2.4 highlight the surface atomic composition, based on the XPS 1s peaks of C, O and N elements, normalized by their sensitivity factor. The survey spectra showed that C, O and N were indeed the only elements present, as shown in table 2.2. Therefore, the atomic surface compositions calculated can be directly compared to each other. The actual areas used in the calculation were not from the survey but from the high-resolution scans of O (figure 2.3 a-d) and N (figure 2.4 a-d). GNP-O showed a 2-times increase in the O content compared to the pristine material, with 8.7 at% and 4.1 at%, respectively (table 2.2). This confirmed the successful introduction of O-containing groups upon oxidation treatment. The deconvolution of the O 1s peak revealed that GNP-O possessed the largest number of C-O (4.4 at%), C=O (3.5 at%) and COOH (0.8 at%) surface groups (figure 2.3e). Surprisingly, GNP-H presented an oxygen percentage (3.8 at%) similar to the pristine sample, suggesting that the difference in PZC is not directly related to the oxygen content but instead to the different chemical nature of the O-containing groups. GNP-H possessed 2.1 at% C-O and 1.3 at% C=O, while GNP-P showed 2.5 at% C-O and only 1.0 at% C=O. Furthermore, although both catalysts had a small number of COOH groups, with only 0.2 at% for GNP-H and 0.4 at% for GNP-P. Although this difference is small and derived from a fitting model, it might explain the difference observed in PZC. The remarkably low amount of oxygen on GNP-N (0.7 at%) indicates that the ammonia treatment not only introduced N-containing groups, but also induced a thermal decomposition of the O-containing groups. Regarding the N content (figure 2.4e), GNP-H, GNP-O and GNP-P presented a low N content (0.33 at%, 0.12 at% and 0.23 at%, respectively), only composed of pyrrolic groups. The difference in the N content of these catalysts is due to the different specific carbon surface areas as a result of the surface functionalization treatment. On the contrary, GNP-N carbon showed a variety of N-groups, such as pyridinic (1.19 at%), pyrrolic (0.72 at%), graphitic nitrogen (0.21 at%), and pyridine N-oxide (0.12 at%).

Beside the surface groups analysis, the degree of graphitization, which influences the conductivity of the catalysts, was extrapolated from the XPS Auger peak^[33]. All carbon catalysts showed around 77% of sp^2 carbon, demonstrating that the functionalization treatments did not affect the sp^2 character of the samples. To complete the characterization of the modified carbon materials, the X-ray diffraction patterns of the GNP-P, GNP-H, GNP-O and GNP-N catalysts were acquired and shown in the supporting information (figure 2.5). The

diffraction patterns of all surface-modified carbons were similar, meaning that the bulk graphitic structure was not significantly changed by the different surface modification treatments in line with earlier reports^[26]. Representative scanning electron microscopy (SEM) images (figure 2.6) of the freshly prepared electrodes show a uniform coverage of the carbon paper substrate with the modified carbon catalysts. The elemental analysis results showed only C, O and F, where the F came from the Nafion binder used to anchor the catalyst to the carbon paper. Furthermore, both EDX (table 2.3) and XPS (table 2.2) did not show any metal impurity. They were also not expected in these samples, as the initial oxidation treatment was performed for all the catalysts in a highly concentrated nitric acid solution.

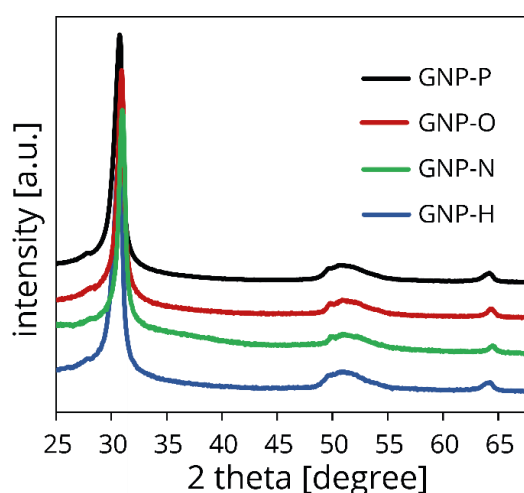


Figure 2.5 - X-rays diffraction patterns of GNP-P, GNP-H, GNP-O and GNP-N

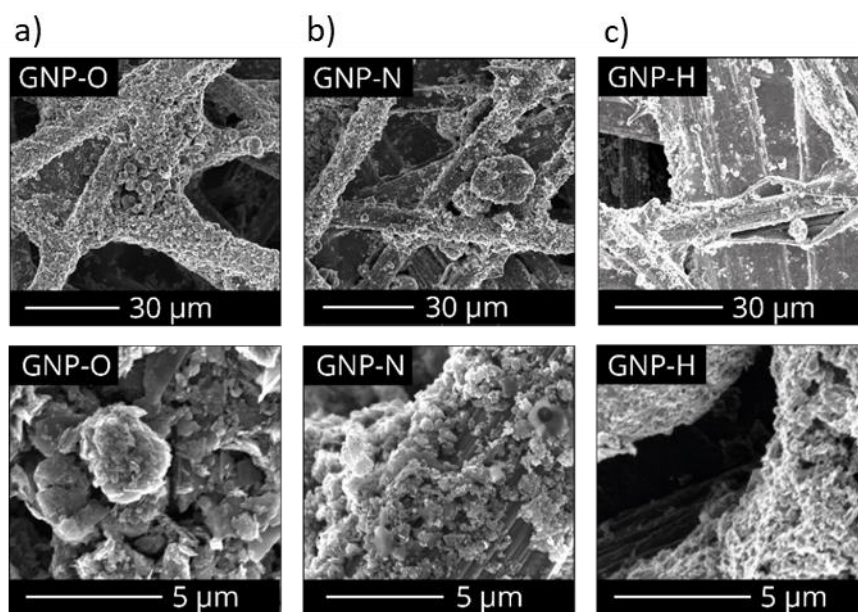


Figure 2.6 - Representative SEM images of the surface-modified carbons a) GNP-O, b) GNP-N and c) GNP-H deposited on the carbon paper substrate. Low magnification for an overview (top) and high magnification for a more detailed view (bottom).

Table 2.3 - EDX weight percentages of the pristine and surface modified carbons after deposition onto carbon paper.

Sample	C [wt%]	O [wt%]	F [wt%]
GNP-O	26.9	71.6	1.5
GNP-N	26.6	70.9	2.4
GNP-H	26.5	70.8	2.6

2.3.2 Electrocatalytic reduction of CO₂

Figure 2.7 shows the total current density (j_{total}), normalized by the carbon surface area, as a function of the applied negative potential for GNP-H, GNP-O and GNP-N in a CO₂-saturated 0.1 M KHCO₃ aqueous solution at pH 6.8. The current density was obtained at four different potentials (-0.7, -0.9, -1.2 and -1.4 V vs RHE), averaging over 45 min. At -1.2 V vs RHE, GNP-H

showed a current density of -20.1 mA m^{-2} , while GNP-O and GNP-N exhibited slightly larger current densities: -25.2 mA cm^{-2} and -28.2 mA cm^{-2} respectively. The different current densities can be explained by the difference in the catalytic activity of acid/base surface groups of which the GNP-O and GNP-N electrodes have a higher density than the GNP-H catalyst^{[34][35][36]}.

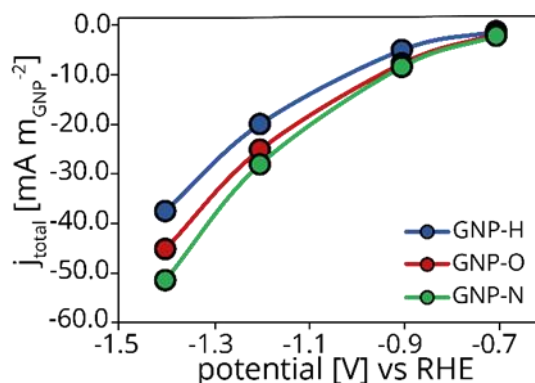


Figure 2.7 - Total current density, as a function of the applied potential of GNP-H, GNP-O and GNP-N electrocatalyst in a CO_2 -saturated 0.1 M KHCO_3 electrolyte at pH 6.8.

To understand the influence of surface functionalization on the selectivity, we evaluated the CO and H_2 partial current densities, normalized to the carbon surface area. Figure 2.8a shows the hydrogen current densities as a function of the applied negative potential. The GNP-H catalyst gave the lowest current density with -18.9 mA m^{-2} at -1.2 V , while GNP-O and GNP-N produced a slightly larger H_2 current (-24.6 mA m^{-2} at -1.2 V vs RHE). This small current increase might be explained by an improved wetting of the carbon due to the presence of polar surface groups on GNP-O and GNP-N.

Figure 2.8b shows the CO partial current densities of the modified catalysts. GNP-N is the only catalyst that shows a non-negligible CO current at only -0.9 V vs RHE. At -1.4 V vs RHE, GNP-N exhibits by far the largest CO current density, about 5.5-times higher than to the oxidized carbon and the reduced carbon. Furthermore, GNP-O produced formic acid, with a FE of 5.8% at only -0.7 V vs RHE. The catalysts produced formic acid only at more cathodic potentials. As the precision in the quantification of formic acid *via* HPLC is limited^{[3][8][16][20][37][38][39]}, we will mainly focused in the reminder of the paper, on understanding the selectivity towards CO.

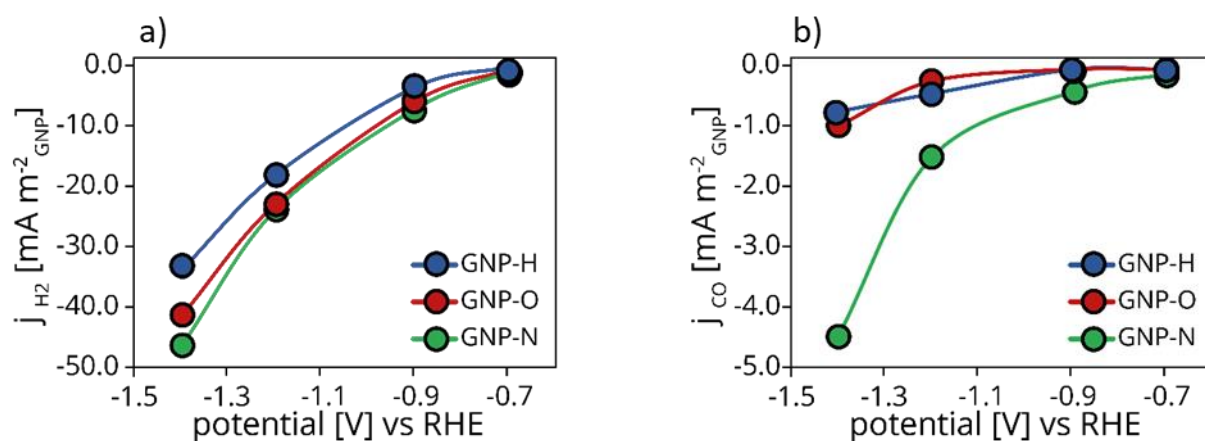


Figure 2.8 - a) H₂ and b) CO partial current density normalized by carbon surface area, as a function of the applied potential of the GNP-H, GNP-O and GNP-N catalyst in a CO₂-saturated 0.1 M KHCO₃ electrolyte at pH 6.8.

In figure 2.9, the CO Faraday efficiency (FE) for all the surface-modified carbons is shown as a function of the applied potential. At -0.7 V and -0.9 V vs RHE, GNP-H and GNP-O did not produce any CO. However, GNP-N produced 3.5% and 4.3% CO FE respectively, demonstrating that the CO₂ reduction began at lower overpotential. Upon increasing the potential to -1.2 V and -1.4 V vs RHE, the GNP-N electrocatalysts clearly produced most CO, with a FE of 5.1% and 8.6% respectively at these potentials.

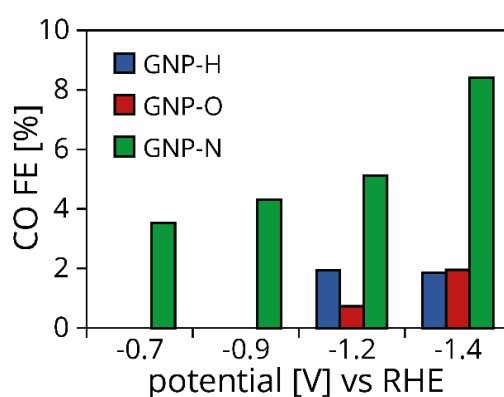


Figure 2.9 - CO faradaic efficiency as a function of the applied potential, for the GNP-H, GNP-O and GNP-N catalyst in a CO₂-saturated 0.1 M KHCO₃ electrolyte at pH 6.8.

2.3.3 Effect of the surface functional groups on the CO selectivity

To quantify the effect of different surface groups on the CO production, we calculated the CO turnover frequency (TOF) (figure 2.10). This analysis assumes that the carbon surface (alone) is involved in H₂ evolution, while the functional surface groups are responsible for the CO evolution. The GNP-H catalyst was excluded from the analysis due to the uncertain nature of the active sites. Although the hydrogen treatment is meant to remove all surface groups, the process is likely to have also introduced other type of defect sites, but the nature of these defect is not yet well understood. Therefore, we attribute the activity of the GNP-H to the presence of such defects and/or to presence of low concentrations of the pyrrolic N groups (0.4 at%), after the hydrogen treatment.

At low overpotentials, the CO TOF of GNP-O (red marker) was negligible. In contrast, the TOF of GNP-N electrocatalyst (green marker) was 0.001 and 0.005 mol_{CO} s⁻¹ mol_{groups}⁻¹ respectively. At -1.2 V and -1.4 V vs RHE, the N-containing groups showed a 15-20-fold higher intrinsic activity than the O-containing groups present on GNP-O catalyst. These results demonstrated that the structure and chemical properties of carbon surface groups plays a key role on the selective reduction of CO₂. By treating the carbon electrocatalysts, we modified their acidity/basicity. CO₂ is a weak Lewis acid^[40], and hence preferentially adsorbed and further converted on strong Lewis basic active sites. The XPS measurements (figure 2.4) showed strong Lewis basic groups (pyridinic) on the surface of GNP-N (PZC = 9.1), which can explain its high CO partial current density. The lone electron pair on the pyridinic N atom can bind to the electrophilic C in CO₂, leading to *COOH formation, the first intermediate of the proton-coupled electron transfer pathway to CO^{[41][15]}.

Although recent results from DFT calculations suggest that pyrrolic groups can contribute to CO formation at very high overpotentials, this has not been supported by experiments. Experimental results indicate that the pyridinic groups mostly determine the CO partial current density^[18]. We hence only normalized the CO TOF to the pyridinic groups (figure 2.10, empty markers, being aware that this is an approximation.

Under this assumption, the intrinsic TOF of these groups is 0.12 mol_{CO} s⁻¹ mol_{pyridine} at -1.4 V vs RHE. Most of the published work on carbon-based electrocatalysts for CO₂ reduction involves materials produced *via* a bottom-up approaches, such as chemical-vapor deposition, using organic precursor such as pyridine, acetonitrile and dimthylformamide^[42], to achieve a

high N content (in the carbon framework) and carefully designed graphene sheets. Hence, the selectivity and current density reported in literature is much higher, up to 80-85% CO FE and 100 mA cm^{-2} [29][39][43]. Interestingly, our work showed for the first time that simple surface functionalization procedure, starting from commercially available carbon powder, exhibits similar effects to a doping process. Furthermore, the combination of these simple procedures and a detailed surface characterization allowed to quantify the specific contribution of pyridinic groups to the CO TOF of GNP-N, giving a remarkable insight on the selectivity of these groups. Although the specific CO TOF for carbon surface groups is not found in literature for this reaction, similar values were reported for more complex organometallic systems, such as carbon nanotubes functionalized with iron porphyrin (0.049 s^{-1})^[44], and nickel cyclam catalysts (0.015 s^{-1})^[45], tested in similar conditions.

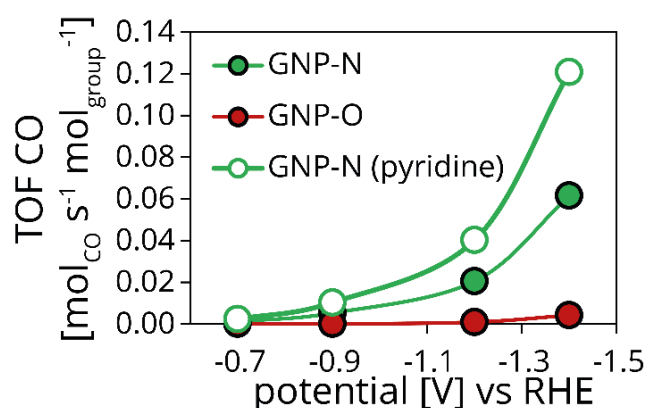


Figure 2.10 - Turn over frequency (TOF) CO molar production per unit of time per mol surface group as a function of the applied potential. TOF was obtained through a combination of the CO partial current density and surface group analysis for GNP-N and GNP-O electrocatalyst. All the measurements were obtained in CO₂-saturated 0.1 M KHCO₃ 6.8 pH electrolyte.

2.4 Conclusions

In this chapter, a systematic study of the effect of surface-modification of graphitic carbon on its properties as electrode for the CO₂RR has been performed. Two different treatments introduced N-containing or O-containing surface groups, leading to basic or very acid surface properties. An alternative treatment removed surface groups, leading to a near neutral surface. The total current density, and the product selectivity of the CO₂ reduction were influenced by the nature and density of the surface groups. Especially the pyridinic groups showed a high intrinsic activity to form CO, while acidic groups rather led to formic acid production. Overall, the hydrogen evolution reaction on the carbon was still dominating, but our approach presented here showed for the first time that the selectivity can be rationally tuned by altering the surface chemistry *via* simple surface functionalization. By evaluating the CO turn over frequencies, it was found that nitrogen containing groups showed 20-times higher intrinsic selectivity compared to the oxygen containing groups.

Acknowledgements

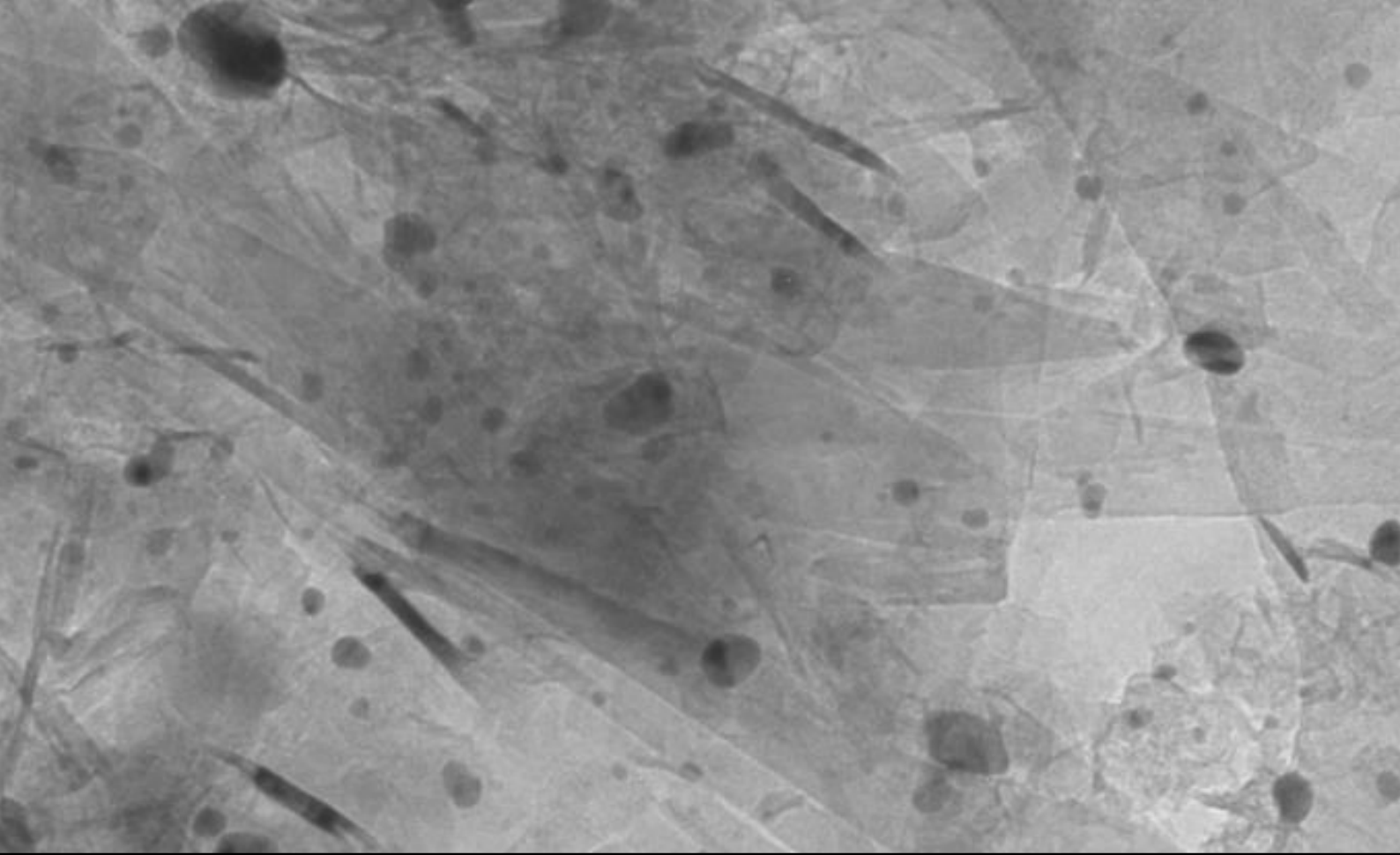
Marisol Tapia Rosales was supported by the NWO-ElReCet project, part of the Solar-to-Products program funded by the Dutch Research Council (NWO). Jan Willem de Rijk is acknowledged for useful discussions on the electrochemical set-up. Iris ten Have is acknowledged for the SEM images.

References

- [1] S. Siahrostami, K. Jiang, M. Karamad, K. Chan, H. Wang, J. Nørskov, *ACS Sustain. Chem. Eng.* **2017**, 5, 11080–11085.
- [2] Y. Sun, Q. Wu, G. Shi, *Energy Environ. Sci.* **2011**, 4, 1113–1132.
- [3] M. Pumera, *Energy Environ. Sci.* **2011**, 4, 668–674.
- [4] D. A. C. Brownson, D. K. Kampouris, C. E. Banks, *J. Power Sources* **2011**, 196, 4873–4885.
- [5] L. Dai, D. W. Chang, J.-B. Baek, W. Lu, *Small* **2012**, 8, 1130–1166.
- [6] H. Wang, X. Yuan, G. Zeng, Y. Wu, Y. Liu, Q. Jiang, S. Gu, *Adv. Colloid Interface Sci.* **2015**, 221, 41–59.
- [7] N. Yang, S. R. Waldvogel, X. Jiang, *ACS Appl. Mater. Interfaces* **2016**, 8, 28357–28371.
- [8] Z. Sun, T. Ma, H. Tao, Q. Fan, B. Han, *Chem* **2017**, 3, 560–587.
- [9] G. P. Hao, W. C. Li, D. Qian, G. H. Wang, W. P. Zhang, T. Zhang, A. Q. Wang, F. Schüth, H. J. Bongard, A. H. Lu, *J. Am. Chem. Soc.* **2011**, 133, 11378–11388.
- [10] P. Atkins, J. de Paula, *Physical Chemistry*, W. H. Freeman, New York, **2006**.
- [11] X. Sun, *Front. Chem.* **2021**, 9, 1–9.
- [12] A. S. Varela, W. Ju, A. Bagger, P. Franco, J. Rossmeisl, P. Strasser, *ACS Catal.* **2019**, 9, 7270–7284.
- [13] F. Pan, B. Li, W. Deng, Z. Du, Y. Gang, G. Wang, Y. Li, *Appl. Catal. B Environ.* **2019**, 252, 240–249.
- [14] X. Hao, X. An, A. M. Patil, P. Wang, X. Ma, X. Du, X. Hao, A. Abudula, G. Guan, *ACS Appl. Mater. Interfaces* **2021**, 13, 3738–3747.
- [15] M. Abdinejad, E. Irtem, A. Farzi, M. Sassenburg, S. Subramanian, H. P. Iglesias Van Montfort, D. Ripepi, M. Li, J. Middelkoop, A. Seifitokaldani, T. Burdyny, *ACS Catal.* **2022**, 12, 7862–7876.
- [16] J. Wu, S. Ma, J. Sun, J. I. Gold, C. Tiwary, B. Kim, L. Zhu, N. Chopra, I. N. Odeh, R. Vajtai, A. Z. Yu, R. Luo, J. Lou, G. Ding, P. J. A. Kenis, P. M. Ajayan, *Nat. Commun.* **2016**, 7, 1–6.
- [17] A. H. and G. S. Ruguang Ma, Kuikui Wang, Chunjie Li, Chundong Wang, *Nanoscale Adv.* **2022**, 814–823.

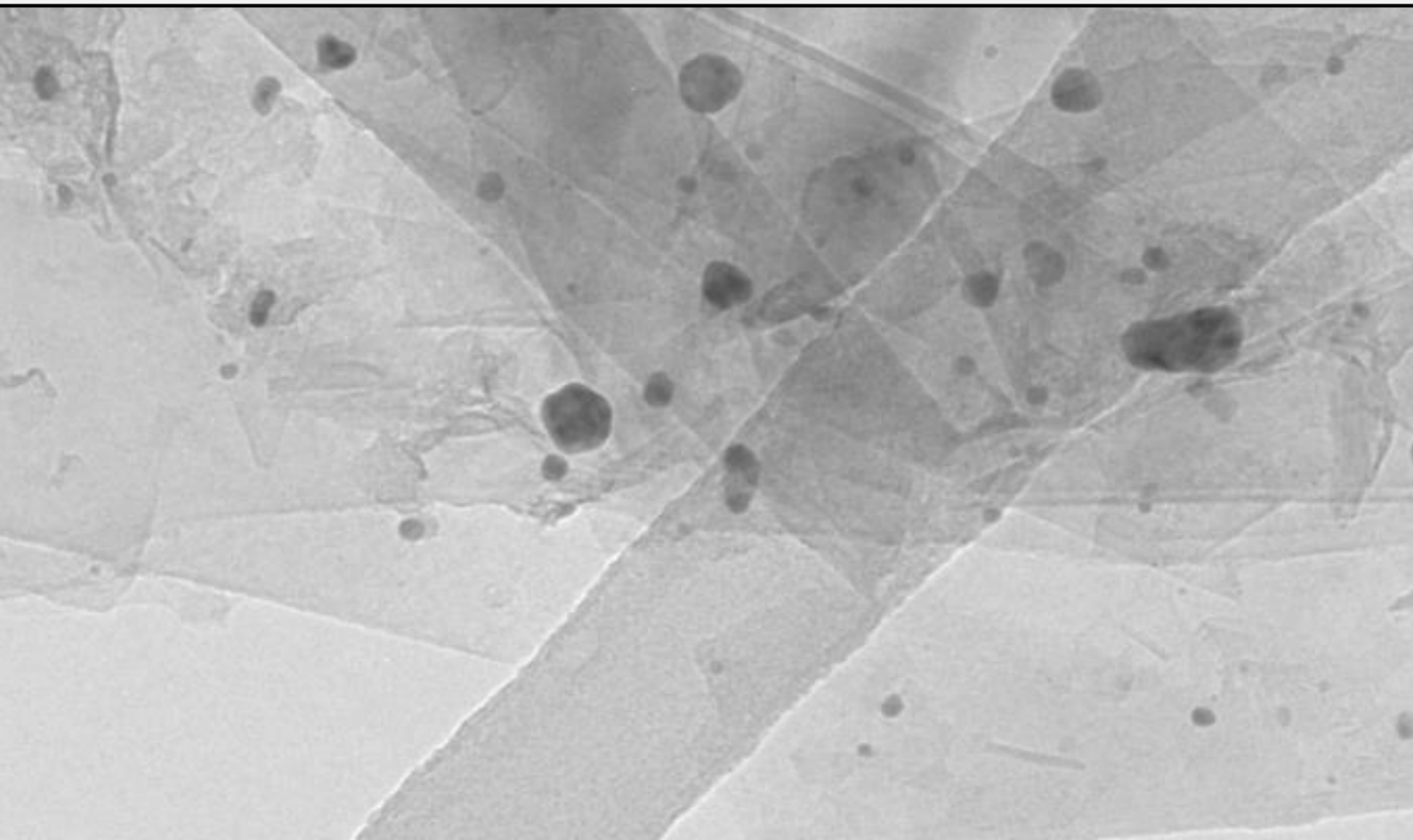
- [18] J. Yuan, W. Y. Zhi, L. Liu, M. P. Yang, H. Wang, J. X. Lu, *Electrochim. Acta* **2018**, *282*, 694–701.
- [19] S. Liu, H. Yang, X. Huang, L. Liu, W. Cai, J. Gao, X. Li, T. Zhang, Y. Huang, B. Liu, *Adv. Funct. Mater.* **2018**, *28*, 1800499.
- [20] F. Yang, X. Ma, W. Cai, P. Song, W. Xu, *J. Am. Chem. Soc.* **2019**, *51*, 20451–20459.
- [21] R. Beerthuis, J. W. de Rijk, J. M. S. Deeley, G. J. Sunley, K. P. de Jong, P. E. de Jongh, *J. Catal.* **2020**, *388*, 30–37.
- [22] H. P. Boehm, *Carbon N. Y.* **1994**, *32*, 759–769.
- [23] B. M. Philippe Serp, in *Nanostructured Carbon Mater. Catal.*, **2015**, 20–33.
- [24] J. L. Figueiredo, *J. Mater. Chem. A* **2013**, *1*, 9351–9364.
- [25] B. Donoeva, N. Masoud, P. E. De Jongh, *ACS Catal.* **2017**, *7*, 4581–4591.
- [26] D. Sebastián, I. Suelves, R. Moliner, M. J. Lázaro, *Carbon N. Y.* **2010**, *48*, 4421–4431.
- [27] R. Arrigo, M. Hävecker, S. Wrabetz, R. Blume, M. Lerch, J. McGregor, E. P. J. Parrott, J. A. Zeitler, L. F. Gladden, A. Knop-Gericke, R. Schlögl, D. S. Su, *J. Am. Chem. Soc.* **2010**, *132*, 9616–9630.
- [28] M. G. Plaza, S. García, F. Rubiera, J. J. Pis, C. Pevida, *Sep. Purif. Technol.* **2011**, *80*, 96–104.
- [29] L. Chen, P. Peng, L. Lin, T. C. K. Yang, C. Huang, *Aerosol Air Qual. Res.* **2014**, *14*, 916–927.
- [30] M. P. van Heeswijk, J. H. Bitter, M. L. Toebe, A. J. van Dillen, K. P. de Jong, *Carbon N. Y.* **2004**, *42*, 307–315.
- [31] J. L. Figueiredo, M. F. R. Pereira, *J. Energy Chem.* **2013**, *22*, 195–201.
- [32] M. A. Montes-Morán, D. Suárez, J. A. Menéndez, E. Fuente, *Carbon N. Y.* **2004**, *42*, 1219–1225.
- [33] D. J. Morgan, *C* **2021**, *7*, 51.
- [34] B. Buczek, S. Biniak, A. Świątkowski, *Fuel* **1999**, *78*, 1443–1448.
- [35] S. Mrozowski, *Carbon N. Y.* **1971**, *9*, 97–109.
- [36] K. H. Radeke, K. O. Backhaus, A. Swiatkowski, *Carbon N. Y.* **1991**, *29*, 122–123.
- [37] J. Wu, M. Liu, P. P. Sharma, R. M. Yadav, L. Ma, Y. Yang, X. Zou, X. Zhou, R. Vajtai, B. I. Yakobson, J. Lou, P. M. Ajayan, *Nano Lett.* **2016**, *16*, 466–470.
- [38] J. Wu, R. M. Yadav, M. Liu, P. P. Sharma, C. S. Tiwary, L. Ma, X. Zou, X. D. Zhou, B. I.

- Yakobson, J. Lou, P. M. Ajayan, *ACS Nano* **2015**, *9*, 5364–5371.
- [39] H. Wang, Y. Chen, X. Hou, C. Ma, T. Tan, *Green Chem.* **2016**, *18*, 3250–3256.
- [40] H. Kiuchi, R. Shibuya, T. Kondo, J. Nakamura, H. Niwa, J. Miyawaki, M. Kawai, M. Oshima, Y. Harada, *Nanoscale Res. Lett.* **2016**, *11*, 0–6.
- [41] Y. Yan, E. L. Zeitler, J. Gu, Y. Hu, A. B. Bocarsly, *J. Am. Chem. Soc.* **2013**, *135*, 14020–14023.
- [42] P. P. Sharma, J. Wu, R. M. Yadav, M. Liu, C. J. Wright, C. S. Tiwary, B. I. Yakobson, J. Lou, P. M. Ajayan, X. D. Zhou, *Angew. Chemie - Int. Ed.* **2015**, *54*, 13701–13705.
- [43] G. L. Chai, Z. X. Guo, *Chem. Sci.* **2016**, *7*, 1268–1275.
- [44] A. Maurin, M. Robert, *Chem. Commun.* **2016**, *52*, 12084–12087.
- [45] F. Greenwell, G. Neri, V. Piercy, A. J. Cowan, *Electrochim. Acta* **2021**, *392*, 139015.



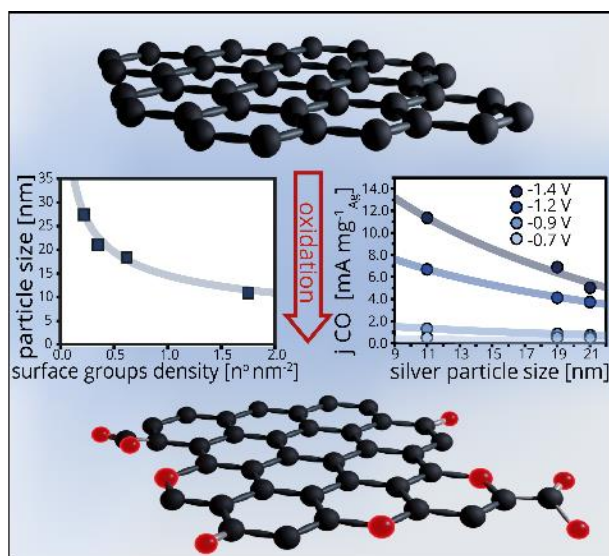
CHAPTER 3

Ligand-free silver nanoparticles



Abstract

The use of supported nanoparticles for electrocatalysis is appealing as it enables high dispersion of catalysts and control over the nanoparticle sizes, which influence catalytic activity. In this chapter, we report a strategy to synthesize highly dispersed, ligand-free silver Ag nanoparticles supported on carbon. We demonstrate that the heat treatment atmosphere and carbon surface chemistry are crucial to control the Ag particle size in the 10-30 nm range. Even at low silver loadings ($0.099 \text{ m}^2_{\text{Ag}} \text{ m}^{-2}$), Ag nanoparticles outperform the bulk silver at low overpotentials, leading to a 23.5% CO Faradaic efficiency at -1.2 V vs RHE. The Ag weight-based activity of the catalysts scaled with the inverse particle size, while the Ag surface-specific activity was independent of particle size in this range. The supported silver nanoparticles can produce a H_2 to CO ratio of 2.9 to 1, interesting for further exploration of this type of catalysts for syngas synthesis.



This chapter is based on the article:

Francesco Mattarozzi, Nienke Visser, Jan Willem de Rijk, Peter Ngene and Petra de Jongh, 'Ligand-free silver nanoparticles for CO_2 electrocatalytic reduction to CO', *European Journal of Inorganic Chemistry*, **2022**, e202200365.

3.1 Introduction

In his pioneering work, Hori demonstrated that silver is one of the most promising transition metals for CO₂ reduction, thanks to the high selectivity towards CO, a valuable chemical building block, compared to zinc and other transition metals^{[1][2][3]}. Supporting silver nanoparticles on conductive substrates can maximize the activity of the costly metal^{[4][5][6]}. Control over the particle size is essential to study the relationship between the structural properties of the catalyst and the electrochemical performance. In literature, colloidal synthesis of silver nanoparticles is often reported, as it can give good control over the nanoparticle size and morphology^{[7][8][9][10][11][12]}. However, the presence of ligands, which are difficult to remove, hampers studies of the intrinsic catalytic properties of silver nanoparticles. However, the synthesis of ligand-free silver particles is challenging^[13]. To increase the stability of the metal catalyst, silver nanoparticles are often supported on high surface area materials. Despite the high selectivity towards hydrogen formation, carbon offers many advantages as support material for the silver nanoparticles for fundamental studies, such as good electrical conductivity, and the possibility to tune the silver particle size and the carbon support properties, which can influence the catalytic performance^{[14][15][16]}. Unfortunately, often a high metal weight loading and high mobility of silver species on carbon supports lead to sintering of the nanoparticles at moderate temperatures, leading to large particle size and broad particles distribution^{[17][18]}.

In this chapter, we discuss a novel approach to control the particle size of ligand-free silver nanoparticles supported on carbon by Incipient Wetness Impregnation (IWI). We investigated the effect of different decomposition atmospheres and densities of carbon surface groups. We achieved reasonable control over the particle size, and we correlated specific electrochemical parameters (the CO Faradaic efficiency, CO partial current density and the H₂ to CO ratio) to the silver particle size and surface coverage.

3.2 Experimental section

3.2.1 Modification of the carbon materials

To study the influence of the support functional groups on the silver particle size, the commercial carbon powders GNP500 (XGnP500 purchased from XG Science) and HSAG100 (TIMREX) were functionalized using nitric acid (Sigma Aldrich, 65.0% wt/wt)^[19]. Specifically, the carbon substrate (10 g) was dispersed in concentrated HNO₃ (50 mL_{HNO3} g_{carbon}⁻¹) in a 1 L round bottom flask equipped with a cooler. To avoid NO_x leaks during the procedure, two slightly basic (pH=8) water traps were connected to the head of the cooler. The reaction mixture was heated to 80 °C for 2 hours under vigorous stirring. Subsequently, the reaction mixture was quenched with cold water. The modified carbon was thoroughly washed with deionized water until the solution reached neutral pH, and then dried overnight at 90 °C in a round bottom flask. The effect of the functionalization procedure was evaluated by point of zero charge (PZC) analysis, potentiometric titration, N₂ physisorption and X-ray powder diffraction (XRD). The graphitic carbon supports were labelled with a number indicating the BET surface area of the pristine support and a letter, referring to the pristine (P) or oxidized (O).

3.2.2 Synthesis of supported silver nanoparticles

The silver nanoparticle were deposited by incipient wetness impregnation^[20]. The carbon support was dried under vacuum at 170 °C for 2 hours, to remove moisture and air from the pores. Subsequently, the support was impregnated with an AgNO₃ (Sigma Aldrich, 99.0%) aqueous solution under static vacuum at room temperature. The volume of the solution corresponded to 95% of the support pore volume and the AgNO₃ concentration varied between 2 M and 6 M, in order to achieve a silver weight loading of 10% for all the catalysts. After the impregnation step, the catalyst was dried under dynamic vacuum at room temperature for 10 hours, to remove the water and leave AgNO₃ nanocrystals on the surface of the carbon support. The dried catalyst was transferred to a fixed bed reactor (internal diameter 1 cm) and placed in the oven under a flow (6000 mL g⁻¹ h⁻¹) of 10% H₂ in N₂. The reactor was heated to 300 °C with a ramp of 5 °C min⁻¹, to decompose the AgNO₃ to Ag⁰. We

refer to the Ag catalysts using an Agx@y-z nomination, where x is the mean particle size of the sample (i.e., Ag11, Ag19 and Ag21), y is the pristine support surface area and z is either P (pristine support) or O (oxidized support). For instance, Ag11@100-O refers to a catalyst with 11 nm Ag nanoparticles, supported on the oxidized (O) graphitic carbon support with 100 m² g⁻¹ surface area (100).

3.2.3 Working electrode preparation

The working electrodes were prepared by spraying the supported silver catalysts (Ag21@100-P, Ag19@500-O and Ag11@100-O) on a carbon paper electrode (Toray TGP-H-060). The catalyst (11 mg) was dispersed in a 4470 μ L Milli-Q water, 1120 μ L isopropanol (Sigma Aldrich, 99.5%) and 44.4 μ L Nafion solution (Sigma Aldrich, 5.0% in a mixture of aliphatic alcohols and water) and sonicated for 45 minutes. This ink was then sprayed onto the carbon paper (Toray, TGP-H-060, 4.9 cm²) and dried overnight at room temperature^[21]. A catalyst loading of 0.1 mg_{Ag} cm⁻² was intended for all the catalysts. A uniform distribution of the catalyst over the carbon paper support was demonstrated by SEM analysis (figure 3.1).

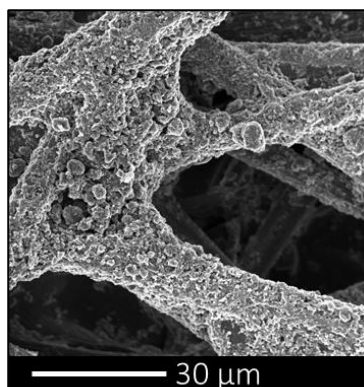


Figure 3.1 – SEM image of the carbon paper substrate (supporting fibers) with graphitic carbon nanoplatelets (500-O) uniformly covering the substrate after spraying.

3.2.4 Characterization

The BET surface area and the pore volume of the carbon support were probed *via* N₂-physisorption performed with a Micromeritics TriStar instrument at -196 °C. The carbon

powder was dried at 170°C under vacuum. Transmission electron microscopy (TEM) images of Ag19@500-O were acquired using Thermo Fischer Scientific Tecnai20 microscope, operated at 200 kV, while the TEM images of the other samples were acquired using TalosL120C microscope, operated at 120 kV. The holey carbon 200 mesh copper grids were prepared by drop casting a mixture of ethanol and supported Ag catalysts, previously sonicated for 45 minutes. The Ag nanoparticle size was determined by measuring 300 particles at 5 different locations. The average particle size was calculated as number average particle size using equation 3.1:

$$\text{average particle size} = \frac{\sum_i^n d_n}{N} \quad \text{equation 3.1}$$

where d_n is the diameter of particle n , and N is the total number of particles counted. To calculate the total silver surface area from the particle size distribution measured with TEM images, with b_n being the central value of each bin, and the particle count c_n corresponding to the number of particles in the n^{st} bin. The Ag metal surface area SA_{pn} (equation 3.2) and volume V_{pn} (equation 3.3) of a single particle in bin n were calculated assuming hemispherical nanoparticles:

$$SA_{pn} = 2 * \pi * \left(\frac{b_n}{2}\right)^2 \quad \text{equation 3.2}$$

$$V_{pn} = \frac{2}{3} * \pi * \left(\frac{b_n}{2}\right)^3 \quad \text{equation 3.3}$$

Furthermore, the mass of a single particle (M_{pn}) in bin n was calculated using the Ag bulk density ρ (equation 3.4):

$$M_{pn} = \rho * V_{pn} \quad \text{equation 3.4}$$

By multiplying the particle count c_n by the mass of a single particle in the bin, the total silver mass in each bin (M_{bn}) was obtained using equation 3.5:

$$M_{bn} = c_n * M_{pn} \quad \text{equation 3.5}$$

Then, we calculated the specific surface area of the single bin n , as the sum of the surface areas of the particles in bin n per total silver mass on the sample (equation 3.6):

$$SSA_{bn} = (c_n * SA_{pn}) / \sum_1^n M_{bn} \quad \text{equation 3.6}$$

The SSA_{bn} represents the silver surface area (nm^2) for the specific bin n per total weight of silver on the sample ($g_{Ag \text{ tot}}$). The last step to calculate the total silver surface area is to sum all SSA_{bn} , multiplied by the real silver weight loading on the electrode and by the electrode surface area (equation 3.7):

$$\begin{aligned} \text{total silver SA} &= \sum_1^n SSA_{bn} * Ag \text{ weight loading} * \text{electrode SA} = \\ &= \left(\frac{nm_{Ag}^2}{g_{Ag \text{ tot}}} \right) * \left(\frac{g_{Ag \text{ tot}}}{cm_{electrode}^2} \right) * (cm_{electrode}^2) \end{aligned} \quad \text{equation 3.7}$$

To calculate the silver surface coverage and the silver surface fraction, the Ag density ($10.49 \text{ g}_{Ag} \text{ cm}_{Ag}^{-3}$) was used, which leads to a total silver volume of $0.01 \text{ cm}^3 \text{ g}_{carbon}^{-1}$. It is considered the case study of Ag11@100-O. A hemispherical nanoparticle morphology with an average particle size of 11 nm was assumed. Therefore, the volume of a single Ag particle (V_{1P}) is calculated *via* equation 3.8:

$$V_{1P} = \frac{4}{6} * \pi * r^3 = 348.27 \text{ nm}^3 \text{ particle}^{-1} \quad \text{equation 3.8}$$

The total number of particles per gram of carbon support is the calculated by dividing the total Ag volume by the volume of a single particle (equation 3.9):

$$\frac{0.01 \text{ cm}^3}{3.48 * 10^{-19} \text{ cm}^3} = 3.04 * 10^{16} \text{ particles } g_{carbon}^{-1} \quad \text{equation 3.9}$$

From the BET analysis, we could use the specific surface area of the support ($55 \text{ m}^2 \text{ g}^{-1}$) and the surface area covered by a single Ag particle ($94.5 \text{ nm}_{Ag}^2 \text{ particle}^{-1}$, considering the area of a circle) to calculate the number of Ag nanoparticles per m^2 of carbon ($5.52 * 10^{14} \text{ particles m}^{-2}$).

$\text{m}^2_{\text{carbon}}$) and therefore, the Ag area that covers the carbon support ($5.25 \times 10^{16} \text{ nm}^2_{\text{Ag}} \text{ m}^{-2}_{\text{carbon}}$), corresponding to 5.25% of carbon surface covered by silver nanoparticles.

Furthermore, we can calculate the total Ag exposed surface area (hemisphere) per unit of area of high surface area carbon support (equation 3.10):

$$SA_{\text{Ag}} = 2 * \pi * r^2 * \text{particles} \text{ m}^{-2}_{\text{carbon}} = 0.1 \text{ m}^2_{\text{Ag}} \text{ m}^{-2}_{\text{carbon}} \quad \text{equation 3.10}$$

The last step was to calculate the total Ag surface area exposed at the working electrode ($0.005 \text{ m}^2_{\text{Ag}} \text{ cm}^{-2}_{\text{electrode}}$) and high surface area carbon support exposed at the working electrode ($0.046 \text{ m}^2_{\text{carbon}} \text{ cm}^{-2}_{\text{electrode}}$), and then evaluate the fraction of silver at the surface of the electrode (equation 3.11):

$$\begin{aligned} \text{Ag fractional surface coverage} &= \frac{0.005 \text{ m}^2_{\text{Ag}} \text{ cm}^{-2}_{\text{electrode}}}{0.046 \text{ m}^2_{\text{carbon}} \text{ cm}^{-2}_{\text{electrode}} + 0.005 \text{ m}^2_{\text{Ag}} \text{ cm}^{-2}_{\text{electrode}}} \\ &= 0.099 \end{aligned} \quad \text{equation 3.11}$$

The same calculations were applied to all the different catalysts.

X-ray diffraction (XRD) measurements were performed on a Bruker D2 Phaser, equipped with a Co K_{α} X-ray source with a wavelength of 1.79026 \AA . The PZC of the support was measured by titration, using Milli-Q water as a solvent. This method involves the gradual addition of carbon material to 3 mL Milli-Q solution and continuous measurement of the pH. The pH of the solution saturates at high carbon concentrations, with the pH approaching the PZC of the support. The density of functional surface groups was evaluated by potentiometric titration using the TitraLab TIM880 Titration Manager apparatus. In particular, 20 mg of the sample was dispersed in 35 mL 0.1 M KCl solution and 0.01 M NaOH was used as the titrant.

3.2.5 Electrochemical measurements

A custom-built, three-electrode H-type electrochemical cell was used for the electrocatalytic experiments (figure 3.2). The cathodic compartment (volume = 11 mL) was separated from the anodic compartment (volume = 11 mL) by a Nafion membrane (Ion Power,

Nafion N117). The CO₂ saturated catholyte was purged with 10 mL min⁻¹ CO₂ (Linde, purity 5.2), while the anolyte was stirred by bubbling Ar. The working electrode was composed of a glassy carbon disc (HTW-Germany), in contact with the external electrical circuit and a carbon paper disc that was impregnated with the catalyst. The carbon paper surface area exposed to the electrolyte was 3.8 cm². We used a Ag/AgCl (Metrohm, 3 M KCl) reference electrode and a 3.8 cm² Pt disc (Metrohm, 99.5%) as counter electrode. A 0.5 M KHCO₃ (Sigma Aldrich, >99.0%) solution (pH = 7) was used as electrolyte. All the electrochemical measurements were performed using an Autolab PGSTAT204 potentiostat, and the applied potential was converted to the reversible hydrogen electrode potential (RHE) using equation 3.12:

$$E_{\text{RHE}} = E_{\text{Ag/AgCl}} + 0.209 + 0.059 \text{ pH} \quad \text{equation 3.12}$$

The electrocatalytic performance was determined by chronoamperometry measurements at different potentials for 45 minutes. The gaseous products were analysed by connecting the cathodic compartment outlet to a Global Analysis Solutions Microcompact GC 4.0. The GC instrument was equipped with three channels. The first channel, a Rt-QBond (10 m x 0.32 mm, Agilent) packed column, detects CH₄, C₂H₄ and C₂H₆, using a FID detector; the second channel, Molecular Sieve 5A (10 m x 0.53 mm, Restek) packed column, that separates small gaseous molecules such as CO, and CH₄, is equipped with a methanizer, in order to increase the sensitivity for CO detection; the third channel, with a TCD detector, has a Carboxen 1010 (8m x 0.32 mm, Agilent) packed column which separates H₂ and CO₂. High purity nitrogen (99.9%) was used as a carrier gas. The liquid products were analysed using a Varian HPLC with a refractive index detector (RID) and a Bio-Rad Aminex HPX-87H column at 60 °C. The Ag disc (Goodfellow, 99.9%, temper: as rolled), used as benchmark, was mechanically polished using an alumina slurry before the electrochemical test.

The total current density analysis is crucial to compare the rate of the electron transfer across the electrode-solution interface, for different catalysts. We defined the total current density as the average current recorded at a specific potential, normalized by the geometrical surface area of the electrode (3.8 cm²). The Faradaic efficiency was calculated using equation 3.13:

$$FE = \frac{(n * F * mol)}{i_{tot} * t} \quad \text{equation 3.13}$$

where n were the moles of electrons per mole of product ($\text{mol}_P \text{ mol}_e^{-1}$), F represents the Faraday constant (C mol_e^{-1}), mol are the moles of products formed (mol_P), i is the total current (C s^{-1}) and t is the analysis time (s). Since the total Faradaic efficiency is very close to 100% for all catalysts, we preferred to normalize the value by 100, to fairly compare the samples. The partial current density defines the contribution of the individual reaction products to the total current density. This parameter was calculated as the product of the total current density and the FE.

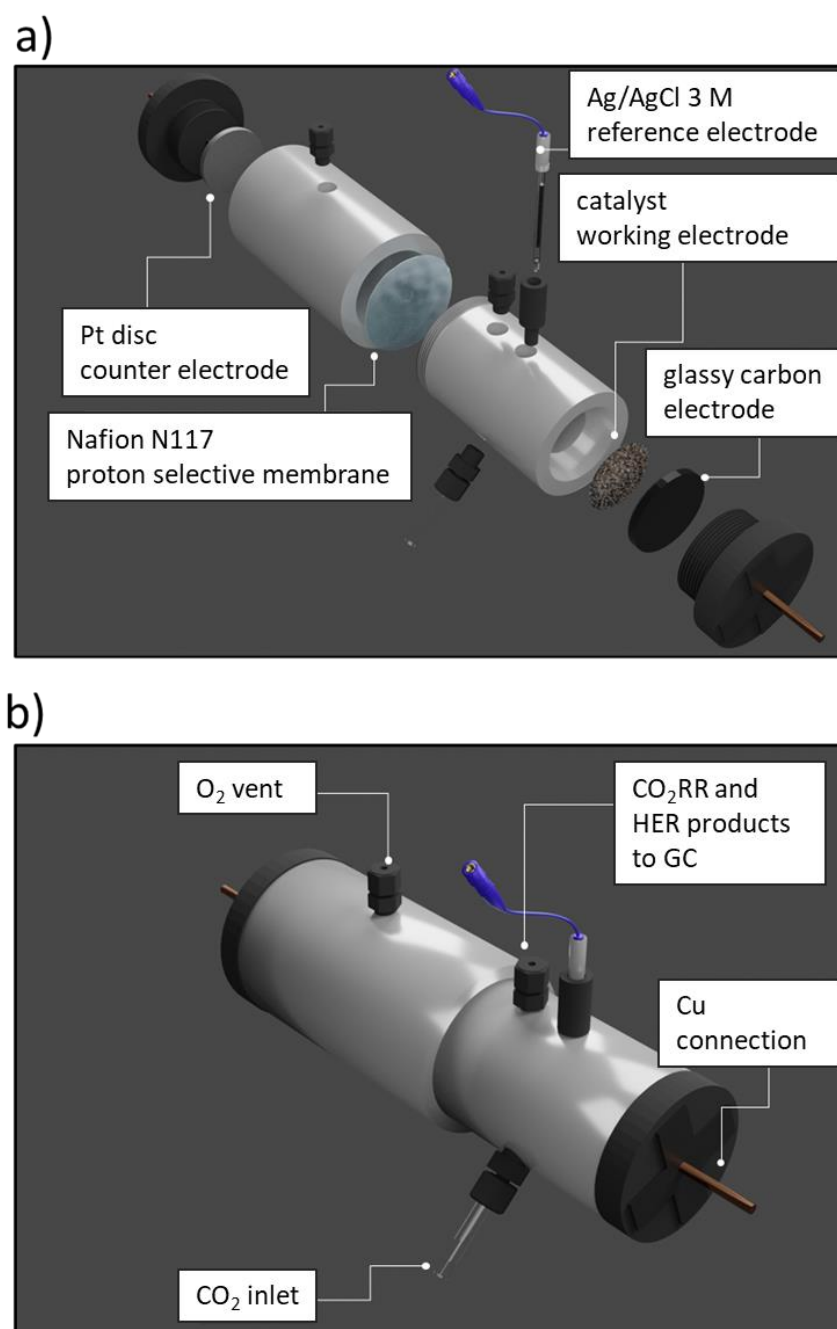


Figure 3.2 – Schematic representation of the custom-built electrochemical cell designed by Marisol Tapia Rosales, Sneh Sameer and Manfred van den Berg. a) Open electrochemical cell and b) close electrochemical cell.

3.3 Results and discussion

3.3.1 Control over the particle size

The first parameter, that can be used to tune the silver particle size, is the composition of the atmosphere during the silver nitrate decomposition. We compared two samples: the first was treated in an inert atmosphere (pure nitrogen, electron micrograph in figure 3.3a) while the second was exposed to a reducing atmosphere (10% H₂ in nitrogen, electron micrograph in figure 3.3b). All other variables, such as the silver loading on 100-P commercial carbon (10% wt/wt), the heat treatment temperature (250°C) and gas hourly space velocity (6000 mL g_{cat}⁻¹ h⁻¹), were the same for both samples. Figure 3.3c and 3.3d show the corresponding particle size distributions. In reducing atmosphere silver nanoparticles of 21 ± 15 nm were formed, while the treatment in inert atmosphere produced 34 ± 30 nm particles. This effect can be explained by the direct decomposition of AgNO₃ precursor to form Ag under H₂, while silver oxide intermediates are formed in inert atmosphere. Oxidized silver species are known to be highly mobile on the surface of the support, which can explain the larger particles and broad particle size distribution. Other reducing atmospheres with different gas composition (i.e. 30% H₂ in N₂) have been tested, but no beneficial effects were observed, rather larger particles and broad particle size distribution. This is likely related to the fast kinetics of the decomposition reaction to form Ag nanoparticles on the carbon surface. Hence, 10% H₂/N₂ was used for all the samples.

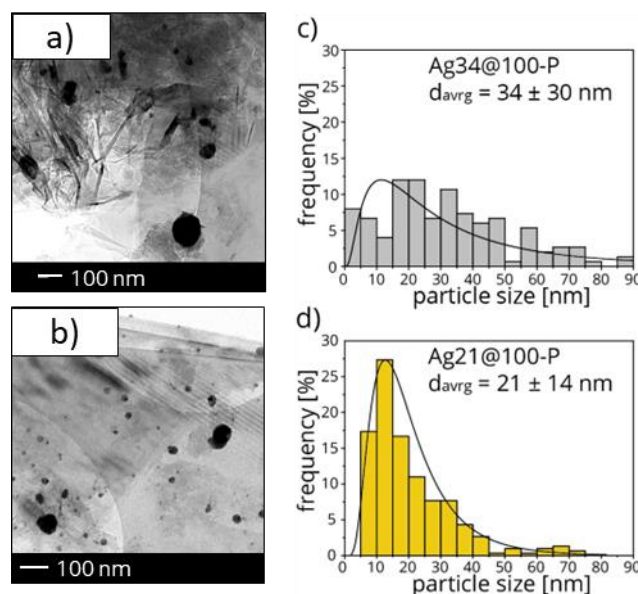


Figure 3.3 – On the left, TEM images of a) Ag34@100-P and b) Ag21@100-P. On the right, particle size distribution of c) Ag34@100-P and d) Ag21@100-P.

After establishing the most promising gas composition to control the particle size, we further investigated the tunability of the particle size by using the same gas composition during the heat treatment (10% H₂ in N₂) but varying the surface properties of the carbon support. We compared the size of silver nanoparticles supported on four carbon materials, with different densities of acidic surface groups and surface areas (table 3.1).

Table 3.1 – BET surface areas, pore volumes, PZC and number of acid groups for the pristine (GC100-P and GC500-P) and the functionalized supports (GC100-O and GC500-O).

Carbon support ID	BET [m ² g ⁻¹]	Pore volume [cm ³ g ⁻¹]	PZC [pH]	Number of acidic groups [n° nm ⁻²]	Number of acidic groups [n° g ⁻¹]
100-P	92	0.21	3.9	0.35	3.2
100-O	55	0.12	2.9	1.75	9.8
500-P	496	0.95	4	0.22	10.9
500-O	451	0.82	3.1	0.71	32.1

The commercial GNP500 support (in this chapter, 500-P) has a 5-fold larger surface area than HSAG100 (100-P) pristine carbon. As in chapter 2, upon acidic functionalization, the

surface areas of both carbon supports decreased by $40 \text{ m}^2 \text{ g}^{-1}$, although the XRD patterns showed that crystallinity of the carbon materials was not significantly affected. Interestingly, after functionalization, both 100-O and 500-O showed a 3-fold increase in the concentration of acid groups (table 3.1). With 1.75 groups per nm^2 , 100-O showed a higher density of surface groups per unit of surface than 500-O with only 0.71 groups per nm^2 .

Figure 3.4 (a–d) shows the TEM images of the Ag nanoparticles on the different supports and the corresponding particle size distribution (figure 3.4 e–h). By comparing the images of the nanoparticles supported on the pristine (100-P and 500-P) and functionalized (100-O and 500-O) carbons, it is clear that a high number of surface groups led to small nanoparticles and a narrower size distribution. Ag11@100-O presented an average particle size of $11 \pm 8 \text{ nm}$, while Ag21@100-P showed a particle size of $21 \pm 15 \text{ nm}$. Ag19@500-O showed a smaller particle size (19 nm) and less broad particle size distribution (13 nm) than the catalyst based on the pristine carbon (Ag28@500-P). In figure 3.5, we related the particle size to the density of acid groups per unit of surface area. This correlation suggests that the surface groups act as nucleation and/or anchoring sites for the silver nanoparticles during the impregnation step. Since the pH of the precursor solution (6.0) was higher than the PZC of the support (table 3.1), it is likely that the silver cations interacted electrostatically with the deprotonated acid groups at the carbon support. Therefore, a higher number of surface groups per nm^2 might lead to a higher number of Ag nuclei, and, consequently, to a smaller Ag nanoparticle size.

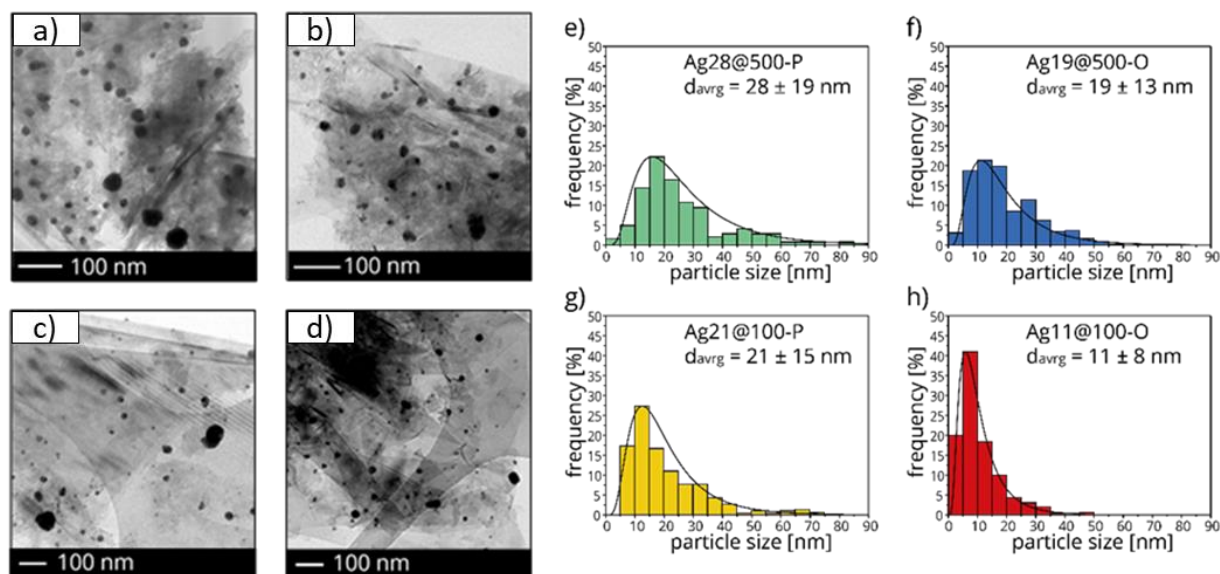


Figure 3.4 – On the left, TEM images of a) Ag28@500-P, b) Ag19@500-O, c) Ag21@100-P and d) Ag11@100-O. On the right, the corresponding particle size distributions of e) Ag28@500-P, f) Ag19@500-O, g) Ag21@100-P and h) Ag11@100-O.

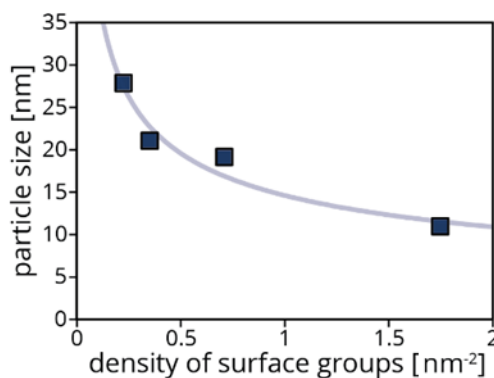


Figure 3.5 – Ag particle size as a function of the density of functional groups on the surface of the carbon support. The blue line is added to guide the eye.

3.3.2 Electrocatalytic activity

As more than 90% of our catalyst' exposed surface consisted of carbon, and carbon is known to be active to form H_2 , we first studied the electrochemical activity of the supports. Figure 3.6a show the total current densities of different carbon electrodes as a function of the applied potential, measured using chronoamperometry. The oxidized supports (i.e., 500-O and 100-O) produced a similar current density, with a maximum of -6.29 mA cm^{-2} at -1.4 V vs RHE, while the pristine support (100-P) generated a slightly smaller current density, with -5.70 mA cm^{-2} at the same potential. This observation can be explained by considering the surface properties of the carbons after the oxidation procedure. The high number of surface groups on 100-O and 500-O are expected to facilitate the electron transfer at the electrode-electrolyte interface.

Next, we consider the carbon supported Ag nanoparticles. Note that the effect of the oxidation state of silver nanoparticles is not discussed in this work. Although no silver oxide diffraction peaks were detected in the XRD analyses (figure 3.7a) nor silver oxide reduction peaks during the cycle voltammetry scans of the supported catalysts (figure 3.7b), we cannot exclude the presence of silver oxide at the surface, as the catalysts were exposed to the atmosphere. Nevertheless, the oxidation layer will affect all the catalysts in similar way, hence the obtained results do not strictly depend on it. Figure 3.6b shows the total current densities for the supported silver nanoparticles, measured using chronoamperometry at different applied potentials. No significant differences were observed between the electrodes. Furthermore, by overlaying figure 3.6a and figure 3.6b, it is evident that the deposition of silver nanoparticles did not significantly change the electrochemical current compared to the bare supports. This result is perhaps not unexpected, given the low silver surface coverage, equal to 5% (Ag11@100-O) of the total carbon area. Therefore, we conclude that the current of the carbon-supported silver catalysts is dominated by the high surface area carbon support. However, by comparing our catalysts with the benchmark, we found that all the silver on carbon electrodes drew larger currents than the pure Ag foil. The smaller current density produced by the bulk flat electrode is likely due to its low electrochemical surface area (3.8 cm^2). To unravel the effect of the silver nanoparticles on CO_2 reduction, we consider two crucial parameters: the CO Faradaic efficiency and the CO partial current density.

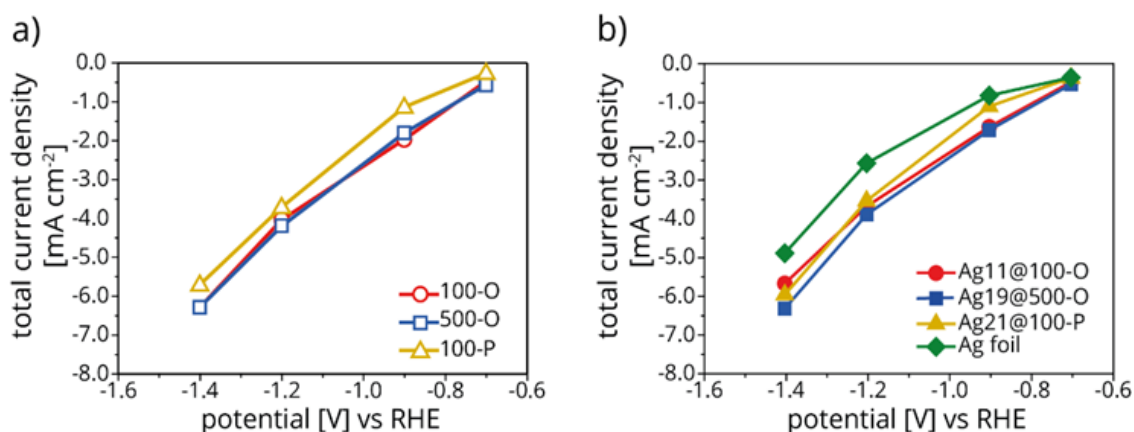


Figure 3.6 – a) Total current density for the bare carbon supports 100-P, 100-O and 500-O as a function of the applied potential. b) Total current density for the supported silver catalysts Ag21@100-P, Ag11@100-O, Ag21@500-O and pure silver foil, as a function of the applied potential. In this figure, the current density is normalized to the geometric surface area of the electrode.

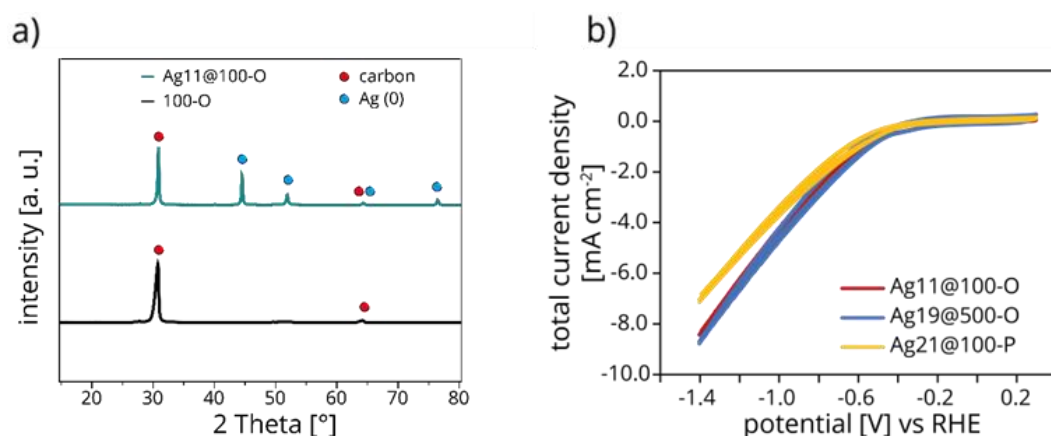


Figure 3.7 – a) XRD pattern of 100-O carbon (black line) and Ag11@100-O (cyan line). b) Cyclic voltammetry measurements performed at 10 mV s⁻¹ scan rate, showing the comparison between the three different catalysts. All the curves shown are the result of the overlapping of three CV cycles from more anodic to more cathodic potentials.

3.3.3 Effect of the silver coverage on the CO Faradaic efficiency

CO is the only product of CO₂ electroreduction expected for Ag catalysts, as no formate nor other liquid products was detected in the electrolyte, while H₂ evolution over carbon is the competitive reaction^{[22][23]}. Figure 3.8 shows the Faradaic efficiency (FE) towards CO, which is the fraction of electrons transferred contributing to the formation of CO, as a function of the silver surface fractional coverage, calculated as the m² of silver divided by the total catalyst surface, assuming hemispherical particles and using the average number particle size determined by TEM. The missing faradaic efficiency, up to 100%, is attributed to hydrogen. We chose the silver surface coverage as a key parameter to analyze the FE, since both silver and carbon contributed to the CO₂ electroreduction processes. The bare carbon 100-O (0.00 Ag fraction) produced mostly H₂ and only a small amount of CO. On the contrary, Ag11@100-O (0.099 Ag fraction) gave a 25.6% CO FE at -1.4 V vs RHE. Although the HER dominates the FE, due to the high carbon surface area exposed to the electrolyte, a remarkably low concentration of silver nanoparticles and a low Ag surface fraction can significantly steer the selectivity of the electron transfer at the electrode surface towards CO₂ reduction. The evaluation of the selectivity at a given Ag fraction showed an increase of the CO FE with more negative potential. At constant potential, the CO FE increases as the Ag fraction increases. For instance, Ag11@100-O showed a 10.4% CO FE at very low overpotentials (-0.9 V vs RHE), while Ag21@100-P (0.032 Ag fraction) and Ag19@500-O (0.007 Ag fraction) produced only 8.4% and 6.5% CO FE at the same potential. The bulk silver electrode (1.00 Ag fraction, at the right side of figure 3.8) showed a low CO FE at low overpotentials, with 6.0% CO FE at -0.9 V, even lower than Ag21@500-O. For higher overpotentials, the Faradaic efficiency to CO at the pure Ag foil electrode was similar to that of the supported Ag nanoparticles (5.0% surface coverage on carbon)^{[24][25]}. Although catalytic data for intermediate silver surface fraction are missing, this analysis confirms the selective electron transfer *via* supported silver nanoparticles. A logical approach to increase the CO FE would be to increase the silver weight loading. Unfortunately, by increasing weight loading, we observed an uncontrolled particle growth, leading to a large particle size and broad particle size distribution (figure 3.9), hence the effects of the particle size cannot be reliably investigated.

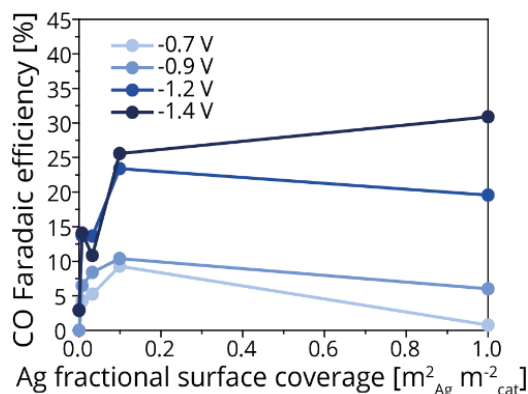


Figure 3.8 – CO Faradaic efficiency comparison as a function of the Ag fractional coverage at the surface of the catalyst. Pure carbon = 0 m²_{Ag} m⁻²; Ag19@500-O = 0.007 m²_{Ag} m⁻²; Ag21@100-P = 0.032 m²_{Ag} m⁻²; Ag11@100-O = 0.099 m²_{Ag} m⁻²; bulk Ag electrode = 1 m²_{Ag} m⁻². The blue lines are added to guide the eye.

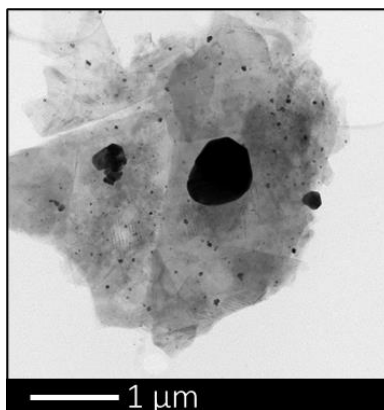


Figure 3.9 – TEM images of Ag@100-O 20% wt/wt, after heat treatment in 10% H₂.

3.3.4 Effect of the particle size on the CO partial current density

Figure 3.10 shows the CO partial current density as a function of the applied potential for both the carbon materials (figure 3.10a) and the carbon supported silver nanoparticles (figure 3.10b). As expected, the bare supports presented very low CO partial current densities, confirming that carbon support is highly selective towards the formation of H₂. Nevertheless, it seems that acidic surface groups slightly promote the CO₂ reduction, since 500-O produced a 1.6-fold and 10-fold higher CO partial current than 100-O and 100-P, respectively.

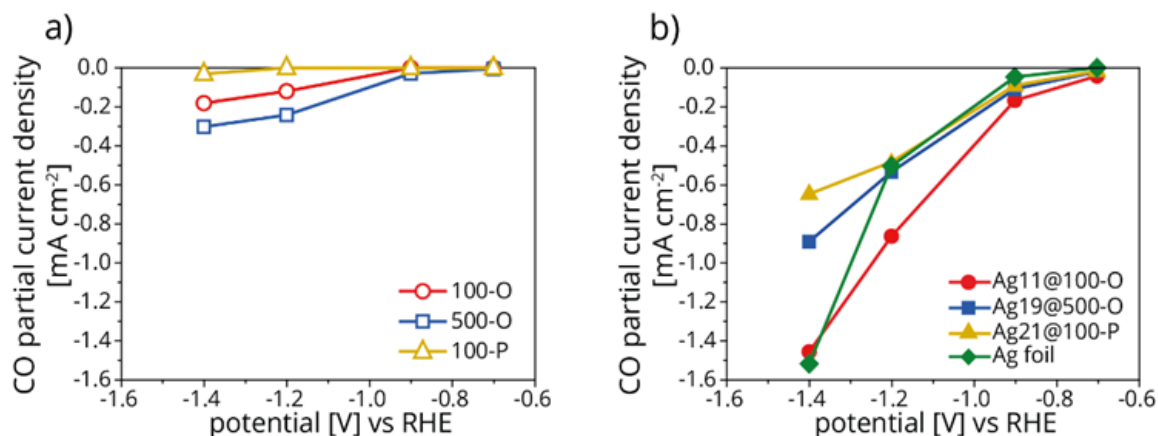


Figure 3.10 – a) CO partial current density comparison for the bare carbon supports (empty markers) as a function of the applied potential. b) CO partial current density comparison for Ag supported catalysts (full markers), as a function of the applied potential. In this figure, the current density was normalized to the geometric surface area of the electrode.

Figure 3.10b shows the CO current densities, normalized to the geometric surface area of the electrode of supported silver nanoparticles and the pure silver foil. The absolute values of the CO current density increased for all catalysts with the overpotentials. This increase became close to linear at large negative potentials, suggesting resistance-limited behavior, probably due to diffusion limitations in the electrolyte solution. Additionally, we observed that Ag11@100-O, the catalysts with the smallest particle size, outperformed the other catalysts, generating a 1.6- and 2.2-times higher CO current density than Ag19@500-O and Ag21@100-P at -1.4 V vs RHE, respectively. Notably, Ag11@100-O gives a larger cathodic CO current density compared to the pure silver foil at low overpotentials. This might be explained by low-coordinated active sites at the surface of the silver nanoparticles readily stabilizing the CO intermediates, leading to an 0.4 mA cm⁻² larger cathodic current than the silver foil, at -1.2 V vs RHE. In conclusion, the trend in CO current density demonstrates that the addition of silver nanoparticles to the carbon support, even at low weight loadings (10⁻⁴ g_{Ag} cm⁻²), increased remarkably the selectivity towards CO, while the high surface area carbon defines the total current density of the catalysts.

To understand the influence of Ag particle size, we analyzed the CO partial current density as a function of the average particle size (figure 3.11). Figure 3.11a shows the absolute

value of CO partial current density, normalized by the silver weight, measured at different potentials. It is clear that over the whole potential range, the CO partial current density is inversely proportional to the particle size. Furthermore, the particle size effect was enhanced at larger overpotentials. Ag11@100-O produced $6.7 \text{ mA mg}_{\text{Ag}}^{-1}$, while Ag19@500-O and Ag21@100-P generated only $4.1 \text{ mA mg}_{\text{Ag}}^{-1}$ and $3.7 \text{ mA mg}_{\text{Ag}}^{-1}$, respectively. This implies that either the smaller particles were intrinsically more active, or that it was simply an effect of specific surface area. Figure 3.11b shows the CO current density normalized to the silver surface area, calculated considering the particle size distribution obtained by TEM images. This analysis reveals that the specific current density does not greatly depend on the particle size, and a weak trend is only observed at high overpotentials. Hence, there is no intrinsic difference between Ag11@100-O and other catalysts. The difference in CO FE when only the geometric surface areas are considered, is mainly due to the higher dispersion of the Ag on the carbon. Therefore, the remarkable catalytic performance (i.e. CO current density, CO FE) of Ag11@100-O is due to a higher surface to volume ratio for the smaller Ag nanoparticles.

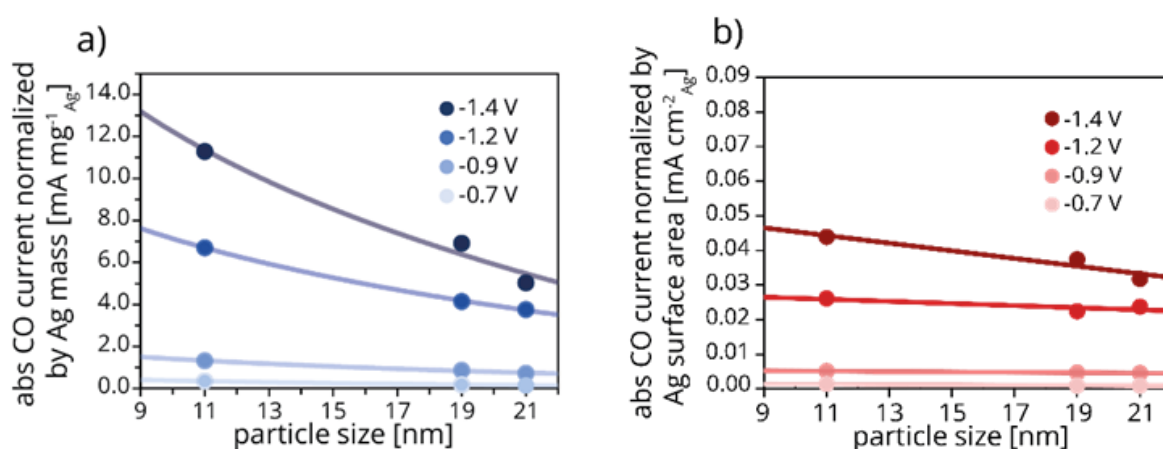


Figure 3.11 – a) CO partial current density normalized by Ag weight on the electrode, as a function of the particle size. b) CO partial current density normalized by Ag surface area, as a function of the particle size. The interpolation lines are used to help understand the figure.

3.3.5 H₂ to CO ratio

Since the electrochemical production of syngas, a mixture of hydrogen and carbon monoxide, might represent an opportunity to use ‘green’ hydrogen and CO to produce sustainable fuels, we evaluated the H₂ to CO ratio for the different catalysts. Figure 3.12 shows the H₂ to CO ratio as a function of the total current density. Ag11@100-O produced the lowest H₂ to CO ratio, compared to Ag19@500-O and Ag21@100-P, at all currents. For all the catalysts, the H₂ to CO ratio decreased at larger current densities, considering, for instance, that Ag11@100-O generated a minimum H₂ to CO ratio of 2.9 at the largest current density (-5.9 mA cm⁻²). This behavior is probably due to the effect of the local pH on the reaction selectivity. Large current densities, generated at more cathodic potentials, result in proton consumption at the electrode-electrolyte interface. This phenomenon increases the local pH and steers the selectivity towards CO₂ reduction products by suppressing the H₂ evolution^[26]. Ag11@100-O gave a 3 to 1 H₂ to CO ratio at -1.2 V vs RHE, a ratio that is close to be suitable to produce linear-chain alkanes *via* Fischer-Tropsch reaction. On the contrary, Ag19@500-O and Ag21@100-P exhibited an H₂ to CO ratio of only 6 to 1 at the same potential. This finding demonstrates that by tuning the particle size and the support surface properties, we can control the H₂ to CO ratio even at high current densities. Having said that, it has to be borne in mind that the current densities in these experiments are still much lower than required for industrial application.

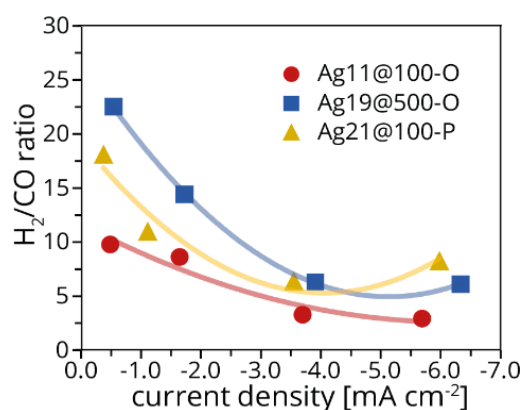


Figure 3.12 – H₂ to CO ratio for the different catalysts, as a function of the total current density.

3.4 Conclusions

In this chapter, we have synthesized ligand-free silver nanoparticles supported on high surface area carbon materials *via* incipient wetness impregnation, achieving control over the particle size. Based on the knowledge about carbon modifications described in chapter 2, we demonstrated the importance of the atmosphere during the heat treatment and the density of acidic surface groups to gain control over the particle size in the range of 11 nm to 21 nm. The total current density of the catalysts, during the CO₂ reduction in 0.1 M KHCO₃, was dominated by the high surface area of the carbon support producing H₂. Nevertheless, the presence of only 0.1 mg_{Ag} cm⁻² of silver on the carbon paper electrode effectively steered the selectivity to 25% CO at -1.4 V vs RHE. Small nanoparticles of 11 nm produced higher CO currents than a bulk silver electrode. The mass activity of the catalysts decreased with increasing particle size, while the specific surface activity showed no dependence on the particle size. Hence, the remarkable catalytic performance of the small silver nanoparticles was achieved thanks to a good dispersion of the silver nanoparticles. The H₂ to CO ratio was as low as 2.9 : 1 at -5.9 mA cm⁻².

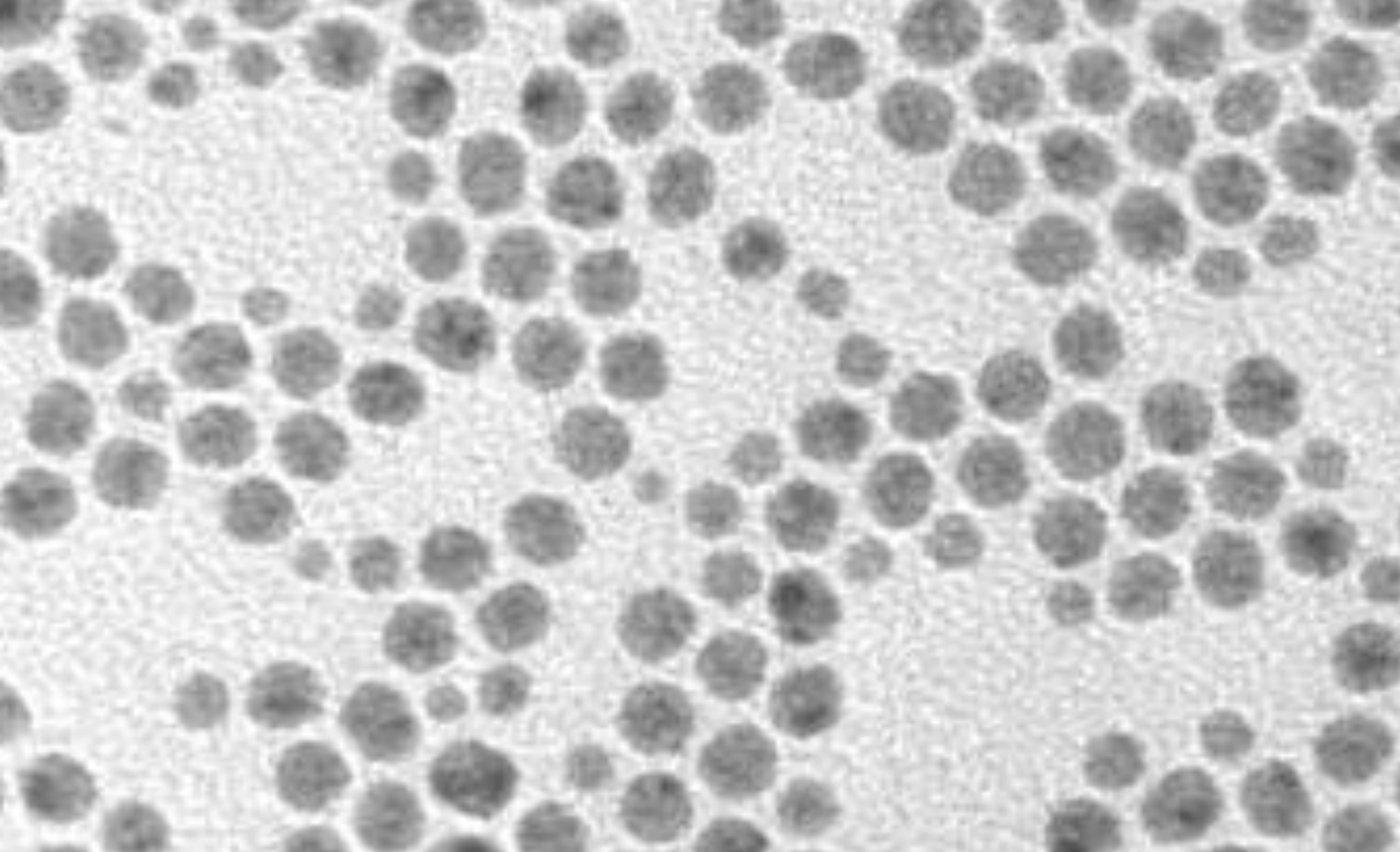
Acknowledgements

Kai Han is acknowledged for useful discussions regarding electrochemical measurements. Marisol Tapia Rosales, Sneha Sameer and Manfred van den Berg are acknowledged for the design of the electrochemical cell.

References

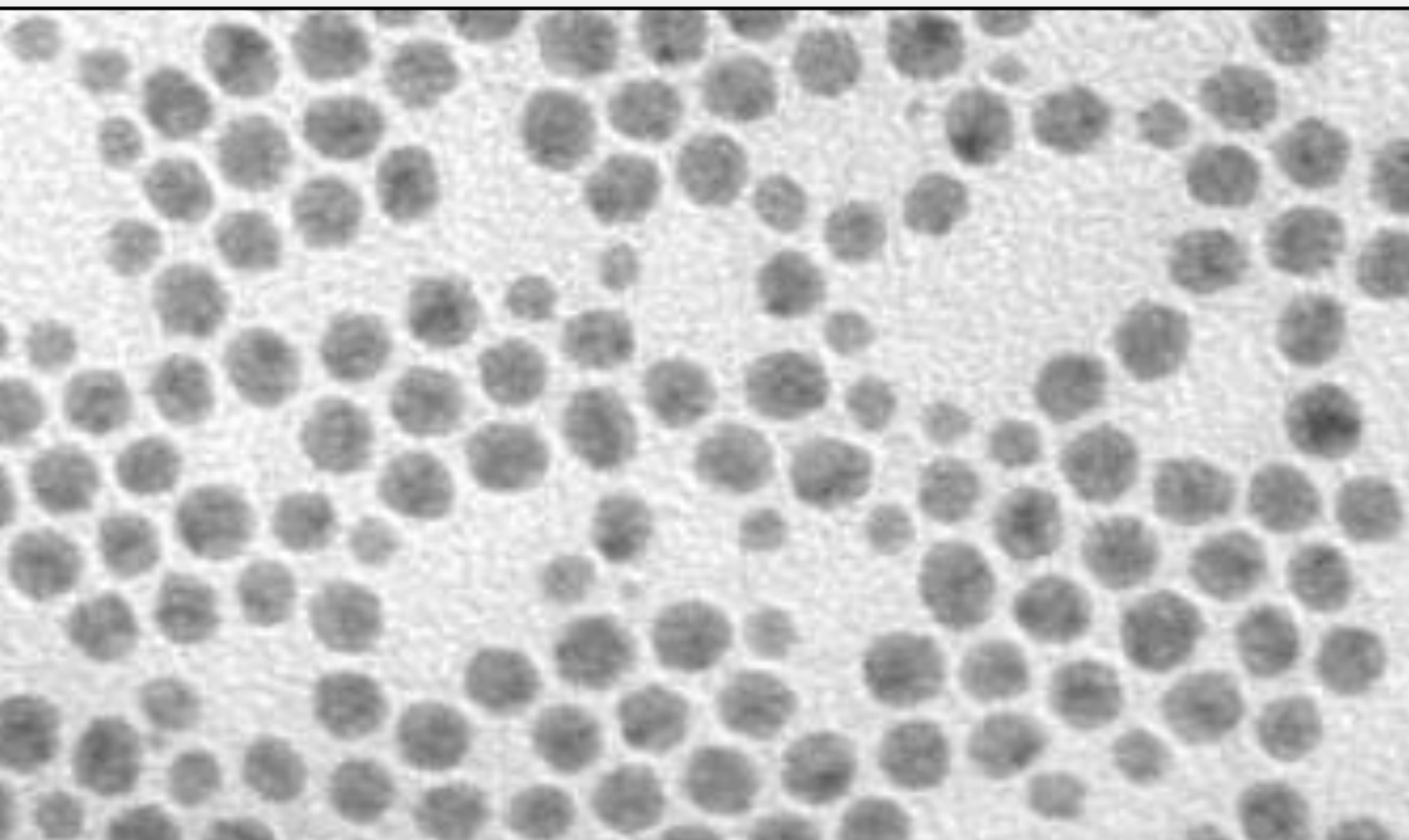
- [1] Y. Hori, R. Takahashi, Y. Yoshinami, A. Murata, *J. Phys. Chem. B* **1997**, *101*, 7075–7081.
- [2] Y. Hori, K. Kikuchi, S. Suzuki, *Lab. Tech. Biochem. Mol. Biol.* **1990**, *20*, 5–51.
- [3] Y. Hori, S. Suzuki, *Bull. Chem. Soc. Jpn.* **1982**, *55*, 660–665.
- [4] N. J. Firet, T. Burdyny, N. T. Nesbitt, S. Chandrashekar, A. Longo, W. A. Smith, *Catal. Sci. Technol.* **2020**, *10*, 5870–5885.
- [5] J. T. Feaster, C. Shi, E. R. Cave, T. Hatsukade, D. N. Abram, K. P. Kuhl, C. Hahn, J. K. Nørskov, T. F. Jaramillo, *ACS Catal.* **2017**, *7*, 4822–4827.
- [6] M. Ma, B. J. Trzeźniewski, J. Xie, W. A. Smith, *Angew. Chemie - Int. Ed.* **2016**, *55*, 9748–9752.
- [7] A. Loiudice, O. Segura Lecina, R. Buonsanti, *ACS Mater. Lett.* **2020**, *2*, 1182–1202.
- [8] S. E. Skrabalak, L. Au, X. Li, Y. Xia, *Nat. Protoc.* **2007**, *2*, 2182–2190.
- [9] Y. Sun, Y. Xia, *Science (80-.)* **2002**, *298*, 2176–2179.
- [10] A. Tao, P. Sinsermsuksakul, P. Yang, *Angew. Chemie - Int. Ed.* **2006**, *45*, 4597–4601.
- [11] M. Wuithschick, B. Paul, R. Bienert, A. Sarfraz, U. Vainio, M. Sztucki, R. Kraehnert, P. Strasser, K. Rademann, F. Emmerling, J. Polte, *Chem. Mater.* **2013**, *25*, 4679–4689.
- [12] P. Y. Lim, R. S. Liu, P. L. She, C. F. Hung, H. C. Shih, *Chem. Phys. Lett.* **2006**, *420*, 304–308.
- [13] J. E. van den Reijen, S. Kanungo, T. A. J. Welling, M. Versluijs-Helder, T. A. Nijhuis, K. P. de Jong, P. E. de Jongh, *J. Catal.* **2017**, *356*, 65–74.
- [14] G. L. Chai, Z. X. Guo, *Chem. Sci.* **2016**, *7*, 1268–1275.
- [15] Z. Sun, T. Ma, H. Tao, Q. Fan, B. Han, *Chem* **2017**, *3*, 560–587.
- [16] J. Wu, R. M. Yadav, M. Liu, P. P. Sharma, C. S. Tiwary, L. Ma, X. Zou, X. Zhou, B. I. Yakobson, J. Lou, P. M. Ajayan, **2015**, 5364–5371.
- [17] R. Jiang, E. Moton, J. P. McClure, Z. Bowers, *Electrochim. Acta* **2014**, *127*, 146–152.
- [18] J. Guo, A. Hsu, D. Chu, R. Chen, *J. Phys. Chem. C* **2010**, *114*, 4324–4330.
- [19] R. Beerthuis, J. W. de Rijk, J. M. S. Deeley, G. J. Sunley, K. P. de Jong, P. E. de Jongh, *J. Catal.* **2020**, *388*, 30–37.
- [20] K. P. De Jong, *Synthesis of Solid Catalysts*, Wiley-VCH, **2009**.

- [21] C. Kim, H. S. Jeon, T. Eom, M. S. Jee, H. Kim, C. M. Friend, B. K. Min, Y. J. Hwang, *J. Am. Chem. Soc.* **2015**, *137*, 13844–13850.
- [22] J. Wu, S. Ma, J. Sun, J. I. Gold, C. Tiwary, B. Kim, L. Zhu, N. Chopra, I. N. Odeh, R. Vajtai, A. Z. Yu, R. Luo, J. Lou, G. Ding, P. J. A. Kenis, P. M. Ajayan, *Nat. Commun.* **2016**, *7*, 1–6.
- [23] N. Yang, S. R. Waldvogel, X. Jiang, *ACS Appl. Mater. Interfaces* **2016**, *8*, 28357–28371.
- [24] W. Yang, W. Ma, Z. Zhang, C. Zhao, *Faraday Discuss.* **2018**, *210*, 289–299.
- [25] S. A. Mahyoub, F. A. Qaraah, C. Chen, F. Zhang, S. Yan, Z. Cheng, *Sustain. Energy Fuels* **2019**, *4*, 50–67.
- [26] Y. Yoon, A. S. Hall, Y. Surendranath, *Angew. Chemie - Int. Ed.* **2016**, *55*, 15282–15286.



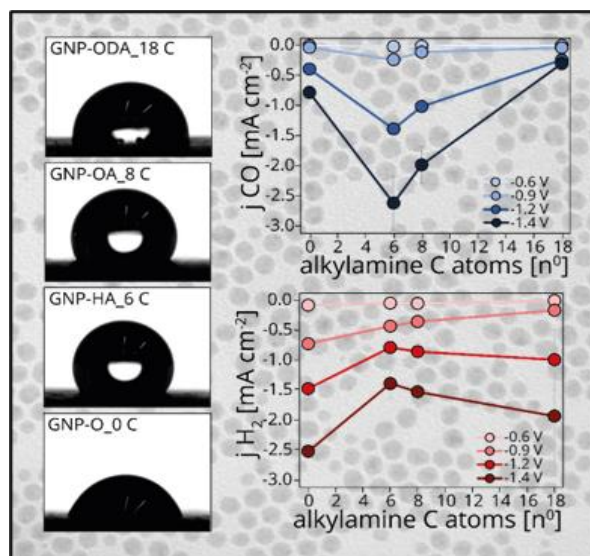
CHAPTER 4

Alkylamine-functionalized carbon supports for silver nanoparticles



Abstract

As an alternative method to the surface functionalization procedure described in the previous chapter, in this chapter, we describe how carbon supports were functionalized with linear alkylamines of different chain lengths, to understand its effect on electrochemical performance, in combination with colloidal silver nanoparticles (diameter = 8 nm). Alkylamines interact with the carbon surface and confer hydrophobic properties to the carbon support as well as making the local environment less acidic. These properties led not only to a suppression of the hydrogen evolution, but also to a remarkable enhancement in CO production. Despite the low silver weight loading ($0.0016 \text{ mg}_{\text{Ag}} \text{ cm}^{-2}$), hexylamine-functionalized carbon-based catalysts achieved a CO to H₂ ratio of 2.0, while the same material without the alkylamine functionalization only reached a ratio of 0.3, at -1.3 V vs RHE. This demonstrates the potential of hydrophobic functionalization for enhancing the CO selectivity of carbon-supported catalysts.



This chapter is based on the following manuscript:

Francesco Mattarozzi, Karen van den Akker, Matt Peerlings, Maaike Vink-van Ittersum, Nienke Visser, Rim van de Poll, Emiel Hensen, Peter Ngene and Petra de Jongh, 'Alkylamine-functionalized carbon supports to enhance the silver nanoparticles electrocatalytic reduction of CO₂ to CO', *ChemElectroChem*, **2023**, e202300295.

4.1 Introduction

The use of supported silver nanoparticles offer the opportunity to improve the electrocatalytic reduction of CO₂ to CO compared to the bulk metal, while lowering the cost of the expensive metal^[1]. Hence, many research groups have devoted much effort to synthesizing size-controlled silver nanoparticles supported on different substrates, such as titania^[2], zeolitic imidazolate frameworks^[3], highly pyrolytic graphite^[4], carbon nitride^[5], glassy carbon^[6] or activated carbon (chapter 3). Carbon is a great support material in electrochemistry, but its high selectivity towards water reduction limits its application^[7]. To overcome this drawback, strategies to modify the electronic structure of the carbon surface, such as doping the graphitic matrix, were adopted^{[8][9]}.

Functionalization represents an alternative approach to carbon doping. For instance, fluorinated polymers, such as polytetrafluoroethylene (PTFE)^[10] and molecules with a long hydrophobic alkyl chain, i.e. 1-octadecanethiol^[11], have been used to enhance the hydrophobicity of carbon materials, especially in the context of gas diffusion electrodes. These molecules suppress the H₂ formation by shielding the surface and hampering contact between carbon and water^[12]. For instance, the introduction of PTFE onto nickel-embedded nitrogen doped carbon nanotubes significantly improved the catalytic performance of the catalyst, by decreasing the H₂ partial current density by 50%, from -20 mA cm⁻² to -10 mA cm⁻² at -1.2 V, compared to the material without the hydrophobic polymer. This effect was correlated to an increase in contact angle between the electrolyte and the catalyst surface, confirmed by experiments performed with catalysts with different PTFE weight loadings^[13].

Furthermore, Wakerly et al. have shown that 1-octadecanethiol functionalization on the surface of hierarchically-structured copper dendrites not only suppressed the H₂ evolution, from 60% FE (hydrophilic electrode) to 10% FE (hydrophobic electrode) at -1.6 V, but also boosted the activity towards CO₂RR, increasing the C₁ products selectivity from 10% to 30% at the same potential^[14]. This observation was attributed to the ability of the hydrophobic copper electrodes to trap CO₂ bubbles at the electrode surface, resulting in a higher local concentration of CO₂ near the electrode surface^[15].

To solve the selectivity issues related to the use of high surface area carbon supports as, described in chapter 2 and 3, in this chapter we functionalized the hydrophilic graphitic carbon materials with different alkylamines *via* a one-step procedure, systematically varying the alkyl

chain length ($6 \leq \text{alkyl carbon atoms} \leq 18$). Furthermore, we investigate how alkylamine functionalization on carbon affects both the physical-chemical properties of the carbon and its electrocatalytic performance in CO_2RR . A low weight loading of colloidal silver nanoparticles ($0.0016 \text{ mg}_{\text{Ag}} \text{ cm}^{-2}$) was drop casted onto the functionalized electrodes to enable the CO_2 conversion to CO. We show that this approach leads to an increase in CO production and suppression of water reduction. At -1.4 V vs RHE, the hexylamine-functionalized carbon catalyst enabled both a 40% reduction in H_2 partial current density and a 225% increase in CO partial current density compared to the hydrophilic benchmark material. These results open the possibility to apply the same method for the preparation of gas diffusion electrodes.

4.2 Experimental section

4.2.1 Synthesis of silver nanoparticles

Silver nanoparticles were prepared *via* colloidal synthesis, by reducing silver nitrate with trioctylamine, and using tetradecyl phosphonic acid and oleic acid as capping agents^[16]. In summary, 170 mg of AgNO₃ (99.5%, Sigma Aldrich) and 278 mg of tetradecyl phosphonic acid (capping agent, 98.0%, Sigma Aldrich) were placed in a 100 mL three neck flask equipped with a condenser and a Teflon stirring bar. 20 mL of 1-octadecene (synthesis grade, Sigma Aldrich) was added as solvent. 0.7 mL of oleic acid (capping agent, 99.0%, Sigma Aldrich) and 1.0 mL trioctylamine (reducing agent, 98.0%, Sigma Aldrich) were added to the mixture. The flask was evacuated for 1 hour at room temperature. Subsequently, N₂ was introduced, and the temperature quickly increased to 60 °C. The thermocouple, connected to the heating mantle, was immersed in the solution inside a glass shell to avoid metal contamination. After 30 minutes at 60 °C, the solution turned from pale yellow to dark brown, indicating the formation of silver nanoparticles. Then, the solution was heated up to 100 °C and the temperature was held for 30 minutes. The solution was cooled down to room temperature. The final product was washed three times in 1 mL hexane (95.0%, Sigma-Aldrich) and 20 mL ethanol (99.5%, VWR chemicals). Between each washing step, the solution was centrifugated at 3000 rpm for 10 minutes, the solvent was decanted, and the product was collected at the bottom of the centrifuge tube. Finally, the solution was resuspended in hexane and stored in a glass vial, protected from direct light by an aluminum foil wrapped around it.

4.2.2 Synthesis of functionalized carbon powders

The synthesis of the oxidized carbon substrate (GNP-O₀C) has been described in chapter 2 and 3^[17]. In summary, 10 g of commercial graphitic nanoplatelets powder (GNP-500, grade C, XG-Science) was dispersed in HNO₃ (65.0% wt/wt, Sigma Aldrich), heated to 80 °C for 2 hours. The product was washed four times with deionized water, dried for 12 hours at 90 °C and ground in a mortar. Oxidized carbon materials were used as substrate for the alkylamine functionalization as they have enhanced interaction with the functionalizing molecules due to the carboxylic groups present on their surface.

The alkylamine functionalized carbons were produced by direct thermal mixing^{[18][19][20]}. 0.2 g of GNP-O_0 C was dispersed in 40 mL milli-Q water in a 100 mL three neck round bottom flask equipped with a condenser and a Teflon stirring bar. 1.1×10^{-3} moles of alkylamine were added. After 15 minutes sonication, the solution was heated to 100 °C for 20 hours at 400 rpm stirring rate. After cooling down to room temperature, the suspension was filtered, washed with milli-Q water, dried at 90 °C, and ground in a mortar. GNP-HA_6 C denotes the carbon functionalized with hexylamine (HA, 99.0%, Sigma Aldrich), GNP-OA_8 C functionalized with octylamine (OA, 99.5%, Acros Organics) and GNP-ODA_18 C the carbon functionalized with octadecylamine (ODA, 99.0%, Sigma Aldrich). The numbers following GNP-O, GNP-HA, GNP-OA and GNP-ODA indicate the number of carbon atoms in the linear alkyl chain of the alkylamines.

4.2.3 Synthesis of functionalized carbon electrodes

The cathodes were prepared by spraying the functionalized carbons onto a 4.9 cm² carbon paper substrate (Toray TGP-H-060). 11 mg of functionalized carbon was dispersed in 4470 µL milli-Q water, 1120 µL isopropanol (99.0%, Sigma Aldrich) and 44 µL Nafion solution (5.0% in water and 1-propanol, Alfa Aesar) and sonicated for 45 minutes. After sonication, a weight loading of 0.3 mg_{carbon} cm⁻² was applied by spraying the ink over the carbon paper, using a Conrad HP-200 Airbrush-Pistole. The modified carbon electrodes were dried overnight under vacuum at room temperature. Finally, a silver loading of 0.0016 mg_{Ag} cm⁻² on the carbon electrode was deposited by drop casting the colloidal silver nanoparticles onto the electrode.

4.2.4 Characterization

Images of colloidal silver particles were acquired by transmission electron microscopy (TEM) using a Thermo Fischer Scientific Tecnai 20 microscope, operated at 200 kV. The TEM grids were prepared by drop casting the silver nanoparticles colloidal solution onto a holey carbon 200 mesh copper grid. The silver nanoparticle average diameter was calculated by taking into account 5 different TEM images and 145 particles in total. The average diameter was calculated using equation 3.1 (chapter 3), where d_n is the diameter of particle n , and N is the total number of particles counted. UV-vis spectra were recorded using Agilent

Technologies Cary 60 UV-Vis. X-ray diffraction measurements both for the silver nanoparticles and functionalized carbon electrodes were performed on a Bruker D2 Phaser, equipped with a Co K α X-ray source with a wavelength of 1.79026 Å. The colloidal silver nanoparticles were drop cast onto a (911) single crystal silicon wafer before the XRD measurement, to maximize the signal to noise ratio.

Scanning electron microscopy (SEM) images were acquired on a Helios G3UC operated at 2 kV and the contrast in the final images was adjusted using ImageJ software. The XPS data were collected using a ThermoFischer Thermo Scientific K-Alpha X-ray Photoelectron Spectrometer, with an Al source (K α monochromatic radiation 1486.6 eV). The deconvolution and quantification of the silver peaks was achieved using CasaXPS. The energy scale was calibrated by setting the C 1s of adventitious carbon to a binding of 284.8 eV. For GNP-ODA_18 C, this approach was not possible, due to the insulating properties of the long alkyl amine, leading to a significant shift of the carbon peak due to the surface charging^{[21][22]}. In this case, the O 1s peak was set to 532.7 eV, the O feature belonging to the activated carbon GNP-O_0 C. The D-parameter and relative sp² – sp³ character of the functionalized carbon materials were calculated as the distance in between the minimum and maximum of the first differential of the carbon Auger peak. A linear relationship between the calculated D-parameter and the sp² – sp³ character of the carbon was assumed. The extremes of the series are diamond, which is fully sp³ with a D-parameter of 14, and highly oriented graphite, which is fully sp² with a D-parameter of 24^[23].

To determine the silver metal weight loading on the carbon paper support, the concentration of colloidal silver nanoparticles was measured by atomic absorption spectroscopy on a ContrAA 700 AAS instrument and multiplied by the amount of solution drop casted onto the electrodes. The contact angle measurements were performed on a Dataphysics OCA 15plus instrument, with water droplets of 4 μ L.

4.2.5 Electrocatalytic measurements

A polymethylmethacrylate (PMMA) three-electrode H-type cell was used for all the electrocatalytic experiments (figure 1.3). 15 mL electrolyte solution (0.1 M KHCO₃, pH=6.8, 99.0%, Sigma Aldrich) was added to both the cathodic and anodic compartments (headspace volume = 3 mL each). The two compartments were divided by a Nafion 117 membrane (Ion

Power). A flowrate of 10 mL min^{-1} CO_2 (Linde, purity 5.2) was applied for 1 hour prior to the experiments, to saturate the catholyte. The same CO_2 flowrate was applied during the experiments. Ar (10 mL min^{-1}) was bubbled through the anolyte solution. The working electrode was made of a glassy carbon disc (HTW-Germany) and the carbon paper disc (4.9 cm^2 , TGP-H-060, Toray), directly in contact with the electrolyte. The functionalized carbon catalysts ($0.3 \text{ mg}_{\text{carbon}} \text{ cm}^{-2}_{\text{carbon paper}}$) and the colloidal silver nanoparticles ($0.0016 \text{ mg}_{\text{Ag}} \text{ cm}^{-2}_{\text{carbon paper}}$) were deposited onto the carbon paper. The carbon paper surface area in contact with the electrolyte was 3.8 cm^2 . An Ag/AgCl (3 M KCl) reference electrode (Metrohm) was used, while a 3.8 cm^2 Pt disc (99.5%; Goodfellow) was used as counter electrode. The electrochemical measurements were performed using a Autolab PGSTAT204 potentiostat, and the applied potential was converted to the reversible hydrogen electrode potential (RHE) using the equation: $E_{\text{RHE}} = E_{\text{Ag/AgCl}} + 0.199 + 0.059 \text{ pH}$. The electrocatalytic performance was measured by chronoamperometry experiments, in which seven potentials per experiment were tested. Each potential was applied for 30 minutes.

The gaseous products were analyzed by gas chromatography, using Global Analysis Solution Microcompact GC 4.0 machine from InterScience, described in detail in a previous paper^[17]. Only CO and H_2 were detected as gaseous products and therefore included in the selectivity calculation. The selectivity of the process was defined by the FE, calculated using equation 2.2 (chapter 2). The partial current density defines the individual contribution of the reaction products to the total current density. This parameter was calculated as the product of the total current density and the FE.

All electrocatalytic data shown in this manuscript were the average of three experiments performed on two different batches of functionalized carbons and silver nanoparticles, synthesized, and tested by two different operators. The error bars were calculated using the standard deviation.

4.3 Results and discussion

4.3.1 Synthesis of silver nanoparticles

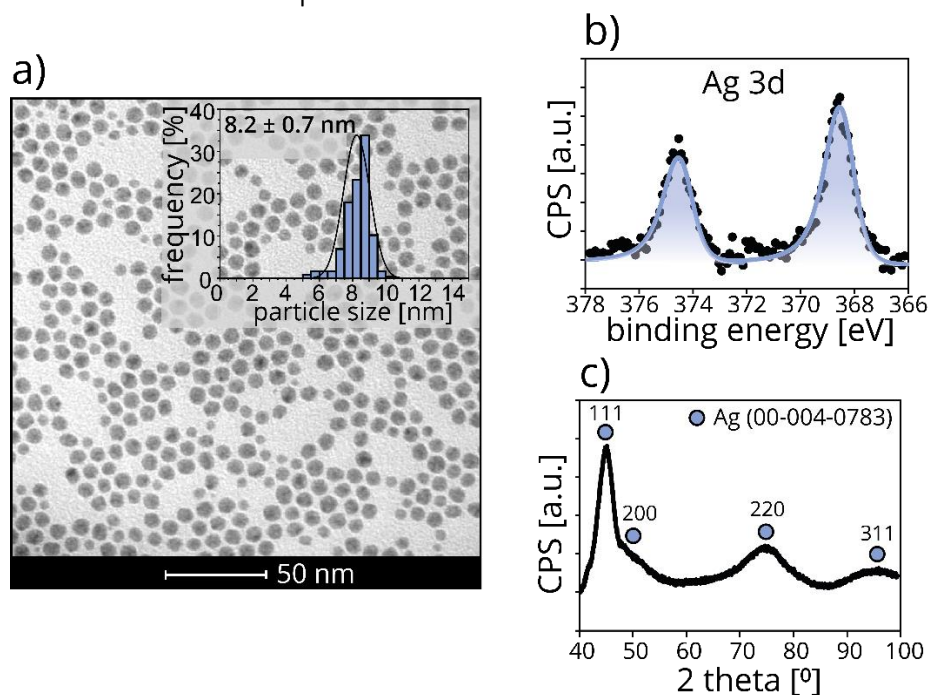


Figure 4.1 - a) TEM image of colloidal silver nanoparticles and particle size distribution (inset). b) XPS spectrum of silver nanoparticles supported on a carbon paper electrode. c) XRD pattern of colloidal silver particles drop casted on top of a (911) single crystal silicon wafer.

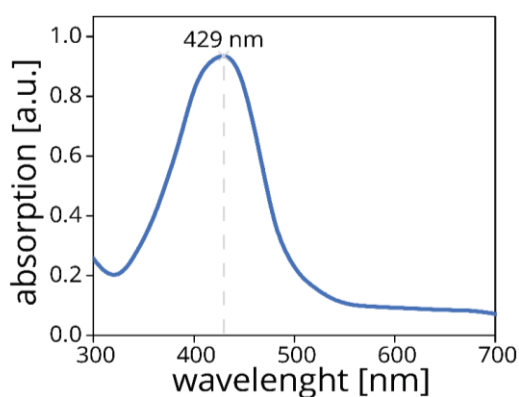


Figure 4.2 – UV-vis spectrum of colloidal silver nanoparticles dispersed in hexane.

Figure 4.1a shows the transmission electron microscopy (TEM) image of the as-synthesized colloidal silver nanoparticles and particle size distribution (inset). The silver

nanoparticles had an average particle size of 8.2 nm, and a narrow particle size distribution (standard deviation = 0.7 nm, figure 4.1a inset). The TEM image (figure 4.1a) demonstrates that most nanoparticles had a spherical morphology. Additional structural characterization using UV-vis measurements (figure 4.2) confirmed the formation of small and mono-dispersed silver nanoparticles^[24]. To investigate the surface and bulk oxidation state of the silver nanoparticles, both X-ray photoelectron spectroscopy (XPS) and X-ray diffraction (XRD) analysis were performed. Figure 4.1b shows that the surface of the silver nanoparticles is in the Ag⁰ state, as evidenced by the presence of metallic silver peaks, with the 3d features at 368.4 eV and 374.5 eV. The XRD pattern (figure 4.1c) clearly shows the (111), (200), (220) and (311) Bragg reflections of silver, confirming successful synthesis of face centered cubic metallic bulk silver nanoparticles. By applying the Scherrer equation to the peak broadening in the XRD pattern, an average crystallite size of 4 nm was calculated. This is smaller than the particle size (8.2 nm) measured by TEM, suggesting either polycrystalline particles or the presence of amorphous silver.

4.3.2 Carbon functionalization

Table 4.1 – XPS carbon (C), oxygen (O) and nitrogen (N) atomic percentages of GNP-O_0 C, GNP-HA_6 C, GNP-OA_8 C and GNP-ODA_18 C functionalized carbon powders without silver nanoparticles.

Sample ID	C atomic%	O atomic%	N atomic%
GNP-O_0 C	91.0	8.4	0.5
GNP-HA_6 C	93.0	5.5	1.5
GNP-OA_8 C	93.0	5.3	1.7
GNP-ODA_18 C	96.0	1.9	2.1

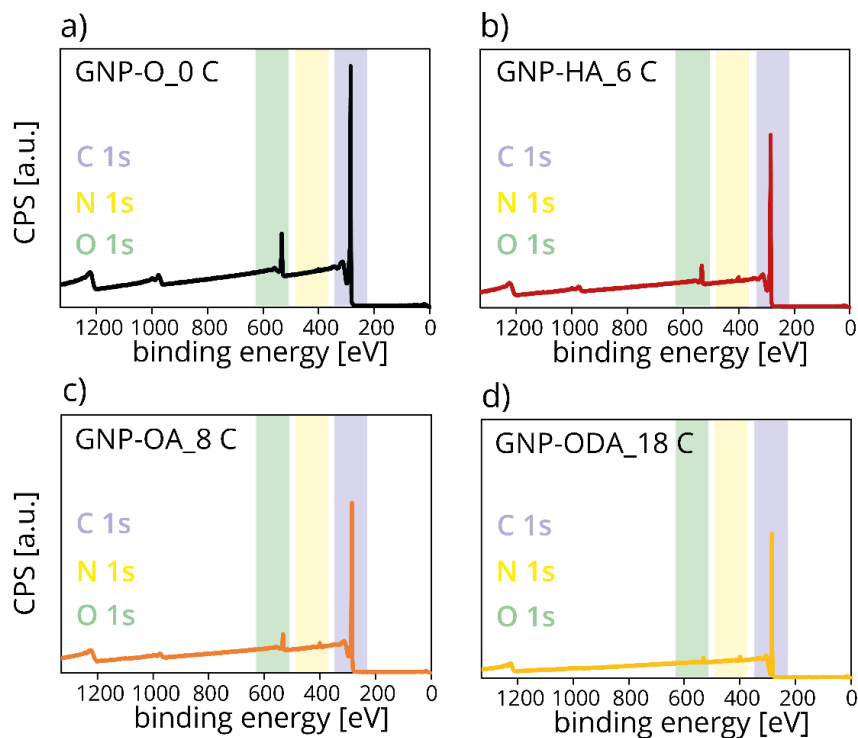


Figure 4.2- XPS survey spectrum of a) GNP-O_0 C, b) GNP-HA_6 C, c) GNP-OA_8 C and d) GNP-ODA_18 C functionalized carbon powders without silver nanoparticles.

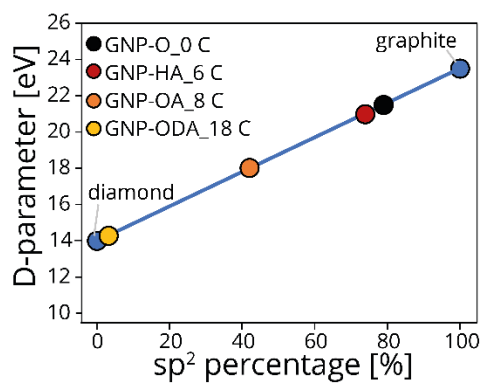


Figure 4.3 – D-parameter as a function of the sp^2 percentage for different functionalized carbons. The D-parameter represents the distance in between the minimum and maximum of the first differential of the carbon Auger peak (XPS). A linear relationship between the D-parameter and the sp^2 character of the carbon is found. The extremes of the series were diamond, fully sp^3 and with a D-parameter of 14, and highly oriented graphite, fully sp^2 with a D-parameter of 24.

Table 4.1 summarizes the carbon (C), oxygen (O) and nitrogen (N) atomic percentages of the functionalized carbon powders before loading with silver nanoparticles. These data were obtained from the XPS survey spectra (figure 4.2), which showed no metal impurities in the samples. GNP-O_0 C, the benchmark carbon material obtained by liquid phase oxidation of commercial graphitic carbon, displayed the highest content of oxygen (8.4 at%), and the lowest percentage of carbon and nitrogen, corresponding to 91.0 at% and 0.5 at%, respectively. The carbon content in GNP-HA_6 C and GNP-OA_8 C was 93.0 at%, with a similar oxygen content of 5.5 at% and 5.3 at%, respectively and similar nitrogen content of 1.5 at% and 1.7 at%. GNP-ODA_18 C displayed the highest carbon content (96.0 at%) and nitrogen content (2.1 at%), and the lowest oxygen content (1.9 at%). The increase in carbon content and decrease in oxygen content from GNP-O_0 C to GNP-ODA_18 C is explained by the increasingly longer carbon chains, from 0 to 18 carbon atoms, shielding the oxygen atoms of the carbon support surface. This hypothesis is supported by the higher surface sp^3 character of the alkyl amine functionalized carbon materials (figure 4.3), which is different from the high sp^2 percentage in GNP-O_0 C, calculated as the D-parameter from the carbon Auger peak. The increase in nitrogen content for GNP-HA_6 C, GNP-OA_8 C and GNP-ODA_18 C is attributed to the amine functionality of the alkylamines.

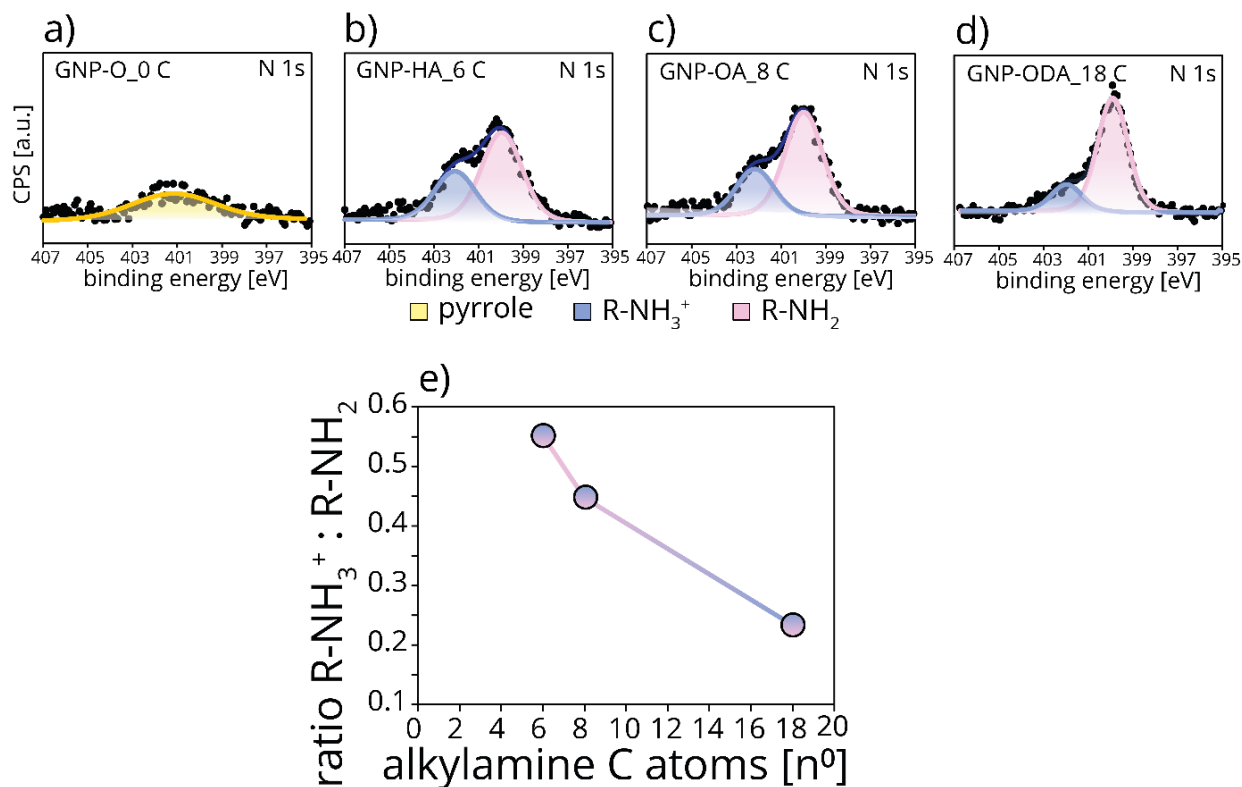


Figure 4.4 – XPS spectrum of a) GNP-O_0 C, b) GNP-HA_6 C, c) GNP-OA_8 C and d) GNP-ODA_18 C functionalized carbon powders without silver nanoparticles. e) ratio between protonated amine (R-NH₃⁺) and free amine (R-NH₂) as a function of the alkyl amine chain length for the functionalized samples.

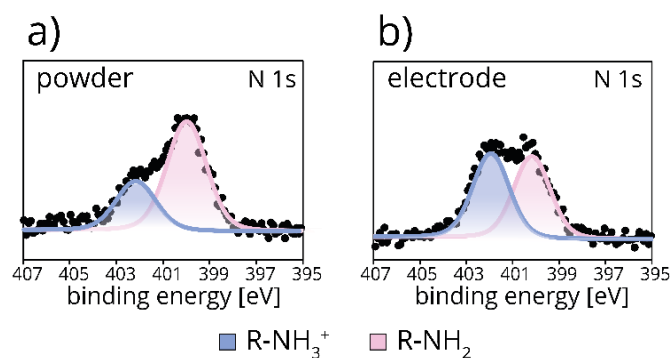


Figure 4.5 – N1s XPS spectra for a) GNP-OA_8 C powder (before spraying onto the carbon paper) and b) GNP-OA_8 C after spraying onto the carbon paper.

To further investigate the chemical nature of the nitrogen atoms, the high-resolution N 1s XPS spectra were deconvoluted and the abundance of the different N species was quantified (figure 4.4). GNP-O_0 C (figure 4.4a) showed only native pyrrolic groups, while the alkylamine functionalized carbons showed different ratios between amine (R-NH₂, pink) at 400 eV and protonated amine (R-NH₃⁺, blue) groups at 402 eV (figure 4.4 b-d)^[25]. These results demonstrate that a fraction of the alkylamines was simply physically adsorbed at the surface of the carbon powder (R-NH₂ peak), while part of the alkylamines electrostatically interacted with the acidic carbon surface groups (R-NH₃⁺ peak)^[26].

Figure 4.4e shows the atomic ratio of the protonated to absorbed amine groups as a function of the number of carbon atoms in the linear alkyl chains. GNP-HA_6 C showed the highest ratio (0.55), followed by GNP-OA_8 C (0.44) and GNP-ODA_18 C (0.23). This means that the longer alkyl chains interact less strongly with the polar surface groups. This could be due to steric hindrance of the alkyl chain, which limits the electrostatic interaction with the acidic surface groups of the carbon. After spraying the functionalized carbon onto the carbon paper, the ratio between protonated amines and free amines increased (figure 4.5), suggesting a weak interaction between the physically adsorbed amines (R-NH₂ peak at 400 eV) and the surface of the oxidized carbon.

These results indicate that the GNP-O carbon was successfully functionalized with the alkylamines, as further evidenced by the point of zero charge analysis, measured *via* mass titration (table 4.2). This analysis showed that starting from the acidic GNP-O_0 C surface (PZC = 3.1), modification with the alkylamines neutralized the acidic sites, leading to a nearly neutral surface (PZC ~ 7).

Table 4.2 – PZC for differently functionalized carbon powders.

Sample ID	PZC [pH]
GNP-O_0 C	3.4
GNP-HA_6 C	7.4
GNP-OA_8 C	7.6
GNP-ODA_18 C	6.8

4.3.3 Carbon supported silver nanoparticles (electrodes)

To prepare the electrode materials, the oxidized (GNP-O_0 C) and hydrophobic functionalized (GNP-HA_6 C, GNP-OA_8 C and GNP-ODA_18 C) carbon materials were sprayed onto a carbon paper support. After this, a low loading ($0.0016 \text{ mg Ag cm}^{-2}$) of colloidal silver nanoparticles was drop casted onto the electrodes. As the main aim of the alkylamine functionalization was to decrease the wettability of the carbon surface, the hydrophilic/hydrophobic properties of the carbon supported silver nanoparticle electrodes were determined using contact angle measurements.

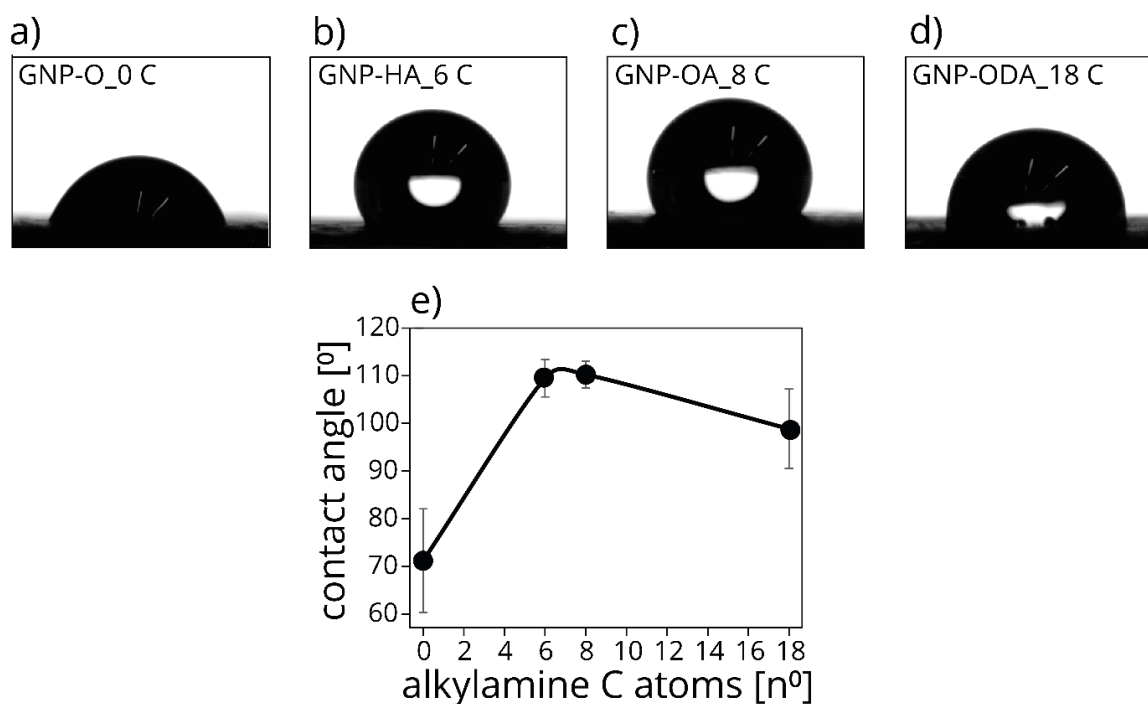


Figure 4.6 – Photos of 4 μL of water on the surface of a) GNP-O_0 C, b) GNP-HA_6 C, c) GNP-OA_8 C and d) GNP-ODA_18 C functionalized carbon electrodes with silver nanoparticles. e) contact angles as a function of the alkyl amine chain length.

Figure 4.6 shows representative contact angle images for a) GNP-O_0 C, b) GNP-HA_6 C, c) GNP-OA_8 C and d) GNP-ODA_18 C catalysts with $0.0016 \text{ mg}_{\text{Ag}} \text{ cm}^{-2}$, while figure 4.6e gives the contact angles as a function of the alkylamine chain length. GNP-O_0 C possessed a

moderately hydrophilic character, with a 71° contact angle. GNP-HA_6 C and GNP-OA_8 C were most hydrophobic, with contact angles of 109° and 110° , respectively. GNP-ODA_18 C exhibited a 100° contact angle, slightly lower than GNP-HA_6 C and GNP-OA_8 C. The hydrophilicity of GNP-O_0 C is explained by the presence of O-containing polar groups, which enhanced the wettability of the electrode. The hydrophobicity of GNP-HA_6 C and GNP-OA_8 C was due to the poor interaction between the long alkyl chains of the alkylamine moieties and water. This shows that the hydrophilic O-containing groups were successfully shielded by the alkylamine hydrophobic chains. GNP-ODA_18 C showed a slightly less hydrophobic surface compared to GNP-HA_6 C and GNP-OA_8 C. This indicates that the different hydrophobicity cannot be explained solely by the length of the alkylamines, but possibly other factors, such as a different surface morphology, and/or a different dispersion of functionalized carbon on the electrode surface for long alkyl chains.

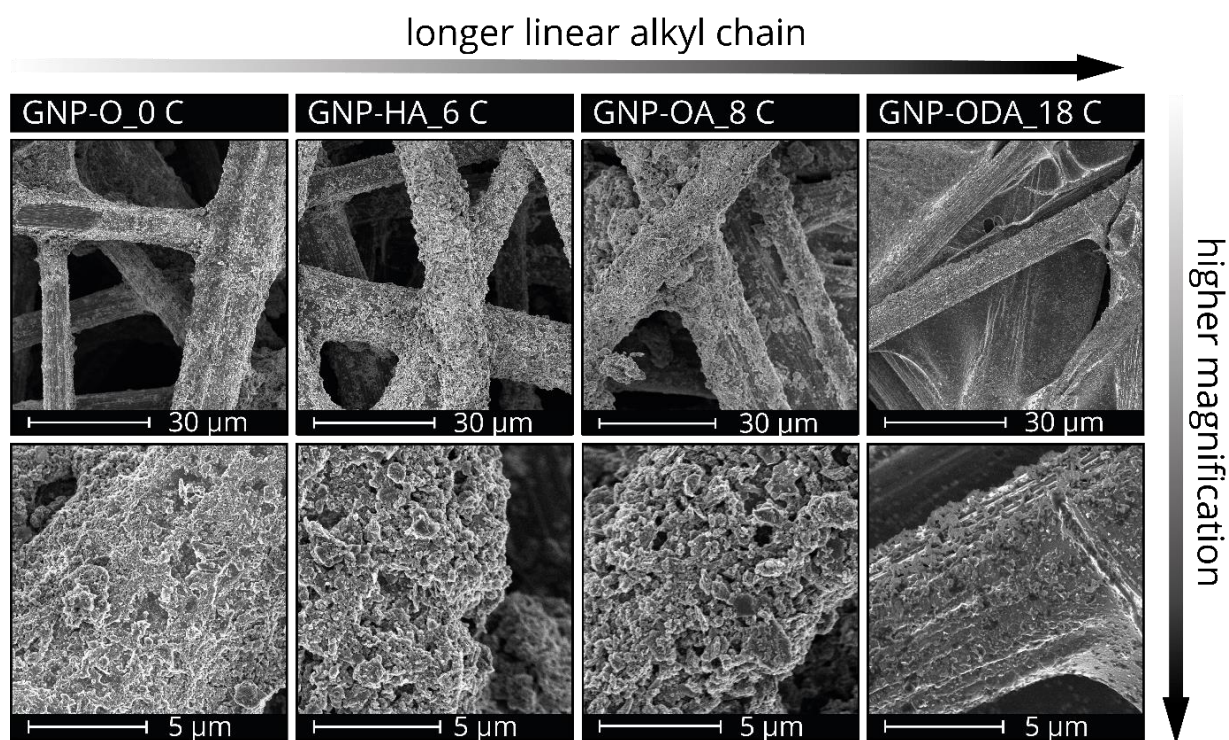


Figure 4.7 – Scanning Electron Microscopy (SEM) images of GNP-O_0 C, GNP-HA_6 C, GNP-OA_8 C and GNP-ODA_18 C carbon electrodes with Ag nanoparticles.

To further investigate the origin of the difference in hydrophobicity, Scanning Electron Microscopy (SEM) measurements were performed. Figure 4.7 shows low magnification (top) and high magnification (bottom) SEM images of GNP-O_0 C, GNP-HA_6 C, GNP-OA_8 C and GNP-ODA_18 C electrodes. GNP-O_0 C, GNP-HA_6 C and GNP-OA_8 C possessed a qualitatively similar distribution of carbon particles over the fibers of the carbon paper. All three catalysts were uniformly coated on the carbon fibers (low magnification images) with sharp-edged particles (high magnification images). GNP-ODA_18 C showed a non-uniform distribution of the carbon powder, with most of carbon fibers of the substrate not covered by the soft-edged particles. The different carbon paper coverages between the catalysts might explain the lower hydrophobicity for GNP-ODA_18 C, compared to the other alkyl functionalized catalysts.

4.3.4 Electrocatalytic performance: influence of hydrophobic functionalization on the catalysts' selectivity

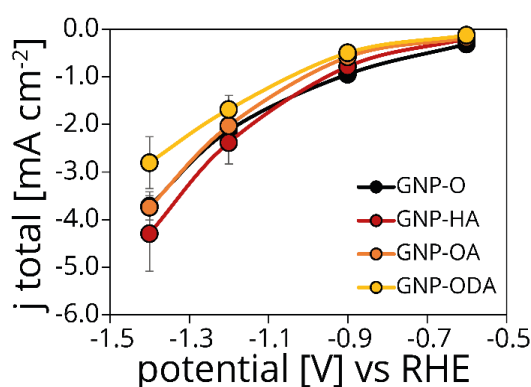


Figure 4.8 – Geometric total current densities as a function of the applied potential. Each data point corresponds to the average current measured by chronoamperometry applying a constant potential for 30 minutes.

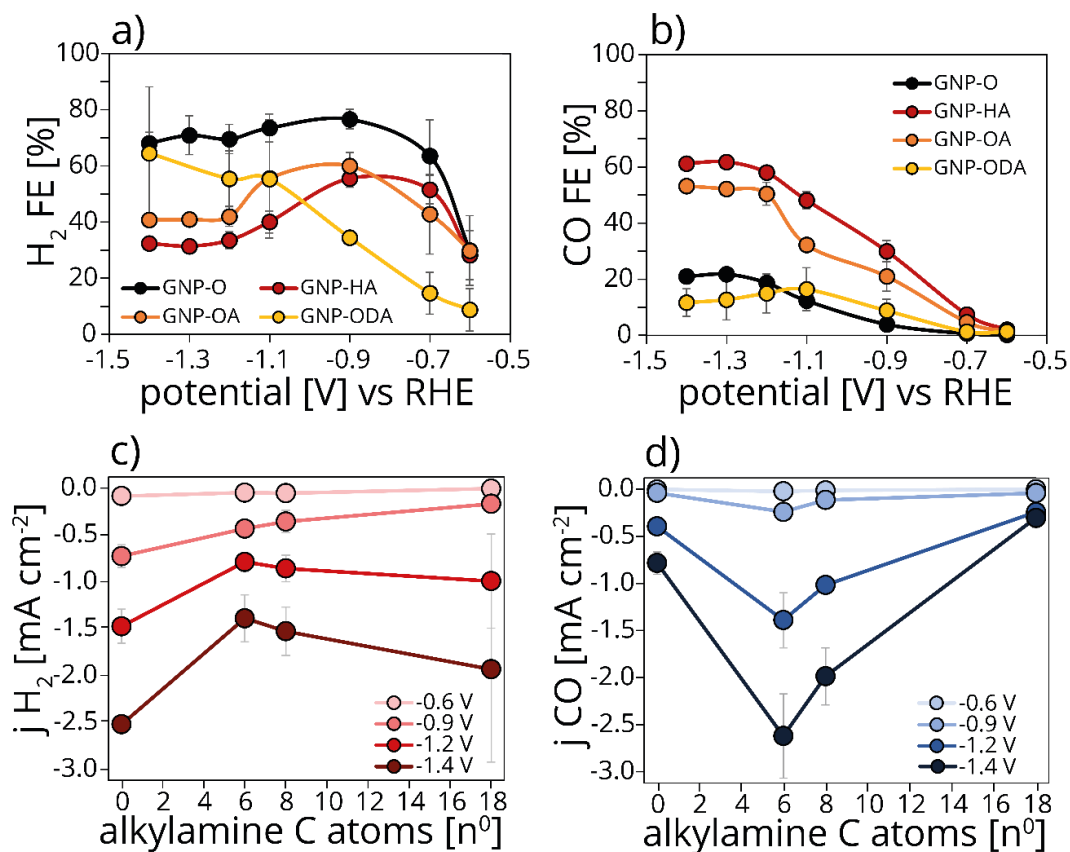


Figure 4.9 - a) H_2 and b) CO faradaic efficiencies as a function of the applied potential, calculated for the four different functionalized carbon catalysts. c) H_2 and d) CO partial current densities as a function of the number of carbon atoms in the alkyl chain, measured as average over 30 minutes.

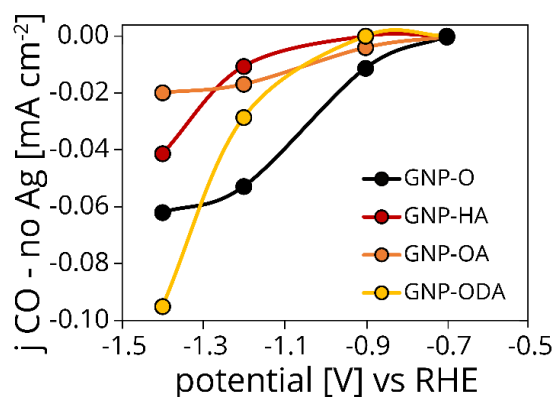


Figure 4.10 – CO geometric partial current densities as a function of the potential for all modified carbon materials (without Ag nanoparticles).

To investigate the effect of hydrophobic functionalization on the total current density (figure 4.8) and selectivity (figure 4.9), potentiostatic measurements were performed in 0.1 M KHCO_3 , applying each potential for 30 minutes. Both figures have been simplified, but the full range of potentials measured is reported in 4.9a and b. Figure 4.8 shows the geometric total current density for the four catalysts, as a function of the applied potential. The electrocatalysts generated similar current densities at low overpotentials, up to -1.1 V. At more negative potentials, GNP-ODA_18 C showed the smallest current densities, with only -1.6 mA cm^{-2} and -2.8 mA cm^{-2} at -1.2 V and -1.4 V respectively. In the same potential range, GNP-O_0 C, GNP-HA_6 C and GNP-OA_8 C produced similar current densities. These catalysts produced their largest current density at -1.4 V, with -3.7 mA cm^{-2} for both GNP-O_0 C and GNP-OA_18 C, and -4.3 mA cm^{-2} for GNP-HA_6 C. The small current density generated by GNP-ODA_18 C could be explained by non-uniform distribution of the functionalized carbon catalysts, which left a large fraction of the low activity carbon fibers of the carbon paper bare.

To separate the contribution of water reduction and the CO_2RR to the total current and thereby probe the influence of the hydrophobic functionalization on the selectivity, the H_2 and CO partial current densities were calculated based on the CO and H_2 product formation rates as a function of the alkyl chain length. This analysis was derived by combining the faradaic efficiency data (figure 4.9a and b) and the total current densities. Figure 4.9c clearly shows that the alkylamine functionalization suppressed the H_2 partial current density. GNP-O_0 C was undoubtedly the catalyst with the highest H_2 production, both at low and high overpotentials, generating a maximum of -2.5 mA cm^{-2} at -1.4 V. GNP-HA_6 C and GNP-OA_8 C showed the lowest overall hydrogen production, with only -1.4 mA cm^{-2} and -1.5 mA cm^{-2} respectively at the largest overpotential. The suppression of the hydrogen evolution reaction for the alkylamine functionalized catalysts is mainly ascribed to a lower wettability of the hydrophobically functionalized materials (figure 4.6), leading to limited water accessibility to the carbon surface. The difference in local environment between GNP-O_0 C and the other catalysts might also play a role in the suppression of the H_2 evolution reaction, as the alkylamine functionalization shields the acidic surface groups on the carbon surface, leading to a less acidic pH close to the electrode surface. This might be relevant especially in the low potential range, where the total current density is small, and the proton consumption is limited.

Also the CO partial current density (figure 4.9d) was greatly influenced by the functionalization. GNP-HA_6 C and GNP-OA_8 C produced a larger current density than the activated carbon GNP-O_0 C and GNP-ODA_18 C. At -1.2 V, both GNP-HA_6 C and GNP-OA_8 C generated a 3.5- and 6.6- fold CO partial current density enhancement compared to GNP-O_0 C and GNP-ODA_18 C, respectively. Under the largest potential bias (-1.4 V), GNP-HA_6 C produced -2.6 mA cm^{-2} , while GNP-O_0 C, GNP-OA_8 C and GNP-ODA_18 C displayed only -0.8 mA cm^{-2} , -2.0 mA cm^{-2} and -0.3 mA cm^{-2} , respectively. The same trend was found by calculating the CO partial current density normalized by silver surface area, as a function of the applied potential.

The remarkable enhancement in CO production observed for GNP-HA_6 C and GNP-OA_8 C could be explained by the so-called “plastron effect”^[14]: the presence of a thin gas layer near the surface of the functionalized electrodes, increases the local concentration of CO_2 . GNP-ODA_18 C performed worse than GNP-O_0 C. The 18-carbon atom chain might shield the active sites for CO_2RR (silver nanoparticles). Control experiments on the modified carbon electrodes without silver nanoparticles confirmed that the alkylamine functionalization alone did not steer the selectivity towards CO (figure 4.10).

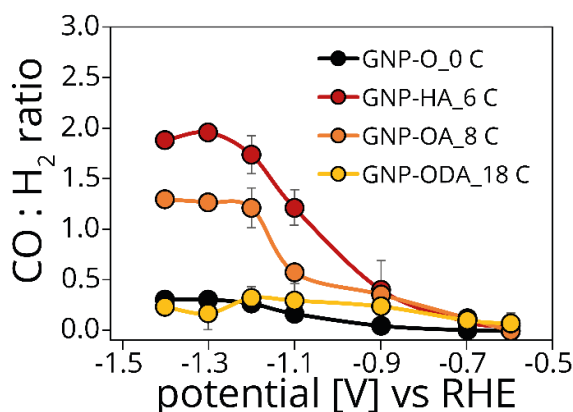


Figure 4.11 – CO to H_2 ratio as a function of the applied potential.

An important parameter is the produced ratio of CO to H_2 (figure 4.11). At low overpotentials, all the alkyl functionalized materials outperformed GNP-O_0 C. At -1.2 V, GNP-ODA_18 C generated a CO to H_2 ratio of 0.3, like GNP-O_0 C, while GNP-OA_8 C and GNP-HA_6 C showed a ratio of 1.2 and 1.7, respectively. At -1.3 V, GNP-HA_6 C reached the

maximum CO to H₂ ratio, equal to 2.0, while GNP-OA_8 C, GNP-O_0 C and GNP-ODA_18 C only produced a ratio of 1.3, 0.3 and 0.2. At more cathodic biases, the catalysts seem to reach a plateau, indicating no further improvement in CO selectivity. These results present an effective strategy to reduce the competitive hydrogen evolution reaction and steer the selectivity towards CO production for carbon-based electrodes. This was successfully achieved by introducing hydrophobic functional groups on the surface of activated carbons.

4.4 Conclusions

A series of four modified carbon materials, functionalized either with oxygen-containing groups (GNP-O_0 C, benchmark) or with amines with different number of carbon atoms in the linear alkyl chain, i.e. hexylamine (GNP-HA_6 C), octylamine (GNP-OA_8 C) and octadecylamine (GNP-ODA_18 C) was produced. 0.0016 mg_{Ag} cm⁻² of colloidal silver nanoparticles (8.2 nm diameter) was drop cast on the carbon materials. Both XPS and contact angle measurements demonstrated that the alkylamines were successfully deposited on the carbon, making the electrode surface more hydrophobic and less acidic. The alkylamine-functionalized carbons exhibited significantly lower H₂ partial current densities and increased CO current densities compared to the oxygen functionalized carbon. This clearly shows that alkylamine functionalization is beneficial for the electrocatalytic performance of carbon-based electrodes for CO production.

Acknowledgements

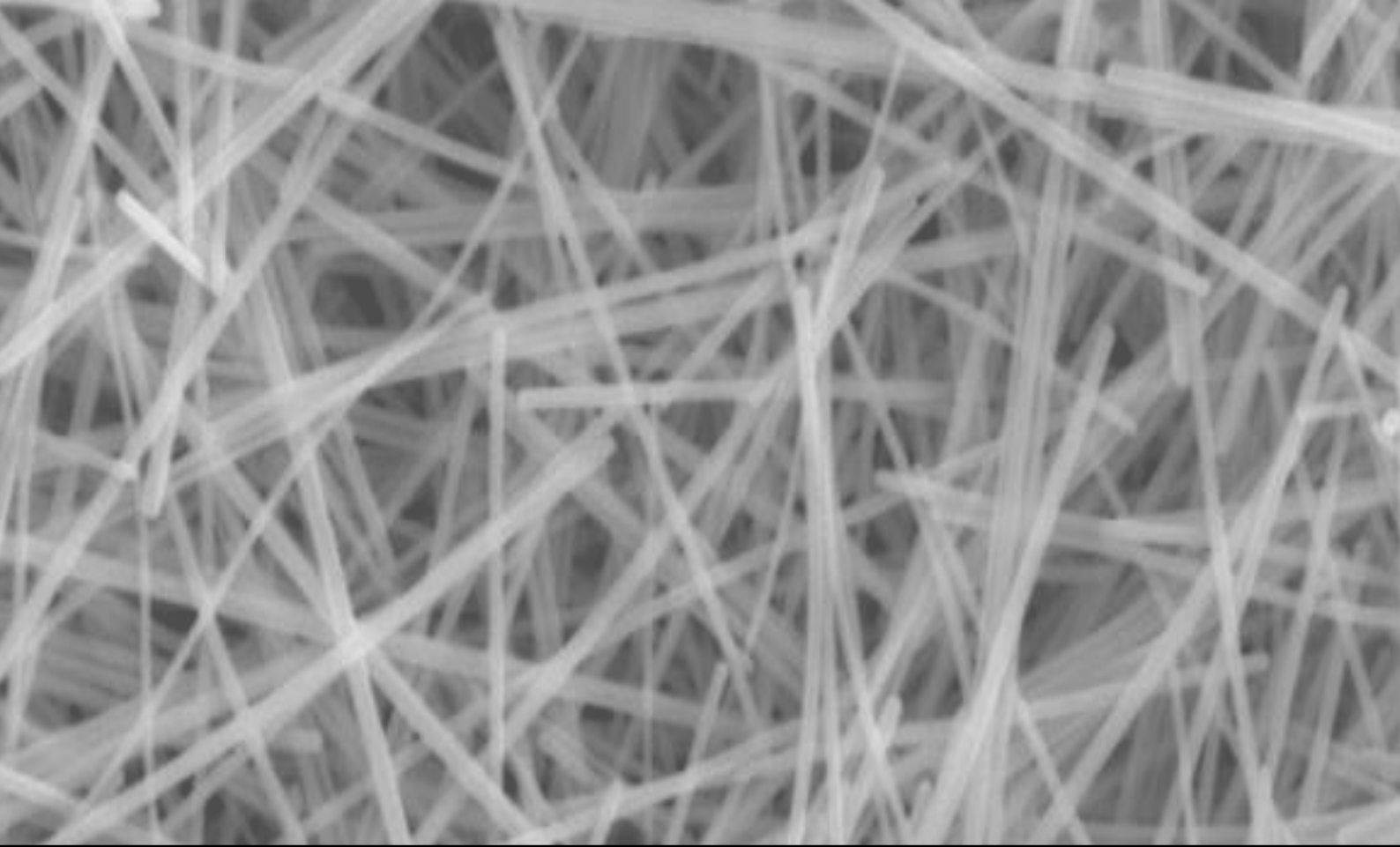
Nienke Visser was funded by TotalEnergies OneTech Belgium. Stephan Jonker is acknowledged for the precious help with atomic absorption spectroscopy measurements. Alex van Silfhout is acknowledged for his help during the contact angle measurements. Jan Willem de Rijk is acknowledged for the technical support, helping both with the cell design and the preparation of the catalytic set-up during this project. Valerio Gulino is acknowledged for the useful discussion of the project results.

References

- [1] C. Kim, H. S. Jeon, T. Eom, M. S. Jee, H. Kim, C. M. Friend, B. K. Min, Y. J. Hwang, *J. Am. Chem. Soc.* **2015**, *137*, 13844–13850.
- [2] S. Ma, Y. Lan, G. M. J. Perez, S. Moniri, P. J. A. Kenis, *ChemSusChem* **2014**, *7*, 866–874.
- [3] Z. Zhuang, Y. Zhang, L. Hu, J. Wang, Z. Zhang, W. Han, *Adv. Mater. Lett.* **2020**, *11*, 19369–19409.
- [4] X. Deng, D. Alfonso, T. D. Nguyen-Phan, D. R. Kauffman, *ACS Catal.* **2022**, *12*, 5921–5929.
- [5] S. Zhang, Z. Mo, J. Wang, H. Liu, P. Liu, D. Hu, T. Tan, C. Wang, *Electrochim. Acta* **2021**, *390*, 138831.
- [6] J. Huang, M. Mensi, E. Oveisi, V. Mantella, R. Buonsanti, *J. Am. Chem. Soc.* **2019**, *141*, 2490–2499.
- [7] Z. Sun, T. Ma, H. Tao, Q. Fan, B. Han, *Chem* **2017**, *3*, 560–587.
- [8] J. Wu, R. M. Yadav, M. Liu, P. P. Sharma, C. S. Tiwary, L. Ma, X. Zou, X. Zhou, B. I. Yakobson, J. Lou, P. M. Ajayan, **2015**, 5364–5371.
- [9] J. Yuan, W. Y. Zhi, L. Liu, M. P. Yang, H. Wang, J. X. Lu, *Electrochim. Acta* **2018**, *282*, 694–701.
- [10] B. Kim, F. Hillman, M. Ariyoshi, S. Fujikawa, P. J. A. Kenis, *J. Power Sources* **2016**, *312*, 192–198.
- [11] S. C. Perry, S. Mavrikis, M. Wegener, P. Nazarovs, L. Wang, C. Ponce De León, *Faraday Discuss.* **2021**, *230*, 375–387.
- [12] M. Li, M. N. Idros, Y. Wu, T. Burdyny, S. Garg, X. S. Zhao, G. Wang, T. E. Rufford, *J. Mater. Chem. A* **2021**, *9*, 19369–19409.
- [13] R. Chen, W. Tian, Y. Jia, W. Xu, F. Chen, X. Duan, Q. Xie, C. Hu, W. Liu, Y. Zhao, Y. Kuang, Y. Zhang, X. Sun, *ACS Appl. Energy Mater.* **2019**, *2*, 3991–3998.
- [14] D. Wakerley, S. Lamaison, F. Ozanam, N. Menguy, D. Mercier, P. Marcus, M. Fontecave, V. Mougél, *Nat. Mater.* **2019**, *18*, 1222–1227.
- [15] E. A. Hebets, R. F. Chapman, *J. Insect Physiol.* **2000**, *46*, 13–19.
- [16] L. Wu, K. E. Kolmeijer, Y. Zhang, H. An, S. Arnouts, S. Bals, T. Altantzis, J. P. Hofmann, M. Costa Figueiredo, E. J. M. Hensen, B. M. Weckhuysen, W. Van Der Stam,

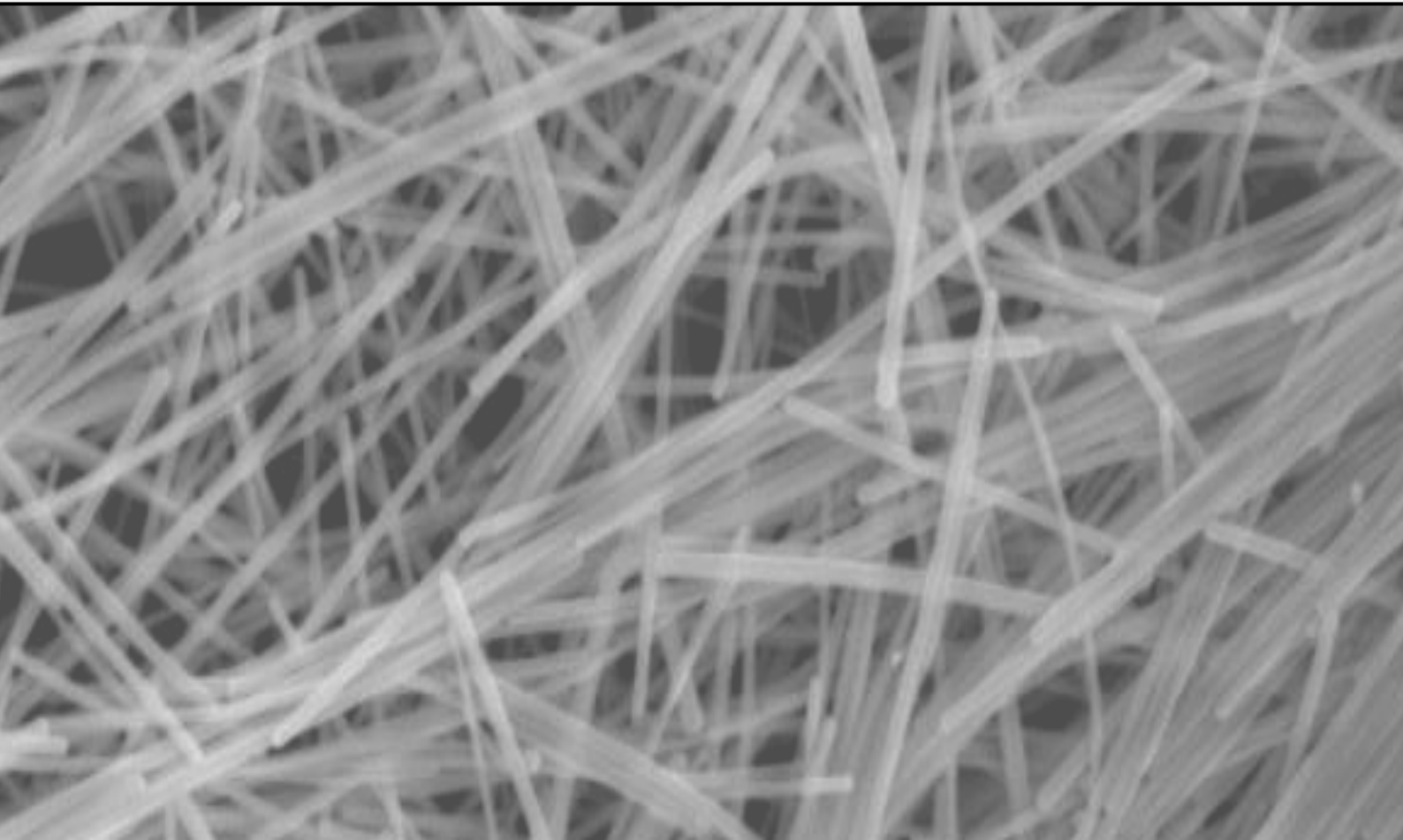
Nanoscale **2021**, *13*, 4835–4844.

- [17] F. Mattarozzi, N. Visser, J. W. de Rijk, P. Ngene, P. de Jongh, *Eur. J. Inorg. Chem.* **2022**, e202200365.
- [18] D. Tasis, N. Tagmatarchis, A. Bianco, M. Prato, *Chem. Rev.* **2006**, *106*, 1105–1136.
- [19] Z. Spitalsky, D. Tasis, K. Papagelis, C. Galiotis, *Prog. Polym. Sci.* **2010**, *35*, 357–401.
- [20] T. Bao, Z. Wang, Y. Zhao, Y. Wang, X. Yi, *Materials* **2018**, *11*, 1710.
- [21] G. Greczynski, L. Hultman, *Prog. Mater. Sci.* **2020**, *107*, 100591.
- [22] K. Artyushkova, *J. Vac. Sci. Technol. A* **2020**, *38*, 031002.
- [23] D. J. Morgan, *C* **2021**, *7*, 51.
- [24] A. T. Le, L. T. Tam, P. D. Tam, P. T. Huy, T. Q. Huy, N. Van Hieu, A. A. Kudrinskiy, Y. A. Krutyakov, *Mater. Sci. Eng. C* **2010**, *30*, 910–916.
- [25] W. Quan, X. Wang, C. Song, *Energy and Fuels* **2017**, *31*, 9517–9528.
- [26] W. Quan, X. Jiang, X. Wang, C. Song, *ACS Sustain. Chem. Eng.* **2020**, *8*, 9998–10008.



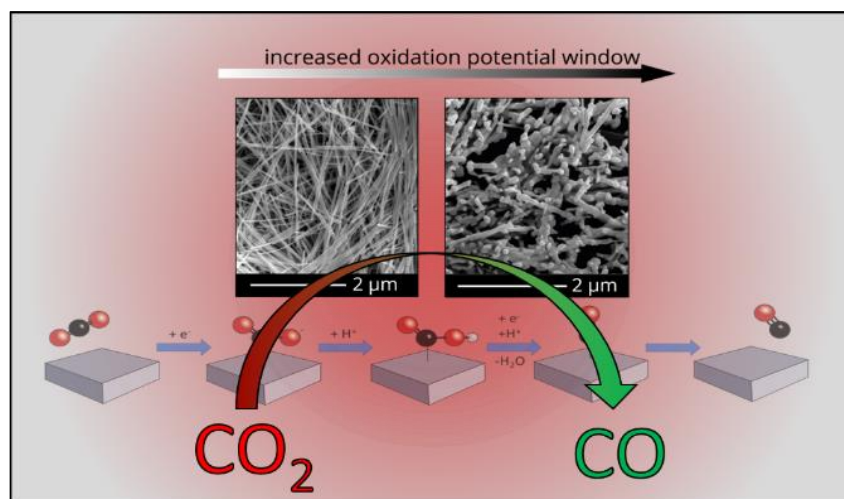
CHAPTER 5

Oxide-derived silver nanowires



Abstract

Compared to nanoparticles, silver nanowires show an enhanced selectivity towards CO. Recent publications proved that oxide-derived electrocatalysts can exhibit better catalytic performance than the pristine metal phase, but oxide-derived silver nanowires have not been investigated. In this chapter, we report for the first time the electrocatalytic properties of silver nanowires, synthesized *via* the polyol method, and pretreated by electrochemical oxidation in basic electrolyte. By increasing the oxidation potential, both the percentage of Ag_xO and the surface roughness of the catalyst were progressively increased. The most oxidized sample showed a remarkably improved CO selectivity ($-294.2 \text{ mA m}^{-2}_{\text{Ag}}$), producing a 3.3-fold larger CO partial current density than the pristine sample ($-89.4 \text{ mA m}^{-2}_{\text{Ag}}$), normalized by electrochemically active silver surface area. This work demonstrates the beneficial effect of the controlled oxidation treatment even on highly selective nanostructures such as silver nanowires.



This chapter is based on the manuscript:

Francesco Mattarozzi, Nolan van der Willige, Valerio Gulino, Claudia Keijzer, Rim van de Poll, Emiel Hensen, Peter Ngene and Petra de Jongh, 'Oxide-derived silver nanowires for CO₂ electrocatalytic reduction to CO', *ChemCatChem*, **2023**, e202300792

5.1 Introduction

Silver nanowires perform remarkably well catalytically compared to polycrystalline electrodes and nanoparticles^{[1][2][3]}. For instance, it was shown that nanowires (100 nm in diameter) produced a higher selectivity (up to 70% faradaic efficiency) towards CO compared to polycrystalline nanoparticles (40% faradaic efficiency), at relatively modest overpotential (*i.e.* -1.2 V vs RHE). This was attributed to the high (100) to (111) facet ratio and edge to corner ratio in the 1-D nanostructure, which lowers the activation energy for the rate determining step of the reaction (first electron transfer to CO₂), as shown by DFT calculations^[4]. Furthermore, nanowires possess high surface area and are suitable for surface modifications, as common synthesis procedures, such as the polyol method, aim to generate relatively thick nanowires (25 nm < diameter < 100 nm). For instance, the structure of silver nanowires was modified *via* wet-chemical sulfidation, introducing surface defects after the stripping of the sulfur atoms^[5]. Although the surface roughening modified part of the original crystalline structure, it also formed active sites that led to a 20% increase in CO faradaic efficiency compared to the pristine wires (50% CO faradaic efficiency) at -0.9 V. However, the sulfidation treatment involves a complicated chemical step, implies the use of additional chemicals and the risk of H₂S evolution.

A similar approach to enhance the electrochemical performance of transition metal electrodes, involves the oxidation and subsequent reduction^{[6][7]}. For instance, it has been demonstrated that an oxide-derived (OD-) nanoporous gold electrode, produced by electrochemical dealloying of a gold-silver foil in nitric acid, produced a larger CO partial current density than a pristine nanoporous gold electrode, with -20 mA cm⁻² and -7 mA cm⁻², respectively^[8]. Seemingly, oxide-derived gold particles, obtained by pulse anodization of a pure gold electrode, achieved nearly full CO selectivity (>96%) at low overpotentials (-0.35 V), where the polycrystalline electrode was inactive towards the CO₂RR under these conditions^[6]. Electrokinetic studies indicated that the CO₂RR was limited by the first electron transfer to CO₂ on polycrystalline gold electrode, while the subsequent proton transfer was the rate determining step for oxide-derived gold particles. Kanan *et al.*^[9] observed a similar catalytic behavior for oxide-derived copper electrodes, obtained *via* thermal annealing of copper foils. The selectivity towards CO increased (up to 40% at -0.5 V) with increasing thickness of the surface oxide layer (Cu₂O – before cathodic condition were applied), tuned by changing the

annealing temperature. Another study demonstrated that the maximum in ethylene and ethanol faradaic efficiency (34% and 16% at -0.99 V, respectively) was achieved by a catalyst with $3.6\text{ }\mu\text{m}$ galvanostatically deposited Cu_2O layer (pre-catalysis) and subsequently reduced to Cu^0 , while the pure copper electrode only generated 13% and 0% faradaic efficiencies at the same potentials^[10].

Commonly, plasma treatments, thermal annealing in air or anodic pulses are used to modify silver electrodes, which are subsequently reduced electrochemically. Oxide-derived silver electrodes outperform pristine silver by increasing CO production and suppressing hydrogen evolution. For instance, electrochemical oxidation (by pulse anodization) of a polycrystalline bulk silver electrode led to a large increase in CO selectivity, up to 75% at only -0.6 V, although it has to be noted that the pristine electrode showed a very poor selectivity (less than 5%) at the same potential^[11]. The same strategy was applied on nanostructured materials, such as nanoparticles^[12]. The origin of the improved performance for oxide-derived silver electrodes is still under debate. Using grazing angle EXAFS^[13], the enhanced CO selectivity was correlated to the presence of sub-surface oxygen atoms after the reduction step, and it was postulated that this led to a higher stability of $^*\text{COO}^-$ reaction intermediate compared to the pure silver surfaces. Other groups ascribed the change in selectivity to change in local pH, influenced by the increased surface roughness and porosity compared to flat silver foils^[11], or to the low coordination number of silver atoms at the surface of oxide-derived materials, after stripping of the oxygen atoms^[14].

After exploring the electrocatalytic properties of silver nanoparticles both in chapter 3 and 4, in this chapter we discuss already CO selective silver nanowires and whether electrochemical oxidation can further enhance their catalytic properties. The oxidation state of silver nanowires was controlled and quantified and the change in morphology as a function of the oxidation potential was systematically followed. Finally, the change in morphology was correlated with the oxidation degree to the enhanced catalytic performance of the oxide-derived silver nanowires, leading to remarkably high selectivity towards CO compared to the pristine nanowires.

5.2 Experimental section

5.2.1 Synthesis of pristine silver nanowires

The pristine silver nanowires were synthesized *via* the polyol method^[15]. The glassware (a 25 mL three-neck flask) was cleaned with concentrated nitric acid (65.0% wt/wt) for 1 hour. 0.34 g of poly(vinyl)-pyrrolidone (PVP; 40 000 mol wt; Sigma Aldrich) was dissolved in 20 mL of ethylene glycol (EG; > 99.0%; Sigma Aldrich) and heated to 160 °C under stirring. After complete dissolution of the PVP, 25 mg of freshly prepared AgCl was added to the solution. At 160 °C and in the presence of oxygen, ethylene glycol was partially oxidized to glycol aldehyde, which acted as reducing agent for Ag^+ to Ag^0 ^[16]. The Cl^- enabled the selective oxidative etching of the polycrystalline silver seeds, preserving the (100) and (111) crystal planes (decahedral seeds). After three minutes, 110 mg of AgNO_3 (99.0%; Sigma Aldrich) was added to the flask, allowing the uniaxial elongation of the silver nanowires. After 24 minutes, the reaction mixture was cooled down to room temperature.

The suspension was centrifuged three times at 6000 rpm for 30 minutes in methanol (> 99.9%; Sigma Aldrich), and the solvent was decanted to remove impurities. Finally, the precipitate was dispersed in methanol and stored in the dark, in a vial sealed with Teflon tape to avoid solvent evaporation. A fraction of the as-synthesized silver nanowires was drop casted on top of a carbon paper electrode (sample name: pristine), while part of the batch was subjected to the oxidation/reduction procedure (sample name: oxY_(0.15-Z), where Y = 1, 2 or 3, with 1 indicating the least oxidized sample, and 3 the most oxidized sample; Z represents the final oxidation potential). For instance ox1_(0.15-0.5) stands for OD-nanowires oxidized by applying a potential sweep between +0.15 V and +0.5 V vs Ag/AgCl.

5.2.2 Synthesis of fresh AgCl

Silver chloride (AgCl) is a photosensitive compound. Therefore, the use of freshly made silver chloride for the synthesis of silver nanowires is necessary to avoid the formation of metallic silver by photoreduction of silver chloride in stock batches. The synthesis of AgCl was performed in a vial wrapped in aluminum foil, to avoid direct contact with light, *via* a one-step procedure. A 0.5 M solution of silver nitrate was mixed with a 1 M solution of sodium chloride,

while stirring at 500 rpm for 5 minutes. After the addition of sodium chloride, silver chloride flocculates immediately. The precipitate was separated from the supernatant, washed once with ultrapure water and dried under vacuum.

5.2.3 Synthesis of oxide-derived silver nanowires

To oxidize and reduce the silver nanowires, we used a custom-made oxidation-reduction holder (figure 5.1 a-c). After drop casting $0.3 \text{ mg}_{\text{Ag}} \text{ cm}^{-2}$ onto a carbon paper substrate, we placed the carbon cloth on top of a glassy carbon disc, in contact with a copper wire connected to the external electric circuit. The holder allows to protect one side of the carbon paper, and at the same time guarantees optimal electrical contact between the catalyst and the electrical source. To oxidize in a controlled fashion the silver electrodes, we chose linear sweep voltammetry (LSV, scan rate = 10 mV s^{-1}) performed in 0.2 M NaOH (pH = 13) in a beaker, using a three-electrode configuration, with Ag/AgCl as reference and a Pt wire as counter electrode. The reduction of the oxidized electrode was performed *via* LSV (scan rate = 10 mV s^{-1}) in 0.1 M KHCO_3 in a beaker, prior to starting the catalytic tests, to avoid perturbations during the CO_2RR .

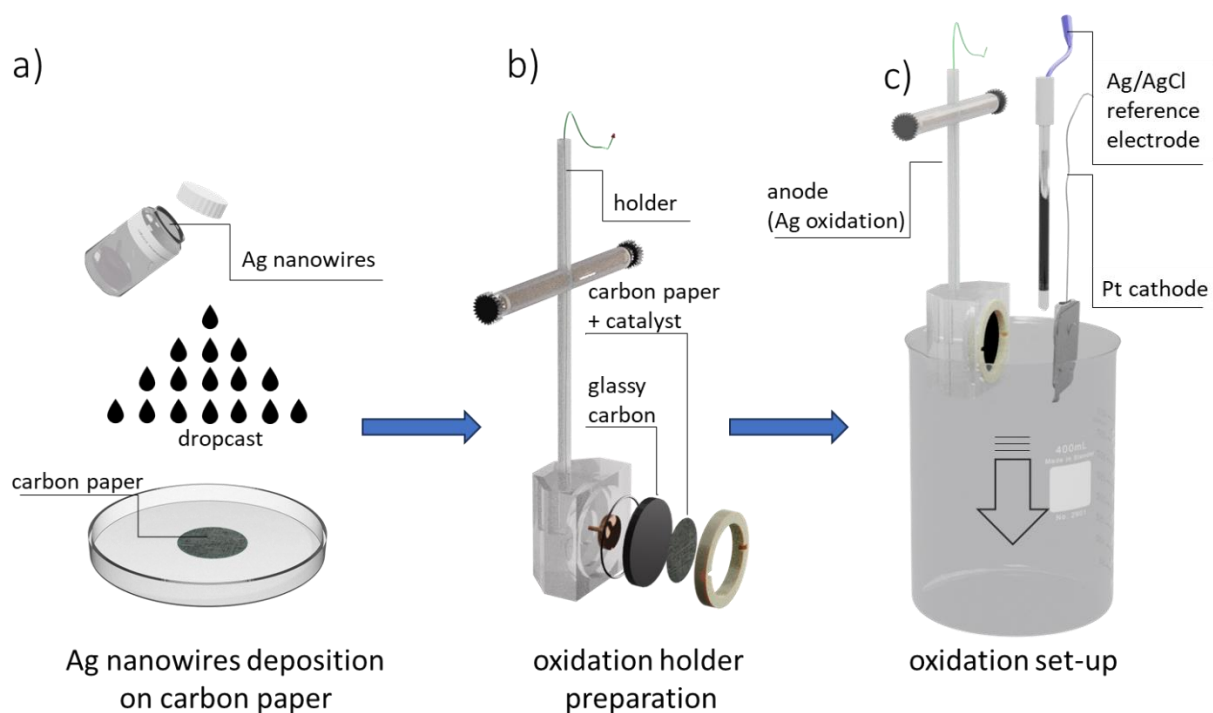


Figure 5.1 – Schematic representation of the silver nanowire oxidation set-up, realized with the help of Sander Deelen. a) silver nanowire deposition on the carbon paper. b) different components of the oxidation holder. c) oxidation set-up with Ag/AgCl reference electrode and platinum counter electrode.

5.2.4 Characterization

Transmission electron microscopy (TEM) images of the pristine nanowires were acquired using a Thermo Fischer Scientific Tecnai20 microscope, operated at 200 kV. The holey carbon 200 mesh copper grids were prepared by drop casting the silver nanowires colloidal solution directly on the grid and dried at room temperature. The silver nanowires average diameter and length was determined by analyzing 10 different TEM images and around 97 nanowires. The average diameter (or length) was calculated using equation 3.1 (chapter 3). Scanning electron microscopy (SEM) images were acquired on a FEI PhenomProX from Phenomworld at 10 kV, imaging using the backscatter detector. High resolution SEM images were acquired using a FEI Helios G3 UC microscope, operated at 10 kV. Sticky carbon tape was used to attach the electrodes on the sample holder.

X-ray diffraction measurements were performed on a Bruker D2 Phaser, equipped with a Co K α X-ray source with a wavelength of 1.79026 Å. Rietveld refinement analysis was performed using MAUD software, considering R_{wp} and χ^2 as indicators for the quality of the fitting^[17]. The XPS data were collected at TU Eindhoven by using ThermoFischer Thermo Scientific K-Alpha X-ray Photoelectron Spectrometer System, with an Al source (K α monochromatic radiation, 1486.6 eV). The deconvolution and quantification of the silver peaks was achieved using CasaXPS and Origin. The carbon peak at 284.84 eV was used as a calibration for energy. UV-vis measurements were performed on Agilent Technologies Cary 60 UV-Vis, and they were used to monitor the purity of the silver nanowires during the synthesis.

To determine the silver metal weight loading on the carbon paper support, the concentration of silver in the colloidal solution was measured by Inductively Coupled Plasma (ICP) on PerkinElmer Optima 8300 Optical Emission Spectrometer. The precise amount of silver was deposited on the carbon paper by using a Finn pipet. The silver loss during the oxidation and reduction procedure was quantified by atomic absorption spectroscopy on a ContrAA 700 AAS instrument. The electrochemical surface area measurements were performed using the underpotential lead deposition method in 0.01 M Pb(NO₃)₂ (99.9%; Sigma Aldrich) + 0.01 M HNO₃ (65.0% wt/wt; Sigma Aldrich), assuming $1.67 \times 10^{-3} \text{ cm}^2 \mu\text{C}^{-1}$ and a scan rate of 10 mV s^{-1} ^[18].

5.2.5 Electrochemical measurements

A three-electrode custom-built H-type electrochemical cell, made of polymethylmethacrylate, was used for electrocatalytic experiments (figure 1.3). The cathodic and anodic compartments (electrolyte volume = 15 mL each; headspace volume = 3 mL each) were divided by a Nafion 117 membrane (Ion Power). The CO₂ saturated catholyte was purged with 20 mL min^{-1} CO₂ (Linde, purity 5.2), while the anolyte was stirred by bubbling Ar (20 mL min^{-1}). The working electrode was composed of a glassy carbon disc (HTW-Germany), in contact with the carbon paper disc (TGP-H-060, Toray) on top of which we deposited the silver nanowires. Onto the carbon paper (total electrode area = 4.9 cm^2) the silver nanowires colloidal suspension was drop cast and dried overnight at room temperature. A silver weight loading of $0.3 \text{ mg}_{\text{Ag}} \text{ cm}^{-2}$ was used for the pristine nanowires electrode, as determined by measuring the silver content *via* ICP. The carbon paper surface area in contact with the

potassium bicarbonate (>99.0%; Sigma Aldrich) electrolyte (0.1 M; pH = 6.8) was 3.8 cm². We used an Ag/AgCl (3 M KCl) reference electrode (Metrohm) and a 3.8 cm² Pt disc (99.5%; Goodfellow) as counter electrode. The electrochemical measurements were performed using a Parstat MultiChannel potentiostat/galvanostat, with a MultiChannel -1000 AC/DC channel for electrochemical impedance measurements.

The electrocatalytic activity was measured both with chronoamperometry and with cyclic voltammetry, corrected for the uncompensated potential measured by impedance spectroscopy (electrolyte resistance). The results were confirmed by chronoamperometry measurements at different potentials for 30 minutes. The gaseous products were analysed online by gas chromatography, using Global Analysis Solutions Microcompact GC 4.0 machine from InterScience, already described in a previous work^[19].

Nuclear magnetic resonance spectra of liquid products were taken at 298 K on a Varian MRF400 spectrometer. Only traces of formate were detected in the liquid phase, therefore mainly CO and H₂ contributed to the selectivity of the process. The selectivity of the process was defined by the Faradaic efficiency (FE), calculated using equation 2.2 (chapter 2). The partial current density defines the individual contribution of the reaction products to the total current density. This parameter was calculated as the product of the total current density and the FE. The impedance measurements were performed on the Parstat MultiChannel -1000 channel of PARSTAT potentiostat, using a frequency range from 0.1 Hz to 100 kHz. The impedance measurements for the charge transfer resistance quantification were performed at the indicated potentials, right after the chronoamperometry measurement at the same potential. Before fitting the Nyquist plots with the equivalent circuit described later, we performed a Kramers-Kronig test on the raw data. Impedance data were analyzed *via* EQC software^[20], following the data validation described in another work^[21]. All fits performed resulted in $\chi^2 < 10^{-3}$.

5.3 Results and Discussion

5.3.1 Synthesis and characterization of oxide-derived silver nanowires

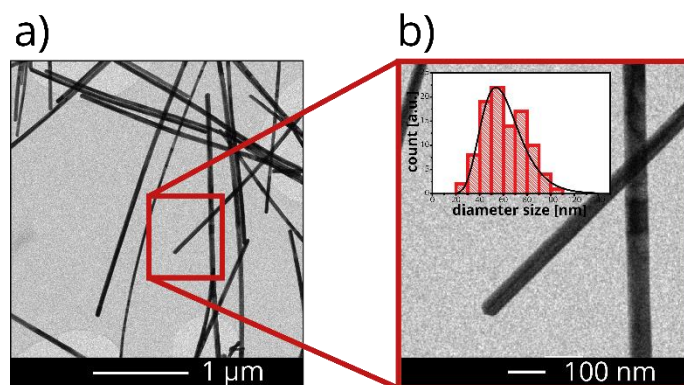


Figure 5.2 – a) Transmission electron micrographs of silver nanowires synthesized *via* the polyol method, b) high magnification of two nanowires. The inset in figure 5.2b shows the shows a higher magnification.

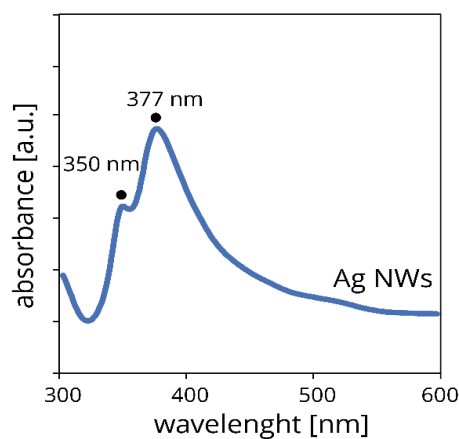


Figure 5.3 – UV-vis spectrum of as-synthesized silver nanowires.

Figure 5.2a shows transmission electron microscopy (TEM) images of nanowires synthesized *via* the polyol method. The average diameter of the wires was 61 ± 17 nm (inset, figure 5.2b) and the average length was $10 \mu\text{m}$, leading to an aspect ratio of around 160. The

epitaxial growth of the nanowires is due to the strong poly(vinyl)-pyrrolidone adsorption preferentially on the (100) facets of the silver seeds^{[22][23]}, which directs the addition of silver atoms onto the uncapped (111) facets, generating 1-D nanostructures. Figure 5.2b shows the faceting at the tip of the nanowires, formed by the intersection between the (100) plane and the (111) plane. The formation of the nanowires was qualitatively followed *via* UV-vis measurements. Two absorption bands are observed at 350 nm and 377 nm, corresponding to the wire's surface plasmon resonance absorption bands (figure 5.3)^[15]. The pristine nanowires were used as a starting point to study the influence of different oxidation treatments on the oxidation state, morphology, and catalytic performance of the silver nanowires.

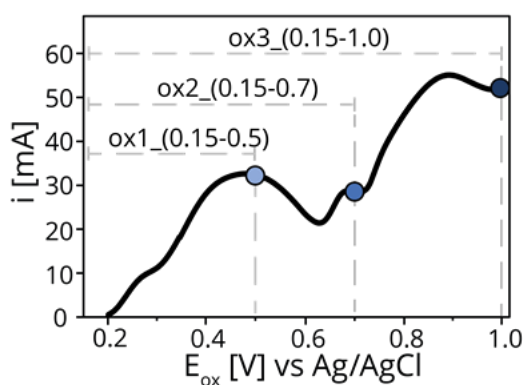


Figure 5.4 – Current versus voltage curves measured in 0.2 M NaOH at 10 mV s^{-1} showing an anodic current due to the electrochemical oxidation of the silver nanowires.

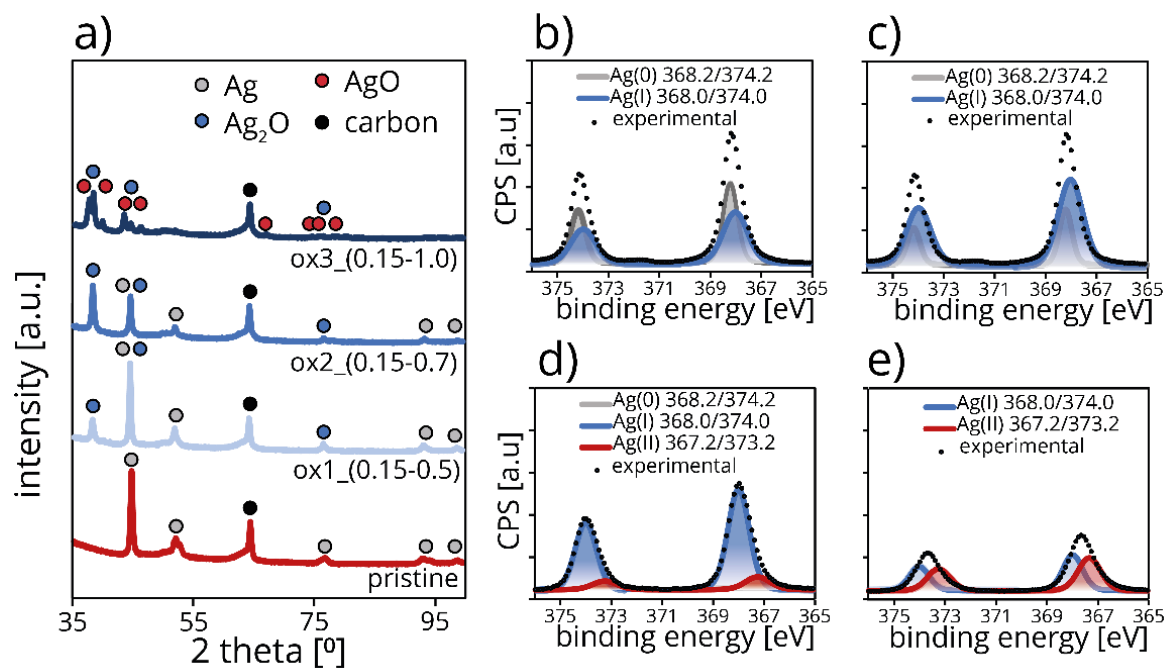


Figure 5.5 – a) XRD pattern of pristine (red), ox1_(0.15-0.5) (light blue), ox2_(0.15-0.7) (blue) and ox3_(0.15-1.0) (dark blue) samples. XPS spectra of b) pristine, c) ox1_(0.15-0.5), d) ox2_(0.15-0.7) and d) ox3_(0.15-1.0) nanowires.

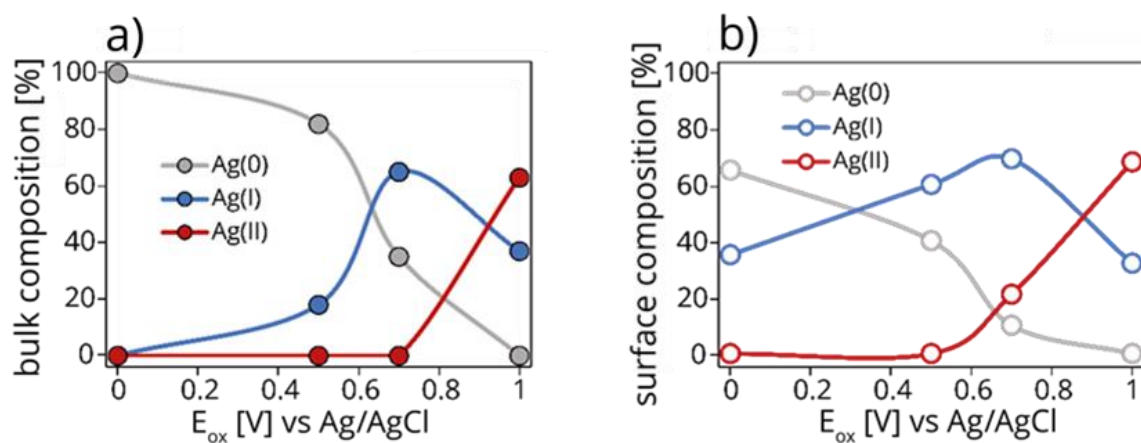
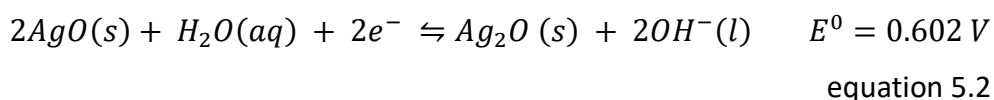
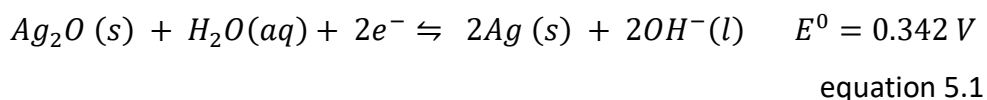


Figure 5.6 - The composition of the different silver oxidation states was quantified a) by XRD and b) by XPS, for pristine, ox1, ox2 and ox3 catalysts. The samples were analyzed after the oxidation treatment. This image offers a direct comparison between bulk (XRD) and surface (XPS) oxidation state.

Figure 5.4 displays the current evolution as a function of the applied anodic potential, obtained *via* linear sweep voltammetry performed in 0.2 M NaOH at 10 mV s⁻¹. Two main peaks were detected: the first peak, ranging from +0.2 V to +0.63 V, is assigned to the oxidation of silver to silver (I) oxide (equation 5.1), while the second peak, centered at +0.9 V, is attributed to further oxidation of silver(I) oxide to silver (II) oxide (equation 5.2):



This electrochemical procedure allowed control over the oxidation degree of the nanowires, by setting a maximum oxidation potential, producing three different catalysts: ox1_(0.15-0.5) partially oxidized to Ag₂O, ox2_(0.15-0.7) with extensive oxidation to Ag₂O, and ox3_(0.15-1.0) almost completely oxidized to AgO, as indicated by the blue dots in Figure 5.4.

After the oxidation treatment, we ex-situ characterized the oxidation state of the silver nanowires with XRD (bulk analysis) and XPS (surface analysis). Quantitative Rietveld refinement analysis of the XRD raw data (figure 5.5a and 5.6a) revealed that, starting from completely metallic silver in the pristine nanowires (0 V oxidation potential), about 18% (wt/wt) of the silver was in the form of Ag₂O after oxidation up to 0.5 V. By further oxidation up to 0.7 V, the percentage of Ag₂O increased to 65%. Extending to the most positive oxidation potential (1.0 V vs Ag/AgCl), the nanowires consisted of 66% AgO and 34% Ag₂O, while no metallic silver was left. Figure 5.6b shows the XPS analysis derived from the deconvolution of the two silver peaks, generated by the spin orbit splitting of the 3d electrons (figure 5.5 b-e)^[24]. The surface analysis (approximately 2 nm) demonstrated that the pristine silver nanowires had a passivation surface layer (due to the exposure to air) that was not detected by the XRD measurement. The ox1_(0.15-0.5) catalyst surface consisted of about 60% Ag₂O and 40% metallic silver, while ox2_(0.15-0.7) contained 20% (wt/wt) AgO, not detected in the XRD measurement. Finally, ox3_(0.15-1.0) showed only AgO and Ag₂O.

A comparison between the bulk (figure 5.6a) and surface composition (figure 5.6b) demonstrates that, although both analyses show a similar trend, the percentage of oxide at the surface was larger than in the bulk. This is logical as oxidation took place at the interface between the nanowires and the basic electrolyte, where the oxygen was introduced into the silver crystal lattice. By increasing the bias, subsurface layers started to get oxidized, and the oxidation process penetrated towards the core of the nanowires^{[25][26]}. All samples, after oxidation treatment, were reduced by scanning from 0.15 V to -1.0 V vs Ag/AgCl in 0.1 M KHCO_3 with 10 mV s^{-1} . This led to a reduction to metallic silver, and these samples from now on are denoted as oxide-derived (OD-) Ag nanowires.

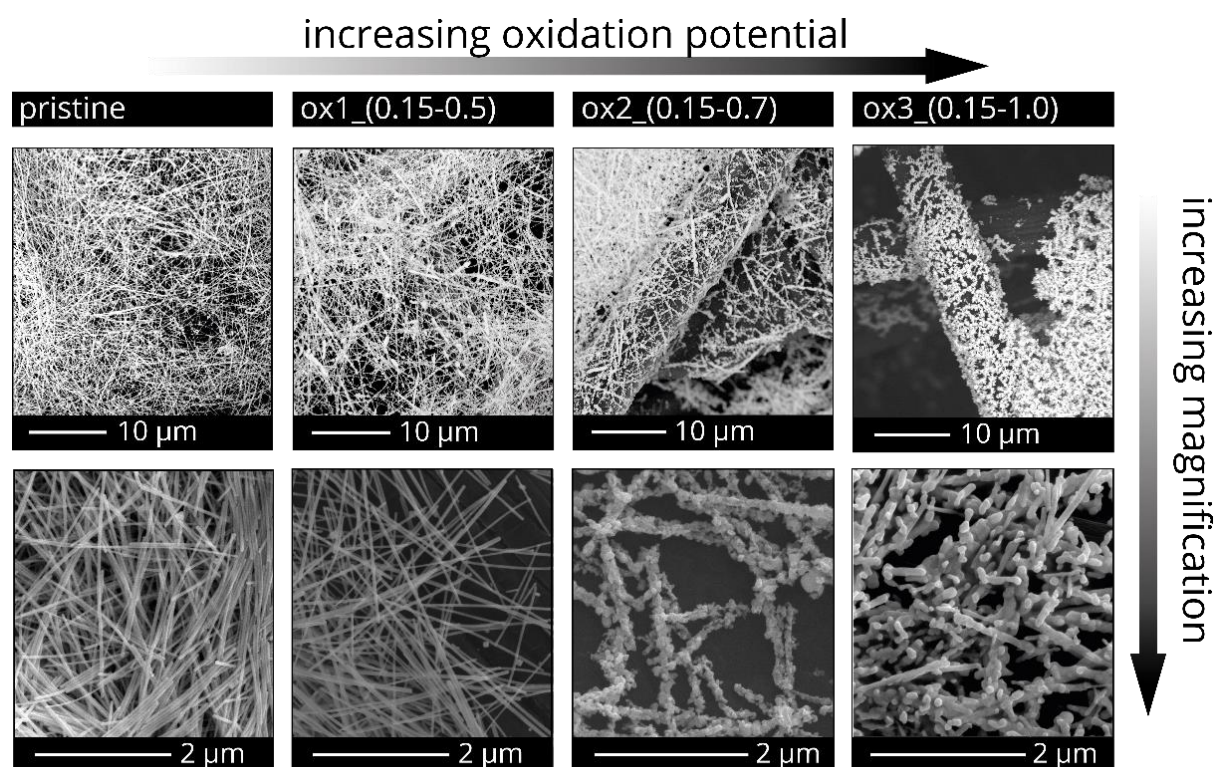


Figure 5.7 – Scanning electron micrographs (SEM) of silver nanowires both pristine (left) and OD-nanowires after exposure to different oxidation potentials followed by reduction at -1.0 V (right). The top row shows the dispersion of nanowires on the carbon paper (low magnification). The bottom row shows the morphology of the nanowires in more detail (high magnification).

The morphology of the pristine and OD-nanowires was studied by scanning electron microscopy (SEM). Figure 5.7 shows representative images, acquired both at lower magnification (top row) and higher magnification (bottom row) to analyze the morphology at nanoscale. The low magnification images show that after oxidation and reduction treatment the remaining nanowires were located close to the ca. 10 μm diameter carbon paper fibers. By increasing the oxidation potential, the underlying nanowire architecture is preserved, but the shape of the nanowires becomes more irregular, illustrated by the ox2_(0.15-0.7) sample. By further increasing the oxidation potential to 1.0 V, the features became less sharp and defined, though still resembling the original nanowires morphology. Furthermore, while the density of nanowires on the carbon paper decreased upon oxidation, the thickness of the nanostructure increased.

5.3.2 Electrocatalytic activity and selectivity

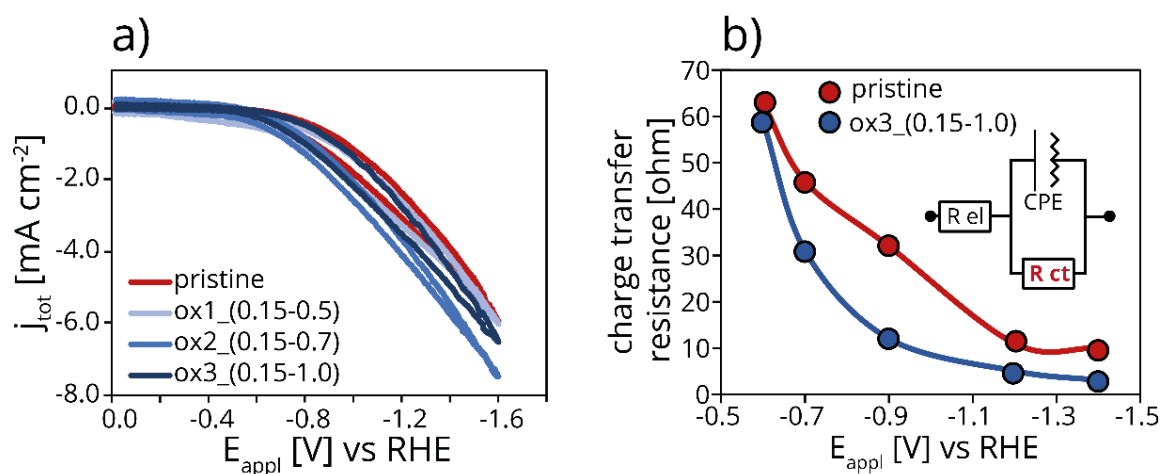


Figure 5.8 – a) Total current density j_{tot} produced by the pristine and the oxide derived nanowires as a function of the applied potential E_{appl} , corrected for the electrolyte resistance. The measurement was performed in 0.1 M KHCO_3 with 10 mV s^{-1} scan rate. b) Charge transfer resistance as a function of the applied potential, measured by impedance spectroscopy in the range between 100 kHz and 1 Hz. The inset shows the equivalent circuit used to fit the impedance data (R_{el} = electrolyte resistance; CPE = constant phase element; R_{ct} = charge transfer resistance).

The electrocatalytic performance of the oxide-derived (OD)-nanowires was compared with that of the pristine catalyst. Figure 5.8a displays the electrochemical current density of the during cycling performed in 0.1 M KHCO_3 . All the OD-catalysts produced a slightly larger current density than the pristine nanowires when normalized per geometric surface area. ox2(0.15-0.7) produced the largest current density, possibly due to its high surface roughness. The OD-catalyst had a lower onset potential than the pristine nanowires.

Impedance spectra were recorded for the pristine and ox3_(0.15-1.0) samples at each potential, to assess the difference in charge transfer resistance between the as-synthesized and most oxidized catalysts (figure 5.8b). The inset in figure 5.8b, shows the equivalent circuit used to fit the impedance raw data, corresponding to a simple resistance-constant phase element-resistance circuit (Randles circuit^[27]). R_{el} is the electrolyte resistance, while R_{ct} is the charge transfer resistance, which corresponds to the intrinsic resistance to the electron transfer occurring at the interface of the catalyst. The OD-catalyst showed a lower charge transfer resistance than the pristine sample through the entire potential range. The difference between the two electrodes is small at low potentials (-0.6 V), where they both showed a relatively small current density and a large resistance, with 63 ohm and 59 ohm for pristine and oxidized sample respectively. At larger potentials (-0.9 V and -1.4 V), the difference was larger, with the pristine nanowires displaying a 2.7-times larger resistance compared to the OD-sample. These results suggest that the defective surface of OD-silver catalysts was electrochemically more active than the pristine wires and promoted the electron transfer to either CO_2 or $\text{H}_2\text{O}/\text{H}^+$.

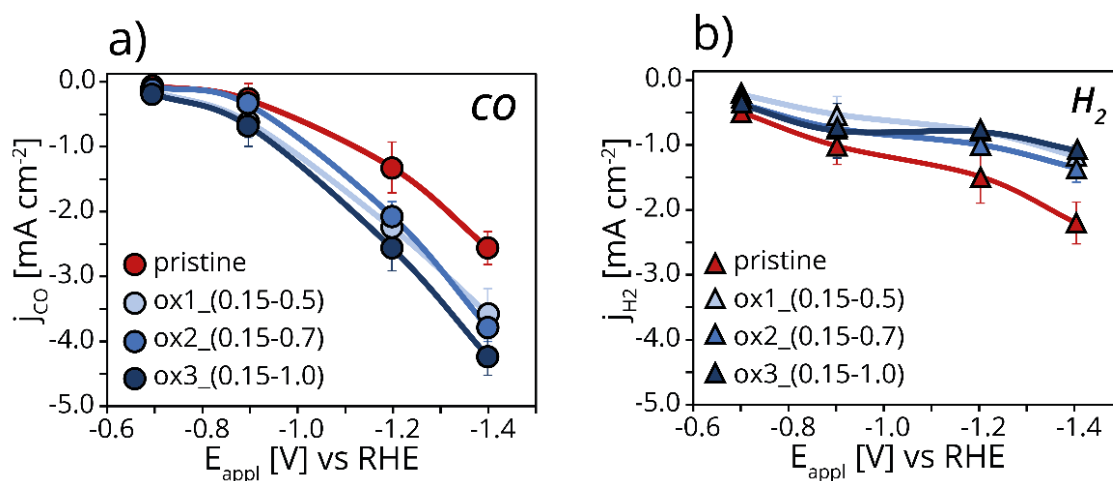


Figure 5.9 – a) CO and b) H₂ partial current density, normalized per geometric surface area, as a function of the applied potential. The test was performed in 0.1 M KHCO₃ with online measurements of the gaseous products (average over 30 minutes catalysis at each potential).

To evaluate the selectivity of the process and separate the individual contributions of the different products to the total current density, the geometric partial current densities were calculated for both pristine and OD-catalysts. This analysis was based on chronoamperometry measurements, coupled with GC analysis of the reaction products. CO was the only product formed from CO₂ while H₂, formed both over carbon and silver, is the competitive product. Figure 5.9a clearly demonstrates that the OD-nanowires were more selective towards CO than the pristine nanowires. The ox3_(0.15-1.0) sample produced a nearly 2-fold higher CO partial current density than the pristine sample, both at -1.2 V and -1.4 V. The pristine catalyst generated the largest H₂ partial current density. The OD-materials produced about half the amount of H₂, with no clear difference between the different OD-materials (figure 5.9b). Hence, the oxidation treatment promoted the conversion of CO₂ to CO and suppressed the H₂ evolution, enhancing the selectivity of the process.

5.3.3 Understanding the selectivity of oxide-derived silver nanowires

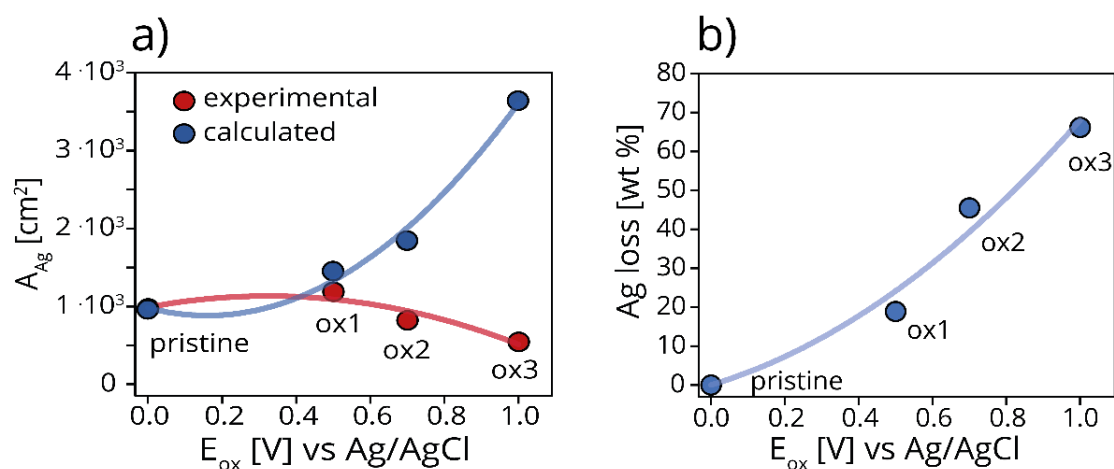


Figure 5.10 – a) Electrochemically active silver surface area (A_{Ag}) measured by under potential lead deposition (experimental, red markers) and calculated for the theoretical situation of no silver loss (calculated, blue markers). b) silver loss as a function of the applied oxidation potential, measured by atomic absorption spectroscopy.

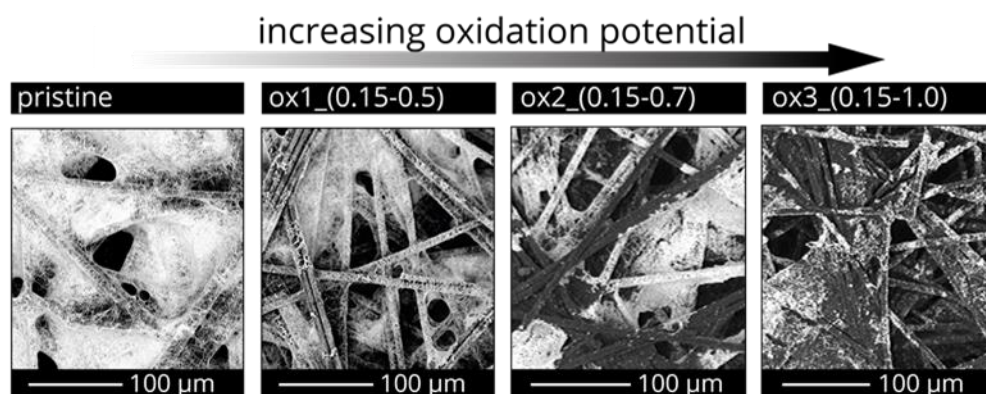


Figure 5.11 – Low magnification SEM images of the carbon supported silver nanowires catalysts.

To assess the key parameters influencing the selectivity of the process, the surface area-normalized selectivity of the catalysts was determined (figure 5.10a). The silver surface was measured by underpotential Pb deposition. In the current-voltage scan, two main peaks were observed, with the first due to underpotential deposition (onset = +0.1 V vs Ag/AgCl) and the second to bulk Pb deposition (onset = -0.2 V vs Ag/AgCl). The silver surface area slightly

increased after oxidation to 0.5 V (ox1_(0.15-0.5) sample), but a 16% and 44% decrease in active surface area was measured for ox2_(0.15-0.7) and ox3_(0.15-1.0) respectively, compared to the pristine nanowires (figure 5.10a, red markers).

SEM already suggested that the density of silver was lower, but also showed an increased surface roughness (figure 5.7) with increasing oxidation potential. Elemental analysis (figure 5.10b) showed that ox3_(0.15-1.0) sample contained 66% less silver than the pristine sample. This points to the dissolution of silver oxide in the aqueous electrolyte, which results in loss of active metal and perhaps enhanced by bubble formation, possibly also some detachment of silver wires. This hypothesis is supported by previous studies, highlighting the solubility at room temperature of Ag_2O in alkaline electrolytes (forming soluble $[\text{Ag}(\text{OH})_2]^-$)^{[28][29][30]}. Furthermore, the cathodic charge, obtained after the reduction of the catalysts, was lower than the anodic charge, obtained after the oxidation treatment. The low magnification SEM overview images of the electrodes (figure 5.11), indeed show that the silver coverage (white areas) of the carbon substrate (dark areas) decreased by increasing the oxidation potential. Therefore, upon oxidation the nanowires experienced two phenomena: (I) an increase in surface roughness leading to increased surface area and (II) a loss of active metal, decreasing the metal surface area. If we could prevent silver leaching during the oxidation treatment, the theoretical silver surface area would increase almost exponentially with increasing oxidation potential, based on the surface roughness increase (figure 5.10 a, blue markers).

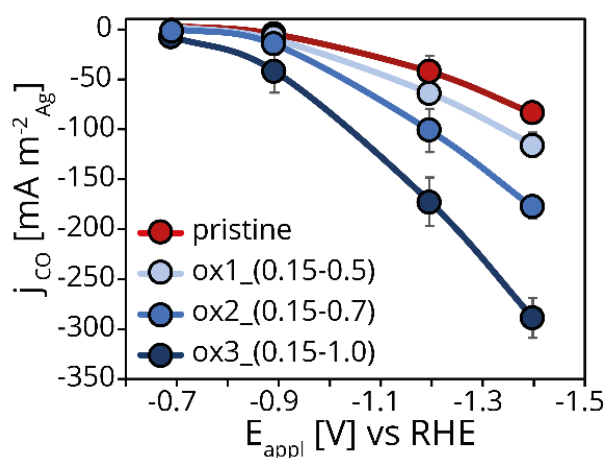


Figure 5.12 – CO partial current density, normalized by silver electrochemically active surface area, as a function of the applied potential.

Figure 5.12 shows the specific CO partial current density of pristine (red markers) and oxidized (blue markers) as a function of the applied potential per real Ag surface area. The pristine nanowires presented the smallest specific CO current density, with only $-47.7 \text{ mA mAg}^{-2}$ at -1.2 V , while ox1(0.15-0.5) and ox2_(0.15-0.7) produced $-69.2 \text{ mA mAg}^{-2}$ and $-106.5 \text{ mA mAg}^{-2}$ at the same potential. The highest CO production density per silver area was obtained with ox3_(0.15-1.0) sample, generating a 3.7-fold increase in the CO specific current density ($-178.0 \text{ mA mAg}^{-2}$) compared to the pristine nanowires. A similar trend was observed at -1.4 V , with ox3_(0.15-1.0) generating $-294.2 \text{ mA mAg}^{-2}$ and outperforming the ox2_(0.15-0.7), ox1_(0.15-0.5) and pristine catalysts, which produced only $-183.6 \text{ mA mAg}^{-2}$, $-120.8 \text{ mA mAg}^{-2}$, and $-89.4 \text{ mA mAg}^{-2}$, respectively. These catalytic data demonstrates that the oxidation process significantly steered the intrinsic selectivity of the catalysts towards CO. The enhancement in specific CO partial current density reflects an improved intrinsic selectivity of the catalysts, as it does not depend on the active metal surface area.

To better understand the selectivity enhancement, we analyzed the rate determining step of the process, to determine if the change in selectivity is related to a change in the reaction pathway. We selected the pristine and the ox3_(0.15-1.0) samples for this analysis, as they showed the largest difference in selectivity.

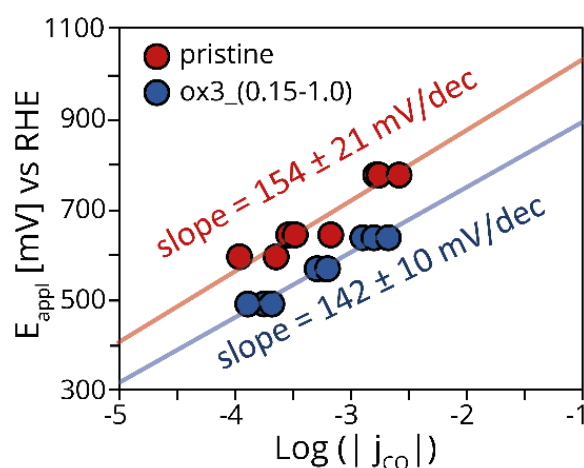


Figure 5.13 – Tafel plot related to CO formation, measured during chronoamperometry, for both the pristine (red marker) and ox3_(0.15-1.0) samples. The error on the slope is calculated using 95% confidence level.

The slope of the Tafel plot gives information about the nature of the rate-determining step of an electrochemical reaction. For the CO₂RR, the Tafel slope is 118 mV/dec if the formation of *COO⁻ intermediate is rate limiting, due to a slow first electron transfer to CO₂. On the contrary, the Tafel slope is 59 mV/dec if the first electron transfer is fast and not limiting the reaction. This hypothesis is valid if it is assumed that the first electron transfer to CO₂ precedes the proton transfer to *COO⁻ first reaction intermediate (uncoupled electron and proton transfer mechanism)^{[31][6]}. The pristine (red markers) and ox3_(0.15-1.0) (blue markers) sample gave a Tafel slope of 154 ± 21 mV/dec and 142 ± 10 mV/dec respectively (figure 5.13). Although the experimental values are higher than the theoretical value, possibly due to a slight influence of mass transfer limitations, the rather high and similar values of the Tafel slope suggest that the rate determining step for both catalysts is the first electron transfer to CO₂.

5.3.4 Electrocatalytic stability

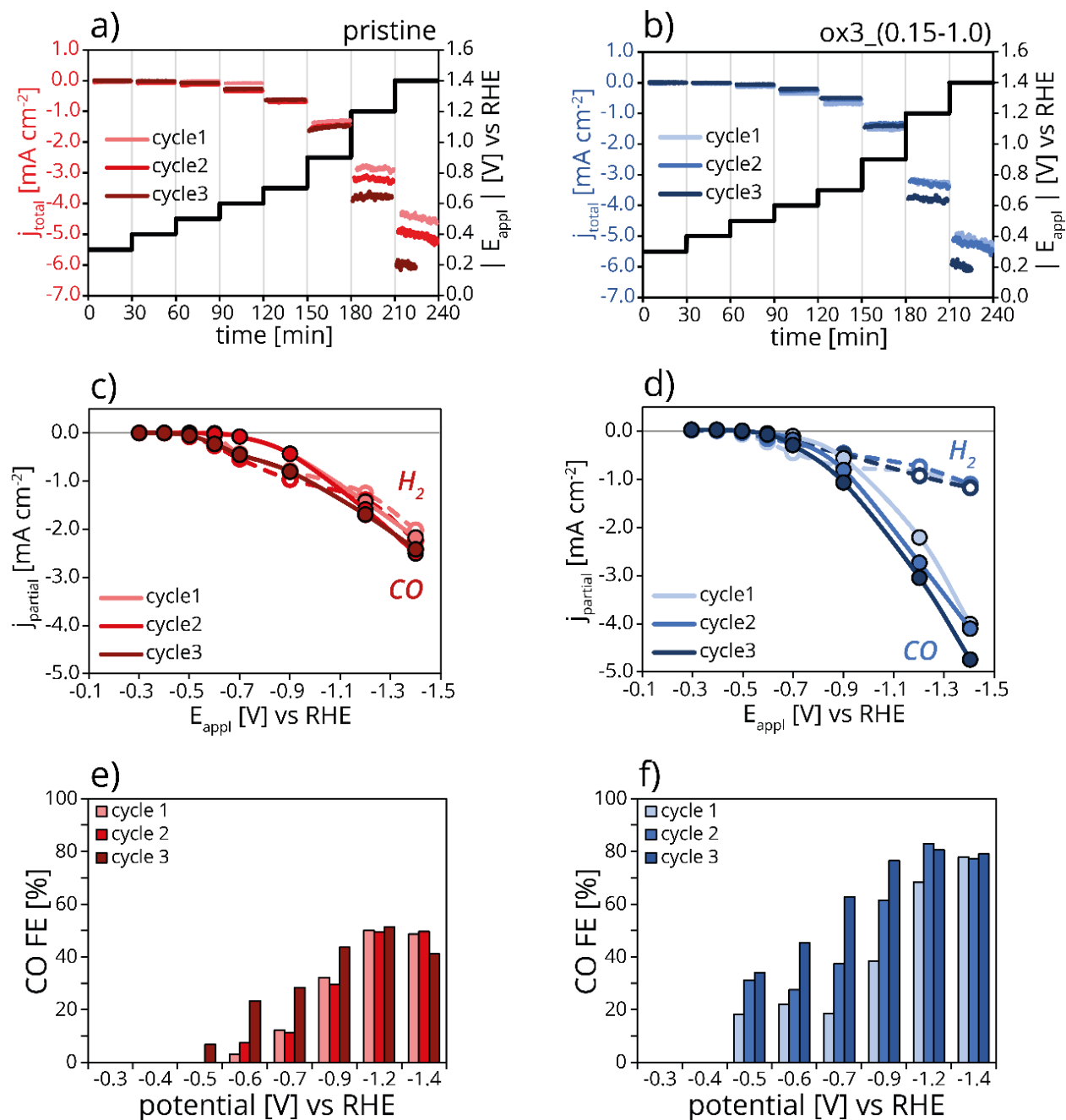


Figure 5.14 – Chronoamperometry stability test performed over three cycles, for both a) pristine and b) ox3_(0.15-1.0) samples. CO (full marker) and H₂ (empty marker) geometric partial current density as a function of the applied potential over three potential cycles (chronoamperometry, hold time = 30 min per potential) for both c) pristine and d) ox3_(0.15-1.0) samples. e) pristine and f) ox3_(0.15-1.0) catalysts' CO faradaic efficiency measured during the stability test.

As the catalysts' stability over time is a key factor for future application of electrocatalytic materials, we also investigated the stability of the catalysts by repeating three times a cycle of eight different potentials for a total of 12 hours. Figure 5.14a and b show the total geometric current density and the stability test potentials as a function of time for pristine and ox3_(0.15-1.0), respectively. At the three lowest potentials (i.e. -0.3 V, -0.4 V and -0.5 V), neither of the catalysts generated gaseous products above the GC detection limit (5 ppm for both H₂ and CO). From -0.7 V downwards, both catalysts showed an increasingly larger current density and product formation. Both pristine and OD-nanowires showed stable and reproducible current densities at low overpotentials, until -1.2 V. At larger overpotential (-1.4 V), for both ox3_(0.15-1.0) and pristine samples the current density gradually increased with time.

The partial current densities (figure 5.14 c-d) were rather stable over three cycles, as well as the CO Faradaic efficiencies (figure 5.14 e-f). A small increase over cycles both in CO and H₂ partial current was measured for both pristine (figure 5.14c) and ox3_(0.15-1.0) (figure 5.14d) catalysts. These inspiring catalytic results from the Ag nanowires open the possibility for further studies on more industrially oriented set ups and devices such as in gas diffusion electrodes and flow cells.

These results clearly showed that the oxidation treatment on silver nanowires remarkably boosted the catalytic performance of the silver catalysts. Furthermore, it is evident that the harsher the oxidation treatment, the larger the CO partial current density per unit of silver area. The electrokinetic analysis (Tafel plot) suggested that no significant change in the reaction pathway or rate determining step occurred after oxidation. Nevertheless, the dramatic enhancement in selectivity for the oxide-derived nanowires points to the formation of new and more selective active sites for CO₂RR. It is likely that subsurface oxygen, stable during catalysis but difficult to detect even with surface techniques, promoted the reduction of CO₂ to CO by helping the stabilization of the first reaction intermediate (*COO⁻), as previously suggested by the group of Smith^[13]. Another possible explanation for the change in selectivity implies that the local pH, at the surface of the oxide-derived samples, is higher than the pH at the surface of pristine nanowires, due to the high surface roughness deriving from the oxidation treatment. High surface roughness limits the diffusion of the buffer

electrolyte to the surface of the electrocatalyst, thus affecting the neutralization/back diffusion of OH^- deriving from both the HER and CO_2RR , hence affecting the reaction selectivity^{[32][33]}. However, this explanation seems less probable, as a drastic improvement in CO FE (figure 5.14e) and partial current density (figure 5.14c) would have been expected for the pristine nanowires after the first potential cycle during the stability tests, if the local pH would have increased. On the contrary, pristine nanowires seem to behave similarly to ox3_(0.15-1.0) sample over multiple potential cycles, hence suggesting the presence of intrinsically different active sites on the oxide-derived sample.

5.4 Conclusions

In this chapter, we have studied the electrocatalytic properties of oxidized Ag silver nanowires for the CO₂ reduction reaction. Controlled electrochemical oxidation was applied to silver nanowires (aspect ratio = 160), synthesized *via* the polyol method. By carefully selecting the final potential during the oxidation treatment (linear sweep voltammetry), we obtained samples with different compositions, ranging from Ag⁰ in the pristine nanowires to 66% AgO and 34% Ag₂O for ox3_(0.15-1.0), oxidized to 1.0 V vs Ag/AgCl. Furthermore, we systematically followed the evolution of the nanowire morphology after the oxidation and reduction process. Hence, we showed that harsher oxidation conditions (more positive applied potentials) not only generated more roughness, but also contributed to active metal loading loss. Nevertheless, the oxide-derived nanowires greatly outperformed the pristine nanowires, with ox3_(0.15-1.0) producing 3.7-fold increase in Ag surface area-normalized CO current density compared to the as-synthesized electrode. No significant difference in the rate determining step of the reaction emerged from the Tafel plot analysis. It is likely that the improvement in CO selectivity for the oxide-derived nanowires is related to the formation of new active sites (subsurface oxygen species). This work shows that a controlled oxidation treatment can be applied to well defined and CO selective silver nanostructures, and still generate an improvement in the catalytic performance, by further steering the selectivity towards CO.

Acknowledgements

Stephan Jonker is acknowledged for the precious help with atomic absorption spectroscopy measurements. Matteo Parente is acknowledged for the fruitful discussions regarding the synthesis of the pristine silver nanowires. Valerio Gulino acknowledges funding from RELEASE (project number: 17621). Nienke Visser is acknowledged for the TEM images of the pristine nanowires. Matt Peerlings and Maaïke van Ittersum are acknowledged for the useful discussions related to the electrochemical results. Jan Willem de Rijk is acknowledged for the technical support, helping both with the cell design and the preparation of the catalytic

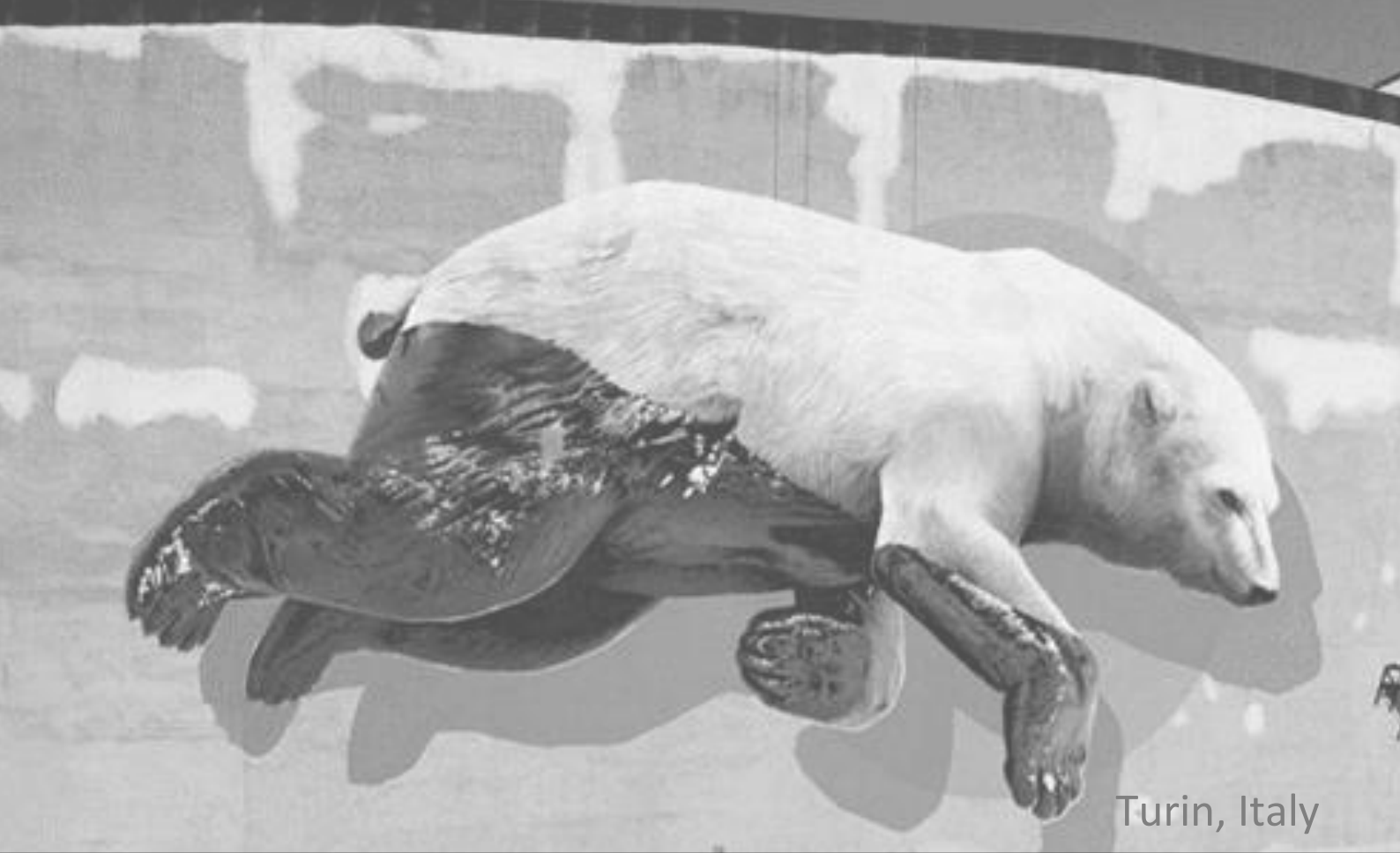
set-up during this project. Sander Deelen is acknowledged for his contribution in the design of the oxidation set-up.

References

- [1] L. Zeng, J. Shi, H. Chen, C. Lin, *Energies* **2021**, *14*, 2840–2850.
- [2] J. Ge, J. Long, Z. Sun, H. Feng, J. Hu, S. W. Koh, Q. Yu, J. Xiao, H. Li, *ACS Appl. Energy Mater.* **2019**, *2*, 6163–6169.
- [3] C. Luan, Y. Shao, Q. Lu, S. Gao, K. Huang, H. Wu, K. Yao, *ACS Appl. Mater. Interfaces* **2018**, *10*, 17950–17956.
- [4] S. Liu, X. Z. Wang, H. Tao, T. Li, Q. Liu, Z. Xu, X. Z. Fu, J. L. Luo, *Nano Energy* **2018**, *45*, 456–462.
- [5] L. Hu, Y. Zhang, W. Han, *New J. Chem.* **2019**, *43*, 3269–3272.
- [6] Y. Chen, C. W. Li, M. W. Kanan, *J. Am. Chem. Soc.* **2012**, *134*, 19969–19972.
- [7] J. J. Velasco-Vélez, C. H. Chuang, D. Gao, Q. Zhu, D. Ivanov, H. S. Jeon, R. Arrigo, R. V. Mom, E. Stotz, H. L. Wu, T. E. Jones, B. Roldan Cuenya, A. Knop-Gericke, R. Schlögl, *ACS Catal.* **2020**, *10*, 11510–11518.
- [8] Z. Qi, J. Biener, M. Biener, *ACS Appl. Energy Mater.* **2019**, *2*, 7717–7721.
- [9] C. W. Li, M. W. Kanan, *J. Am. Chem. Soc.* **2012**, *134*, 7231–7234.
- [10] D. Ren, Y. Deng, A. D. Handoko, C. S. Chen, S. Malkhandi, B. S. Yeo, *ACS Catal.* **2015**, *5*, 2814–2821.
- [11] M. Ma, B. J. Trześniewski, J. Xie, W. A. Smith, *Angew. Chemie - Int. Ed.* **2016**, *55*, 9748–9752.
- [12] K. Jiang, P. Kharel, Y. Peng, M. K. Gangishetty, H. Y. G. Lin, E. Stavitski, K. Attenkofer, H. Wang, *ACS Sustain. Chem. Eng.* **2017**, *5*, 8529–8534.
- [13] N. J. Firet, M. A. Blommaert, T. Burdyny, A. Venugopal, D. Bohra, A. Longo, W. A. Smith, *J. Mater. Chem. A* **2019**, *7*, 2597–2607.
- [14] H. Mistry, Y. Choi, A. Bagger, F. Scholten, C. S. Bonifacio, I. Sinev, N. J. Divins, I. Zegkinoglou, H. S. Jeon, K. Kisslinger, E. A. Stach, J. C. Yang, J. Rossmeisl, B. Roldan Cuenya, *Angew. Chemie* **2017**, *129*, 11552–11556.
- [15] M. Parente, M. Van Helvert, R. F. Hamans, R. Verbroekken, R. Sinha, A. Bieberle-Hütter, A. Baldi, *Nano Lett.* **2020**, *20*, 5759–5764.
- [16] S. E. Skrabalak, B. J. Wiley, M. Kim, E. V. Formo, Y. Xia, *Nano Lett.* **2008**, *8*, 2077–2081.
- [17] H. R. Lutterotti, L., Matthies, S., Wenk, *MAUD: A Friendly Java Program for Material*

Analysis Using Diffraction, **1999**, 14–15.

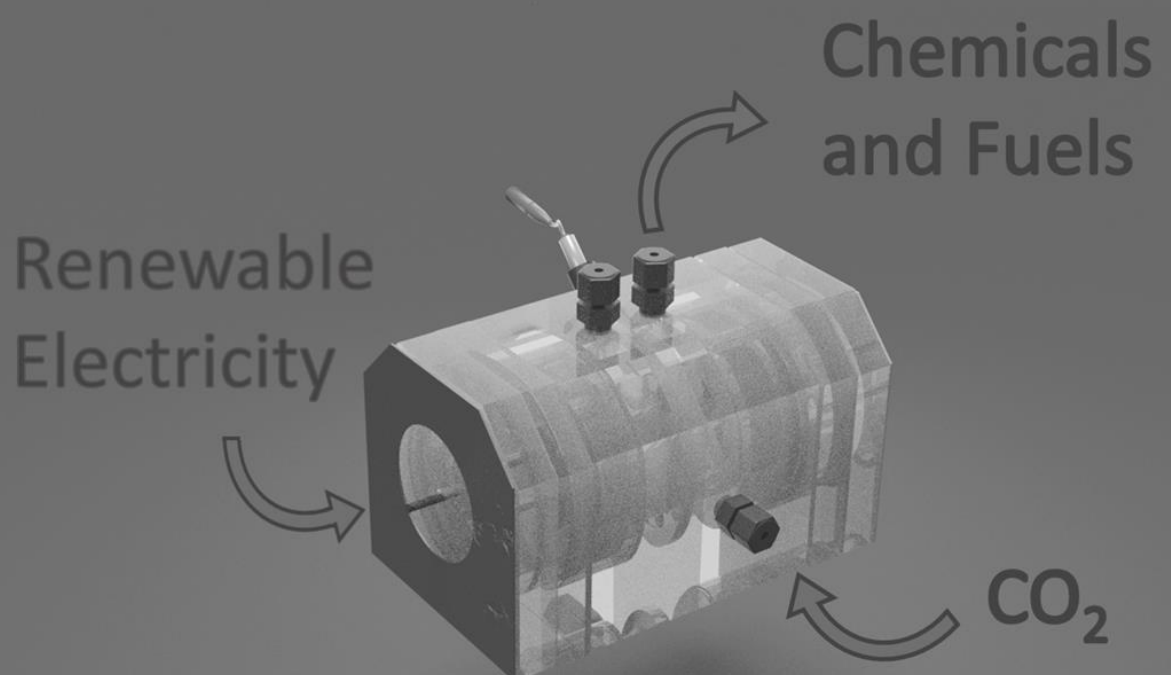
- [18] C. Kim, H. S. Jeon, T. Eom, M. S. Jee, H. Kim, C. M. Friend, B. K. Min, Y. J. Hwang, *J. Am. Chem. Soc.* **2015**, *137*, 13844–13850.
- [19] F. Mattarozzi, N. Visser, J. W. de Rijk, P. Ngene, P. de Jongh, *Eur. J. Inorg. Chem.* **2022**, e202200365.
- [20] B. Boukamp, *Solid State Ionics* **2004**, *169*, 65–73.
- [21] B. Boukamp, *Solid State Ionics* **1986**, 136–140.
- [22] W. A. Al-Saidi, H. Feng, K. A. Fichthorn, *Nano Lett.* **2012**, *12*, 997–1001.
- [23] J. Zeng, Y. Zheng, M. Rycenga, J. Tao, Z. Y. Li, Q. Zhang, Y. Zhu, Y. Xia, *J. Am. Chem. Soc.* **2010**, *132*, 8552–8553.
- [24] A. Al-Sarraj, K. M. Saoud, A. Elmel, S. Mansour, Y. Haik, *SN Appl. Sci.* **2021**, *3*, 1–13.
- [25] T. U. Hur, W. S. Chung, *J. Electrochem. Soc.* **2005**, *152*, A996.
- [26] D. Lützenkirchen-Hecht, H. H. Strehblow, *Surf. Interface Anal.* **2009**, *41*, 820–829.
- [27] J. E. B. Randles, *Discuss. Faraday Soc.* **1947**, *1*, 11–19.
- [28] H. L. Johnston, F. Cuta, *J. Am. Chem. Soc.* **1933**, *55*, 2311–2325.
- [29] S. S. Abd El Rehim, H. H. Hassan, M. A. M. Ibrahim, M. A. Amin, *Monatshefte für Chemie* **1998**, *129*, 1103–1117.
- [30] D. B. Gibbs, B. Rao, R. A. Griffin, M. J. Dignam, *J. Electrochem. Soc.* **1975**, *122*, 1167–1174.
- [31] M. Dunwell, W. Luc, Y. Yan, F. Jiao, B. Xu, *ACS Catal.* **2018**, *8*, 8121–8129.
- [32] A. Goyal, G. Marcandalli, V. A. Mints, M. T. M. Koper, *J. Am. Chem. Soc.* **2020**, *142*, 4154–4161.
- [33] Y. Yoon, A. S. Hall, Y. Surendranath, *Angew. Chemie - Int. Ed.* **2016**, *55*, 15282–15286.



Turin, Italy

CHAPTER 6

Summary, Outlook and Samenvatting



Summary

The work described in this thesis was aimed at understanding the influence of structural properties of silver catalysts supported on carbon for the electrocatalytic reduction of CO_2 to CO. This goal was achieved by rationally designing cathode materials, which were characterized and tested. This enabled a correlation between material properties, such as number of surface functional groups, silver particle size, hydrophobicity, cathode oxidation state, and the catalytic performance, such as the total current density, faradaic efficiency and partial current density normalized by active surface area.

Chapter 1 describes the potential benefits of electrochemistry and electrocatalysis in the context of global warming. The theoretical background of electrochemistry is explained, including models such as the Nerst equation and the Butler-Volmer equation. The Gouy-Chapman-Stern model is introduced to define the composition of the electrolyte solution as a function of the distance from the electrode surface. This description is relevant as electrocatalytic reactions occur at electrode-electrolyte interface. Finally, the CO_2 electrocatalytic reduction to value-added chemicals was described, including the effect of different metal electrodes and buffer electrolytes. Specifically, a background is given on the CO_2RR to CO over silver electrocatalysts, and the properties of carbon electrodes, based on literature.

In chapter 2, the effect of surface-modification of carbon-based electrodes on the reduction of CO_2 to CO is systematically treated. Building on experience of our research group on support functionalization for thermal catalysts, O-containing and N-containing groups were introduced on the surface of high surface area carbon materials *via* liquid phase oxidation and gas phase amination, respectively. Furthermore, most of the acidic carbon surface groups were removed by a high temperature reduction treatment, leading to a catalyst with a neutral surface. The surface chemistry of the electrodes was characterized with acid-base titration, potentiometric titration and XPS. The basic surface properties (high point of zero charge) of the N-functionalized carbon catalyst led to an increased CO production with respect to the O-functionalized and reduced carbon materials. The CO turnover frequency per surface group for pyridinic groups was 30-times higher than for O-containing groups. Although the selectivity of these catalysts was dominated by the competing H_2 evolution reaction over the carbon

surface, this study demonstrated the possibility to tune the surface properties of carbon materials to enhance the ability of the electrocatalyst to reduce CO_2 to CO.

In chapter 3, the effect of silver nanoparticle size on the CO_2 reduction to CO is discussed. Using the surface modification methods described in chapter 2, control over the ligand-free silver particle size was achieved by tuning the surface properties of the carbon supports. It was demonstrated that the silver particle size, in the range of 10 to 30 nm, decreased by increasing the density of O-containing group on the support. Although the silver weight loading onto the high surface area carbon was relatively low ($0.1 \text{ mg}_{\text{Ag}} \text{ cm}^{-2}$), the small nanoparticles (11 nm diameter) effectively steered the selectivity towards CO up to 25%, even greater than the selectivity achieved by bulk silver electrodes under the same conditions. The mass activity of the catalysts decreased with increasing particle size, while the CO current density normalized by metal surface only marginally depended on the particle size. Hence, the better performance of smaller nanoparticles was due to a better dispersion of the silver.

In chapter 4, the aim was to suppress the hydrogen formation over the high surface area carbon support by functionalizing the surface of the support with alkylamines. The effect of the number of carbon atoms in the alkyl chain on the HER suppression and CO selectivity was investigated. A low weight loading ($0.0016 \text{ mg}_{\text{Ag}} \text{ cm}^{-2}$) of colloidal silver nanoparticles (8.2 nm) was deposited onto the modified support to enable the reduction of CO_2 . XPS and contact angle analysis showed that the alkylamines were introduced onto the carbon surface, and that they increased the hydrophobicity and decreased the acidity. Alkylamine functionalization suppressed H_2 evolution, while at the same time promoting CO production. This resulted in a 1 to 2 H_2 to CO ratio for the catalyst functionalized with hexylamine, more favorable than for the pristine carbon-based catalyst (benchmark), able to generate only a 3.3 to 1 H_2 to CO ratio. This ratio is important as the electrochemical production of syngas, a mixture of hydrogen and carbon monoxide, might represent an opportunity to produce sustainable fuels.

In chapter 5, the catalytic properties of a different silver morphology, silver nanowires, are explored. It has been reported that for CO formation, silver nanowires are more favorable than nanoparticles due to a high 100 to 111 facet ratio. Electrochemical oxidation of the silver nanowires was performed to introduce surface defects. XRD and XPS analysis confirmed that by selecting the final potential during the oxidation procedure, different silver compositions were achieved, from metallic silver nanowires to a mixture of Ag_2O and AgO before catalysis.

The wires changed morphology as a function of the oxidation potential; more positive oxidation potentials led to a higher surface roughness. This surface-modification procedure enhanced the catalytic properties of the nanowires. The active surface-normalized CO partial current density increased 3.7-times when the pristine nanowires were oxidized to 1.0 V vs Ag/AgCl in basic electrolyte solution. The higher selectivity is ascribed to either the formation of new active sites or a change in the local environment.

In summary, this thesis shows four methods to influence the catalytic performance of silver nanostructures supported on high surface area carbon materials, achieved by either modifying the support or the metal surface. The in-depth characterization of these materials enabled the correlation between the physical-chemical properties of the catalysts and their catalytic activity and selectivity.

Outlook

Although in chapter 3 we studied particle size effects, we could not establish a clear correlation between silver particle size and CO selectivity for nanoparticles in the range from 10 to 30 nm. By further tuning the carbon support surface properties, i.e. increasing the number of acidic surface groups, and exploring different silver precursors, the silver nanoparticles size range could be extended in the range 1 to 30 nm. By combining experimental and theoretical analysis, it could be investigated how the ratio between size dependent CO₂RR active sites, such as edges and corners, influences the reaction mechanism and the product selectivity. This research could shed light on the mechanism behind the CO₂RR on silver and possibly offer new insight for the rational design of electrodes materials. Furthermore, this simple and scalable procedure can also be applied to other metals, such as copper, and bi-metallic systems, thus increasing the interest in this approach.

The alkylamine functionalization procedure (chapter 4) was developed to suppress the H₂ formation and therefore increase the selectivity towards CO₂ reduction products. The same method could be used to optimize gas diffusion electrodes, in which the hydrophobicity not only prevents the electrode flooding during operations, but also effectively suppresses the H₂ evolution reaction. Stable bonds between the alkylamine functionalization and the carbon surface are desired. Hence, thionyl chloride-mediated synthesis might represent a viable alternative to covalently graft the amines to the support. Furthermore, by using di-amines, it will be possible to simultaneously functionalize the carbon surface with the hydrophobic moieties and absorb CO₂ *via* the N-containing group. This functionalized electrode material could facilitate the use of electrochemical cells (electro swing devices) which aim both to capture and convert CO₂. This could lead to practical implementation of electrocatalysis technologies to decrease the greenhouse gas net emissions.

Regarding oxide-derived silver nanowires supported on carbon (chapter 5), what exactly is the cause for the difference between oxide-derived and pristine electrodes remains a scientific open question. In-situ *operando* Raman spectroscopy could unravel different reaction intermediates adsorption modes onto the electrodes. For instance, the difference in adsorption strength between the different metal surfaces and the *COOH intermediate, supposedly the rate determining step of the reaction, could be investigated in the 300-500

cm⁻¹ Raman shift region as a function of the applied potential for different silver structures, exposing different dominant facets.

Beside applications in CO₂ reduction, the use of silver nanostructures could be applied to other electrocatalytic systems, such as the ascorbic acid oxidation reaction or N₂ reduction to NH₃, which potentially poses the basis for a sustainable route for ammonia production.

Samenvatting

Menselijke CO₂-emissies zijn een van de voornaamste oorzaken van klimaatverandering. Inmiddels is naar schatting de gemiddelde temperatuur op aarde al 1.0 °C hoger dan aan het begin van de industriële revolutie. Hernieuwbare energiebronnen moeten fossiele brandstoffen gaan vervangen om rampzalige gevolgen van klimaatverandering te voorkomen. Toch blijven zowel het wisselvallige karakter (de zon schijnt niet altijd en de wind waait niet altijd) als de grootschalige toepassing van hernieuwbare energiebronnen een uitdaging. Technologieën voor het afvangen, gebruiken en opslaan van koolstof (CCUS) kunnen bijdragen aan het verminderen van de concentratie van CO₂ in de atmosfeer. Elektrokatalyse biedt de mogelijkheid om CO₂ en H₂O om te zetten in brandstoffen en chemische bouwstenen, waarbij groene stroom als energiebron kan worden gebruikt, en de koolstofcyclus gesloten wordt

Deze zogenaamde “CO₂ Reductie Reactie”, of kortweg CO₂RR, kan onder milde omstandigheden en in water worden uitgevoerd. De uitkomst van de reactie kan gestuurd worden door het aanpassen van parameters zoals de potentiaal, de samenstelling van de waterige elektrolytoplossing en de CO₂ partiële druk. Tegelijkertijd kan echter niet alleen CO₂ maar ook water gereduceerd worden, waarbij H₂ gevormd wordt, wat de efficiëntie van de omzetting van CO₂ verlaagt. Daarom is het essentieel om goede kathodematerialen te ontwikkelen, die leiden tot een efficiënte omzetting van CO₂.

In zijn baanbrekend werk toonde Hori enkele decennia geleden al aan dat zilver een van de meest veelbelovende metalen is voor CO₂-reductie, omdat het selectief CO laat vormen, een waardevolle chemische bouwsteen. Daarom ontwikkelden veel onderzoeksgroepen elektrokatalysatoren met nanogestructureerd zilver, afgezet op geleidende dragermaterialen. Het gebruik van dragermaterialen zoals koolstof kan de katalytische prestaties verbeteren en het metaalverbruik verminderen. Het doel van het onderzoek zoals beschreven in dit proefschrift was om de belangrijkste variabelen te begrijpen die invloed hebben op de CO₂ omzetting, zoals de grootte en vorm van de metaaldeeltjes en de oppervlakte-eigenschappen van metaal en koolstofdrager, die de snelheid en de selectiviteit tijdens de CO₂RR naar CO beïnvloeden.

Hoofdstuk 2 beschrijft een systematische studie naar aanpassingen van het oppervlak van koolstofdragermaterialen door zure zuurstof-bevattende groepen en basische stikstof-

bevattende groepen te introduceren, met als doel de katalytische eigenschappen te beïnvloeden. Om het effect van de zure en basische oppervlaktegroepen aan te tonen, hebben we ook alle oppervlaktegroepen verwijderd door een hoge-temperatuur-behandeling. Dit hoofdstuk biedt een uitgebreide discussie over het effect van specifieke oppervlaktegroepen op de CO-selectiviteit. We laten hier zien dat de stikstof bevattende groepen, en met name de pyridinegroepen, de CO₂-reductie tot CO verbeteren, en wel 30 keer actiever zijn dan zuurstofhoudende oppervlakte groepen. Desalniettemin blijft ook de gelijktijdige H₂ productie een belangrijke rol spelen

In hoofdstuk 3 wordt het effect van de zilver deeltjesgrootte op de CO₂RR naar CO reactie besproken. Kale (ligandvrije) zilvernadeeltjes werden aangebracht op koolstofmaterialen met een hoog oppervlak. De deeltjesgrootte werd gevarieerd door de koolstofdrager te functionaliseren met zure oppervlaktegroepen. We vergeleken de katalytische prestaties van drie katalysatoren met verschillende deeltjesgroottes tussen 10 en 30 nm. Hoewel nog steeds voornamelijk waterstof gevormd werd, toonden we aan dat de stroomdichtheid voor CO, genormaliseerd door zilvermassa, groter is voor kleinere deeltjes. Dit komt niet doordat het oppervlak van eigenschappen verandert, of meer functionele groepen heeft per nm². De oorzaak is het grotere oppervlak per gram zilver voor kleinere deeltjes.

In hoofdstuk 4 wordt het aanbrengen van hydrofobe functionele alkylamine groepen op het oppervlak van de drager beschreven, met als doel de vorming van waterstof op de koolstofdrager met een groot specifiek oppervlak te onderdrukken. Dit resulteerde in zeer waterafstotende koolstofelektroden met randhoeken > 90°. Met een lage zilverlading onderzochten we het effect van verschillende lineaire alkylamine ketenlengtes op de selectiviteit naar CO. inderdaad werd de productie van CO hoger dan voor katalysatoren met een onveranderde koolstofdrager, en toont aan dat hydrofobe groepen op het koolstofoppervlak gunstig zijn om de waterstofproductie te onderdrukken.

In hoofdstuk 5 worden experimenten beschreven met een andere vorm van de zilver nanodeeltjes; in plaats van polykristallijne nanodeeltjes richtten we ons op zilver nanodraden, die gunstig zijn voor de CO₂RR naar CO aldus de literatuur. Uitgaand van de al zeer CO selectieve elektroden introduceerden we extra oppervlaktedefecten door gecontroleerde elektrochemische oxidatie. De intrinsieke selectiviteit naar CO wordt groter naarmate we

steviger oxideren, wat tot een 3.7 maal hogere specifieke CO-stroomdichtheid leidt in vergelijking met niet geoxideerde zilver nanodraden.

Samenvattend bespreekt dit proefschrift vier methoden om de katalytische prestaties van zilveren nanostructuren afgezet op koolstofmaterialen te verbeteren. Vooruitgang is geboekt door ofwel de koolstofdrager ofwel het zilvermetaaloppervlak aan te passen. Dit heeft geleid tot een beter begrip van hoe we efficiënte, op zilver gebaseerde elektrokatalysatoren kunnen maken om CO₂ om te zetten in CO.

List of publications

This thesis is partially based on the following publications:

- Francesco Mattarozzi, Marisol Tapia Rosales, Rim van de Poll, Emiel Hensen, Peter Ngene and Petra de Jongh, 'Surface-modified carbon materials for CO₂ electroreduction', *European Journal of Inorganic Chemistry*, **2023**, e202300152.
- Francesco Mattarozzi, Nienke Visser, Jan Willem de Rijk, Peter Ngene and Petra de Jongh, 'Ligand-free silver nanoparticles for CO₂ electrocatalytic reduction to CO', *European Journal of Inorganic Chemistry*, **2022**, e202200365.
- Francesco Mattarozzi, Karen van den Akker, Matt Peerlings, Maaïke Vink-van Ittersum, Nienke Visser, Rim van de Poll, Emiel Hensen, Peter Ngene and Petra de Jongh, 'Alkylamine-functionalized carbon supports to enhance the silver nanoparticles electrocatalytic reduction of CO₂ to CO', *ChemElectroChem*, **2023**, e202300295.
- Francesco Mattarozzi, Nolan van der Willige, Valerio Gulino, Claudia Keijzer, Rim van de Poll, Emiel Hensen, Peter Ngene and Petra de Jongh, 'Oxide-derived silver nanowires for CO₂ electrocatalytic reduction to CO', *ChemCatChem*, **2023**, e202300792.

Other publications:

- Nienke L. Visser, Juliette C. Verschoor, Luc C.J. Smulders, Francesco Mattarozzi, David J. Morgan, Johannes D. Meeldijk, Jessi E.S. van der Hoeven, Joseph A. Stewart, Bart D. Vandegehuchte, Petra E. de Jongh, 'Influence of carbon support surface modification on the performance of nickel catalysts in carbon dioxide hydrogenation', *Catalysis Today*, **2023**, 418, 114071.

Oral presentations:

- Francesco Mattarozzi, Peter Ngene and Petra de Jongh, 'Oxide-Derived Silver Nanowires for CO₂ Electrocatalytic Conversion to CO', *The Netherlands' Catalysis and Chemistry Conference (NCCC2022)*, **2022**, Noordwijkerhout (The Netherlands).
- Francesco Mattarozzi, Peter Ngene and Petra de Jongh, 'Oxide-Derived Silver Nanowires for CO₂ Electrocatalytic Conversion to CO', *The 26th Canadian Symposium on Catalysis (CSC2022)*, **2022**, Vancouver (Canada).
- Francesco Mattarozzi, Peter Ngene and Petra de Jongh, 'Oxide-Derived Silver Nanowires for CO₂ Electrocatalytic Conversion to CO', *The 27th North American Catalysis Society Meeting (NAM27)*, **2022**, New York (USA).
- Francesco Mattarozzi, Peter Ngene and Petra de Jongh, 'E-mpowering the Future Generation: Is Materials Design and Electrochemistry Key for CO₂ Valorization?', *European Industry & Energy Summit (EIES2022)*, **2022**, Geleen (The Netherlands).
- Francesco Mattarozzi, Peter Ngene and Petra de Jongh, 'CO₂ recycling', **2019**, *eye-openers.nl* (online).

Poster presentations:

- Francesco Mattarozzi, Marisol Tapia Rosales, Kai Han, Peter Ngene and Petra de Jongh, 'Ligand-free synthesis of Ag nanoparticles on carbon for CO₂ electrochemical reduction' *ECCM Graduate school*, **2019**, Eerbeek (The Netherlands).

-
- Francesco Mattarozzi, Marisol Tapia Rosales, Kai Han, Peter Ngene and Petra de Jongh, 'Ligand-free synthesis of Ag nanoparticles on carbon for CO₂ electrochemical reduction' *ARC-CBBC symposium*, **2019**, Eindhoven (The Netherlands).
 - Francesco Mattarozzi, Peter Ngene and Petra de Jongh, 'Ligand-free synthesis of Ag nanoparticles on carbon for CO₂ electrocatalytic reduction', *NanoGe Structure-function relationship in CO₂ electrocatalysis*, **2020**, online.
 - Francesco Mattarozzi, Marisol Tapia Rosales, Kai Han, Peter Ngene and Petra de Jongh, 'Ligand-free synthesis of Ag nanoparticles on carbon for CO₂ electrochemical reduction' *The Netherlands' Catalysis and Chemistry Conference (NCCC2020)*, **2020**, Noordwijkerhout (The Netherlands).
 - Francesco Mattarozzi, Nienke Visser, Jan Willem de Rijk, Peter Ngene and Petra de Jongh, 'Ligand-free silver nanoparticles for CO₂ electrocatalytic reduction to CO', *WE-Heraeus-Seminar*, **2022**, online.

About the author

Francesco Mattarozzi was born on the 7th of September 1994, in Como (Italy). After completing high school at Liceo Scientifico Galileo Galilei (Erba, Italy) in 2013, he obtained his bachelor's degree (110/110) in Chimica Industriale (industrial chemistry) at Università Statale di Milano (Milan, Italy) in 2016. During his bachelor thesis, he studied 'drugs degradation in aqueous environment by using photocatalytic ceramic supports based on micrometric titanium dioxide' under the supervision of Prof. Claudia M. L. Bianchi. In 2016, he started his master's in industrial chemistry at Università Statale di Milano (Milan, Italy). In 2018, he performed his master thesis project on 'palladium-based catalysts for selective hydrogenation reactions in liquid phase' under the supervision of Laura Prati. During the master thesis, he obtained a grant for the Erasmus Traineeship and performed a 5-month research project at Utrecht University (The Netherlands). During the Erasmus Traineeship, he worked on 'gas phase selective hydrogenation of 1,3 butadiene using Pd-Ni bimetallic catalysts' under the supervision of Giorgio Totarella and Prof. Dr. Petra E. de Jongh. He obtained his master's degree (110 cum laude/110) in 2018. On the 1st of December 2018, he started his PhD at Utrecht University, under the supervision of Prof. Petra E. de Jongh and co-supervision of Dr. Peter Ngene. His PhD resulted in 4 manuscripts published in international scientific journals and he presented his work at several national and international conferences. He was awarded an oral presentation award (The Netherlands' Catalysis and Chemistry Conference, 2022, Noordwijkerhout, The Netherlands).

